Nanoscopic infrared characterisation of graphene oxide

A Thesis Submitted to the University of Manchester for the Degree of

Master of Philosophy

In the Faculty of Faculty of Science & Engineering

2018

Pietro Steiner

School of Materials

Supervisor: Aravind Vijayaraghavan

“To my friends and for all the dyslexics that fearlessly tackling the world”

Contents

List of Figures:

List of tables:

List of abbreviation:

µm:	Micrometre
0D:	Zero-dimensional
1D:	One-dimensional
2D:	Two-dimensional
3D:	Three-dimensional
AFM:	Atomic force microscope
AFM-IR:	Atomic force microscope coupled infrared spectroscopy
CVD:	Chemical vapour deposition
GO:	Graphene oxide
GPa:	Gigapascal
nm:	Nanometre
NMR:	Nuclear magnetic resonance
rGO:	Reduced graphene oxide
SEM:	Scanning electron microscope
SWCNT:	Single-walled carbon nanotube
TEM:	Transmission electron microscope
wt%:	Weight percentage
XPS:	X-ray photoelectron spectroscopy
Rms	Root mean squared
CT AFM	Contact mode atomic force microscope
Bulk-IR	Bulk FTIR
T-IR	Transmission FTIR
FLGO	Few layers GO sample

GO 4-IRA	IR amplitude spectra of GO with sample thickness of 0,4μm
GO 60-IRA	IR amplitude spectra of GO with sample thickness of 60 nm
GO 10-IRA	IR amplitude spectra of GO with sample thickness of 10 nm
GO 1-IRA	IR amplitude spectra of GO with sample thickness of 1 nm
ThAu	Thermally evaporated gold coated substrate
TAu	Strip-templated gold coated substrate

Abstract:

Graphene oxide (GO) is a single layer of carbon atoms decorated with oxygen groups, which has recently gained interest as a reinforcing filler in composite materials, in filtration processes and for biomedical applications. However, the structure of GO has not been fully characterised, mainly due to the lack of spectroscopic techniques for the unambiguous identification of the oxygen groups onto the surface of GO at the nanoscale. Only recently it has been demonstrated that by using a contact mode Atomic Force Microscopy (AFM) coupled with an IR tuneable source (AFM-IR) it is possible to characterise monolayer GO flakes with a spatial resolution below the diffraction limit.

This work investigates the thickness dependence of AFM-IR analysis with respect to GO spectroscopy and provides a comparison with the conventional FTIR of GO materials. This thesis highlights the great discrepancies within the two IR techniques especially on thinner samples (<10nm) and therefore goes some way to showing the limit of detection for AFM-IR of GO and other two-dimensional materials on a range of techniques. Through experimental investigation, it has been found that that the roughness of the substrate plays an important role in the AFM-IR characterisation of nanomaterials. It has also been discovered that by using an atomically smooth gold substrate the IR amplitude signals of GO flakes are significantly enhanced.

It is anticipated that further improvements of the AFM-IR characterisation could arise from the results found in this thesis; such as the use of different substrates that could lead to an increase of the IR amplitude signal of monolayer GO, further decreasing the detection limit and increasing both the spectral and spatial resolution of this technique for two-dimensional materials.

Declaration:

No portion of the work referred to in the thesis has been submitted in support of an application for another degree or qualification of this or any other university or other institute of learning

Pietro Steiner

Copyright statement:

Acknowledgement

I would like to express my very great appreciation to my Supervisor Aravind Vijayaraghavan, who decided to accept me into his marvellous research group, for this great year of research and for his valuable advice.

I would like to offer my genuine gratitude to Cian, for the fantastic leadership of my project and for being able to teach me the real meaning of the word "science". Moreover, for having faith in me as a scientist and also as a friend.

To Maria for her help in the laboratory and for the impeccable leadership of the laboratory.

I am particularly grateful for the assistance, support and advice given by Natalie (My daily sunshine), Daniel (for the night sessions spent together), Dai, Wentao and to all the Aravind group for the help received.

I would like to express my eternal gratitude to Molly for being my cornerstone throughout this year abroad.

My special thanks are extended to all my friends from the Graphene NOWNANO CDT, for all the advice given and for the confidence to continue my research within a CDT program next year. In particular, I would like to say thanks to Steffan, Fiona, Sebastian and Captain Vaiva.

I would like to acknowledge the support provided my friends within the MUCC and all my international friends around the globe.

I am particularly grateful and thankful for all the assistance and support given by my family, in allowing me to embark on this exceptional journey, and for providing me a solid foundation in my life. Last but not least, I must say a thank you to Macchia and Ette.

Thank you to all of you who helped me throughout this year, you have all been my sunshine in Manchester.

1. Introduction and Aim of the Project

Graphene Oxide (GO) is a two-dimensional (2D) material made of a single layer of carbon atoms functionalised with oxygen functional groups. GO has been considered as a precursor material for the large scale production of graphene, a material with superior proprieties particularly mechanical strength and electronic properties[1]. Almost immediately, GO attracted great interest due to its unique structure leading to the development of several applications from drug delivery systems to water purification and as a reinforcer in composite materials [2,3].

A great effort has been made to determinate the exact GO structure however due to the nonstoichiometric chemical composition, this has proved challenging. A further limitation in the structural study of GO is the absence of sensitive characterisation techniques which combine high spatial resolution with chemical species identification; for unambiguous identification of the functional group onto the GO surface[4,5]. A comprehensive chemical characterisation of GO is important in the development of future GO applications.

The first aim of this project was to determine the chemical composition of commercial GO using XPS, Raman, SEM and FT-IR techniques that are commonly used and then to employ AFM-IR to compare against these methods. A contact mode AFM coupled with an IR tuneable source (AFM-IR) combines the chemical characterisation analysis of the IR spectroscopy with the high spatial resolution of an AFM tip (less the 30nm) and, therefore AFM-IR is a promising prospective technique for the characterisation of GO and 2D materials in general.

AFM-IR has a high spatial resolution, ~30 nm and is commonly used in the analysis of thin films on the order of microns[6]. In order to evaluate whether the AFM-IR could be used as an improvement of the conventional FTIR for 2D materials, AFM-IR spectroscopy and conventional FTIR spectroscopy will be directly compared. Additionally, the limit of detection of the AFM-IR was evaluated by varying the GO sample thickness (1µm to 1nm).

Belkin *et al.* showed that the substrate on which GO is deposited plays an important role in the enhancement and sensitivity of the AFM IR[7]. To further evaluate the effect of the substrate on the AFM-IR characterisation of monolayer GO, samples with varying substrate roughness are to be produced and analysed.

2. Literature Review

2.1 Introduction to Graphene

Carbon, the element of life, is one of the most abundant elements in nature and several carbon allotropes have been found, each of them having unique proprieties and spatial conformation. Carbon allotropes can therefore be classified based on their form in Cartesian space. Three-dimensional (3D) allotropes include graphite, diamond and amorphous carbon (Figure 1).

Graphite and diamond have a crystalline structure based on sp^2 and sp^3 hybridized carbon-carbon bonding respectively, in contrast amorphous carbon is mainly made by a mixture of sp^2 and sp^3 without any crystalline order[8].

The zero-dimensional (0D) carbon allotropes were first discovered in 1985 by Kroto *et al.* and are collectively known as fullerenes. Fullerenes identify a classes of nanomaterials that are form of sp^2 carbon atoms arranged in both pentagonal and hexagonal spherical lattice [9].

Later in 1991, one dimensional (1D) allotropes were synthesised in the form of single walled carbon nanotubes (SWCNT) by Sumio Iijima[10]. These SWCNTs can be conceptualised as a single layer of sp^2 carbon rolled into a tube and joining back up to itself.

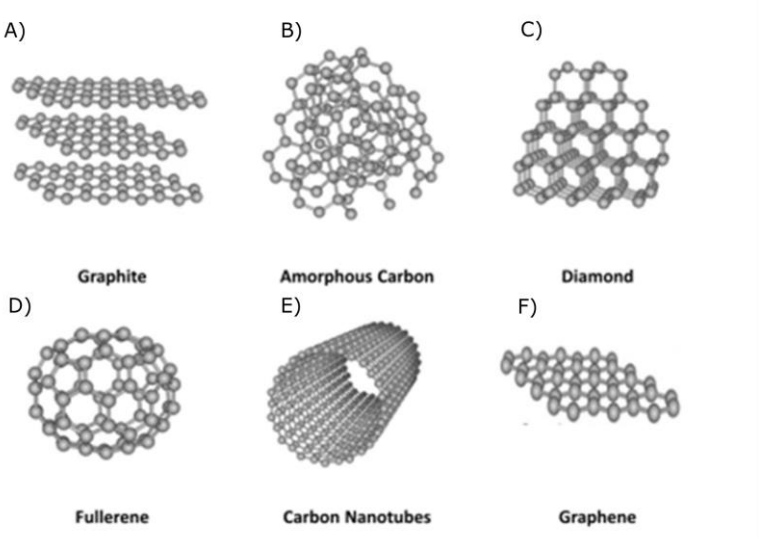

Figure 1 Structures of Carbon allotropes discovered: 3D allotropes A) Graphite **B**) Amorphous Carbon **C**) Diamond**. Novel allotropes recently discovered**: **D**) Fullerene (0D) **E**) Carbon Nanotubes (1D) and **F**) Graphene (2D) [11]**.**

The two-dimensional (2D) carbon allotrope, Graphene, is a single layer of carbon atoms arranged in a hexagonal lattice. Graphene was first postulated as model to explain the

properties of graphite [12] and it was assumed by the Mermin-Wagner's theorem[13] that a single free standing atom layer was intrinsically unstable. However, in 2004 pristine Graphene was isolated by the micromechanical exfoliation of graphite at the university of Manchester[14].

Experiments on the stability of freestanding graphene membranes has shown its stability is related to "nano-undulations" (Figure 2), approximately 1 nm height, of the graphene sheet [15] and since the discovery of graphene, it has been shown to be a revolutionary material with superior proprieties.

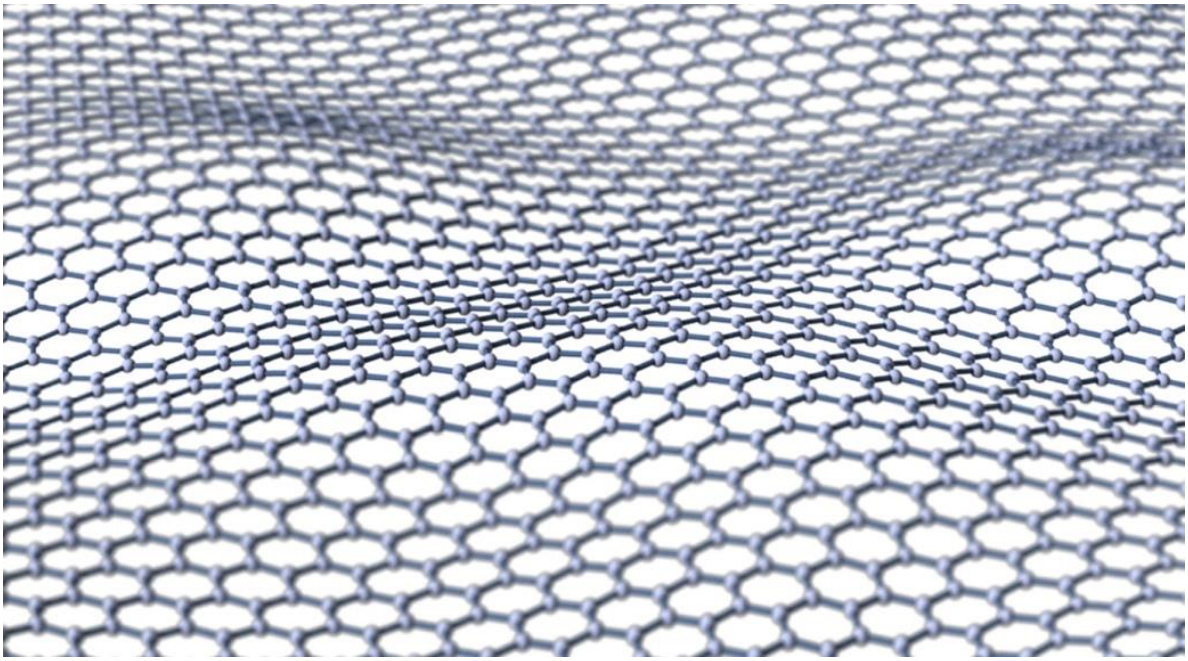

Figure 2 Representation of Nano undulations in the Graphene lattice[16]

2.2 Graphene Structures and Proprieties:

Each of the carbon atoms in a graphene sheet are hybridized sp^2, therefore every carbon atom has 3 sp^2 orbitals and one 2p orbital perpendicular to the sp^2 plane, with an in-plane carbon-carbon bond length of 1.42 Å (Figure 3). The superior properties of this material derive from the strong interaction between sp^2 orbitals and the delocalised 2p electrons. The 2p electrons mutually interact and form the π*(conduction) and π (valence) bands, which create the in-plane electrical conductivity [17].

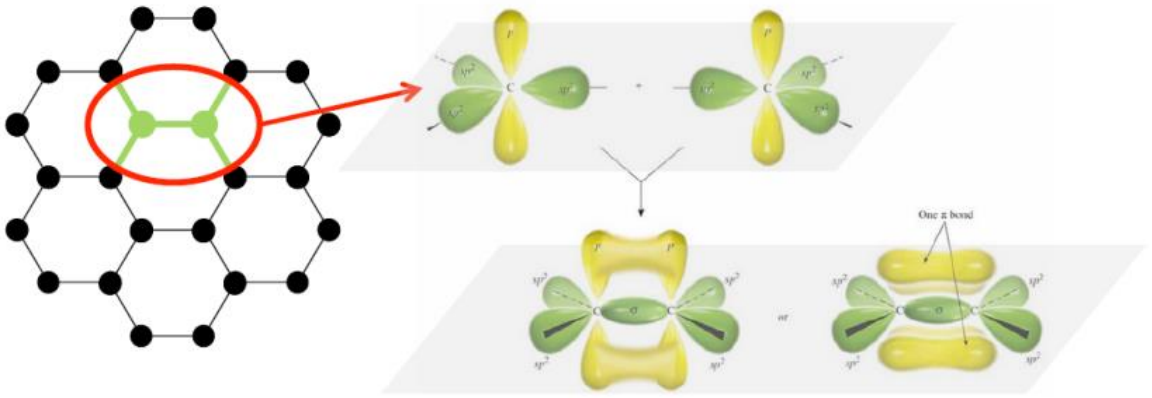

Figure 3 Represenation of the sp^2 carbon bonds in graphene: the images highlight the interaction between the carbon orbitals sp^2 (σ bond) and 2p (π bond)[18].

A change in the momentum of the charge carriers reflects in a change of the bands' energies. The conduction bands of graphene are conical valleys (Figure 4) and they meet each other at the high-symmetry K and K' points of the first Brillouin zone[8]. In proximity of K and K' points, the energy-momentum varies following a linear dispersion relation, and follow the Dirac equation[19]. This means that the carriers seen as zero-rest mass relativistic particles move almost at the speed of light, c =10^6 m/s, and the limit of the conductivity is the fermi velocity [19,20].

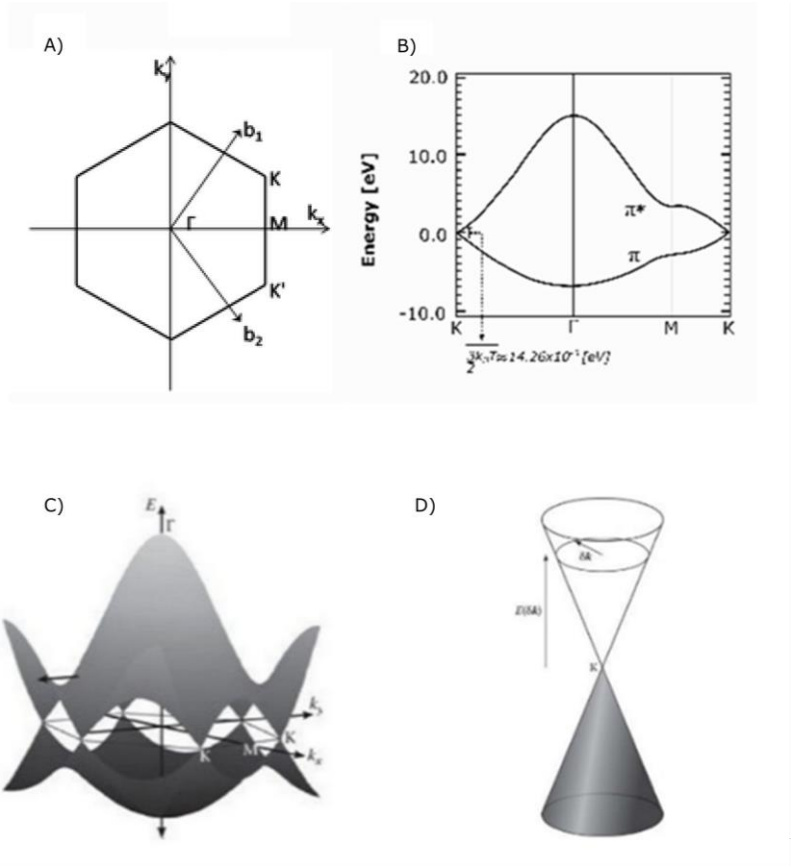

Figure 4 Representation of First Brillouin zone and energy dispersion A) Representation of First Brillouin zone of graphene. **B)** Diagram of the energy dispersion relates to π-electrons along the high symmetry directions. **C)** 3D plot of energy dispersion, the valence band (lower) and the conductive bands (upper) meet at the high symmetry point K, therefore graphene is a Zero-bandgap semiconductor. **D)** Graphic representation of linear dispersion relation near the K point in graphene. Adapted from[8]**.**

Some of the earliest experiments of graphene showed it exhibits an half–integer quantum hall effect, is a zero-band gap semimetal[21] and graphene electrons can channel through any potential height without being reflected back. As a result, graphene electrons can propagate through the graphene lattice for relatively long distances, in the order of microns[22].

Graphene is the world's thinnest material, with a theoretical height of only 0.335 nm[23] and exhibits incredible physical proprieties. The elastic proprieties of graphene were measured using nanoindentation AFM (Figure 5); and found to be the strongest material ever measured with a Young's modulus of 1.0 TPa, third order elastic stiffness of 2.0 TPa and intrinsic strength of 130 GPa[24].

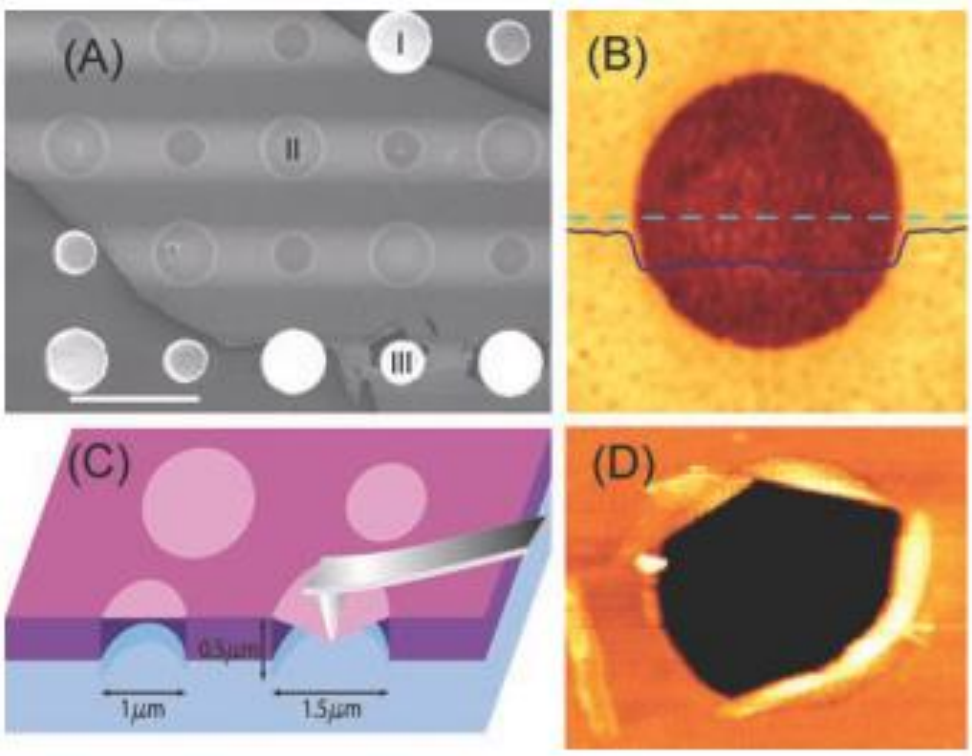

Figure 5 Nanoindetetion of suspended graphene: A) SEM image of suspended graphene onto holes array (1μm and 1.5 μm diameter)**. B)** Noncontact mode AFM image of suspended graphene**. C)** Nanoindentation representation on suspended graphene membrane**. D)** AFM image after the indentation. Adapted from[24].

In addition, free standing graphene displays high thermal conductivity up to 5300 W/mK [25], a high optical transparency of 97,7% using a white light (~500 nm)[26] and a pristine graphene monolayer can act as a perfect gas barrier to most of atoms and molecules[27].

All these superior proprieties make graphene an attractive material for several applications[1] and consequently, high quality graphene is required for industry and academia in bulk quantities.

2.3 Graphene Production

Many techniques have been used to synthesise graphene (Figure 6), with each production method having advantages and disadvantages. Ideally the final product needs to be high quality, but with low production costs. Currently, the optimum cost-effective production method has not been determined for all applications[28].

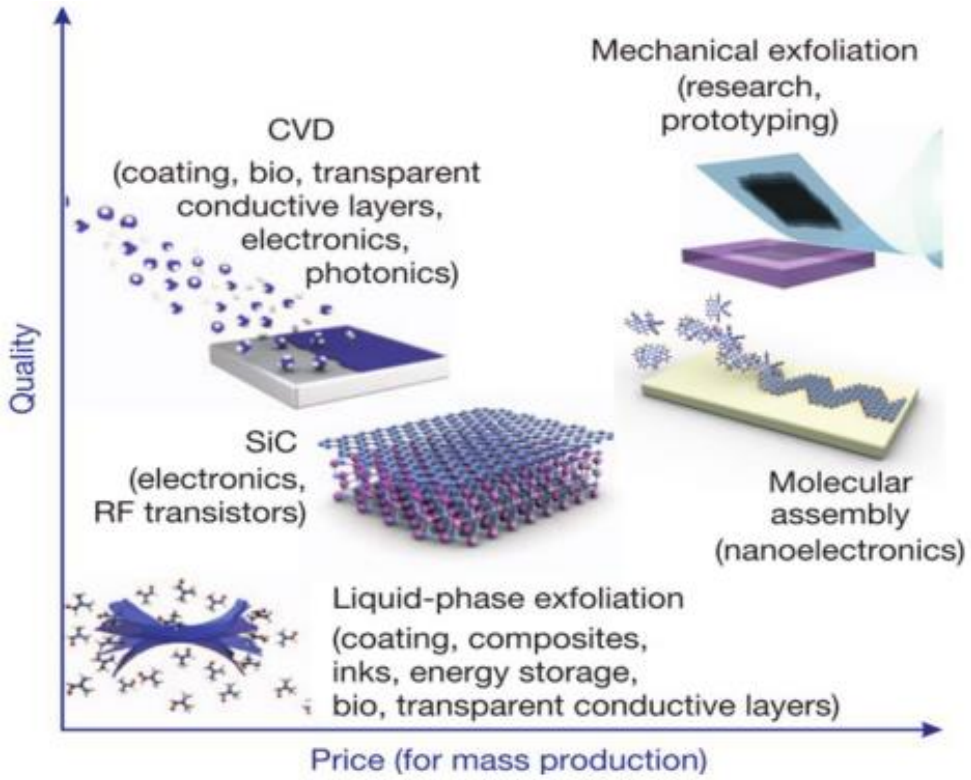

Figure 6 graphene production: representation of different techniques for graphene production including Liquid-phase exfoliation of graphite, chemical vapour deposition, mechanical exfoliation of graphite a molecular assembly[29].

2.3.1 Micromechanical Cleavage of Graphite

Micromechanical cleavage is a process of mechanically exfoliating graphite which reduces the number of layers. This can be achieved by using a tape that strongly attaches to the graphite and then can be peeled off. The graphite layers are held together by weak Van der Waals forces which means it cleaves along the interlayer direction instead of breaking the covalent bonds within the graphene layer. By repeating this process sufficiently, it can isolate a single layer of carbon atoms (Figure 7)[14].

The main advantage of the Micromechanical cleavage method is that it produces the finest quality of graphene in terms of crystalline domain size, number of defects and carrier mobility of up to 200,000 $cm^2V^{-1}s^{-1}$ [30–32].

The disadvantage of this methodology is the size of the graphene flakes produced are relatively small with a low single layer yield and therefore would be difficult to convert to large scale production. Additionally, the quality of graphene can be significantly affected by the process and the materials used, such as low-quality tape can lead to contamination reducing the carrier mobility. Currently, this process is only used for research purposes[33].

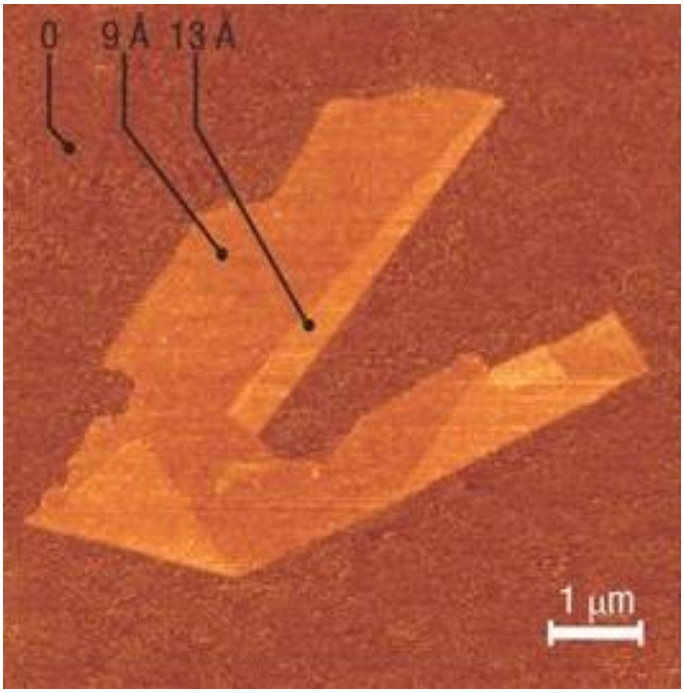

Figure 7 AFM topology of graphene: the image refigure the topology of folded pristine graphene isolated by Micromechanical cleavage[34]**.**

2.3.2 Chemical Vapour Deposition

An alternative method applied for the synthesis of graphene is chemical vapour deposition (CVD). CVD is one of the most effective processes to produce monolayer graphene in high quality and quantity that can be used in many different applications[35]. This method is achieved by exposing a metal substrate, such as copper, to high temperatures (>1000 °C) in the presence of a hydrocarbon precursor. The CVD process (Figure 8) begins with the breakdown of the precursor molecules, followed by the nucleation (new thermodynamic phase) of the carbon atoms into large areas on the substrate. Liquid Hydrocarbons precursors, like pentane[36] have been utilised as well as gaseous hydrocarbons such as acetylene, ethylene and methane[35].

There are many types of CVD produced graphene available, including plasma-enhanced, thermal and hot/cold wall CVD with the precise process of the growth of graphene being dependent on the metal substrate[37–40].

Other researchers have found that it is also possible use many other sources of carbon atoms, including insects and food waste[41].

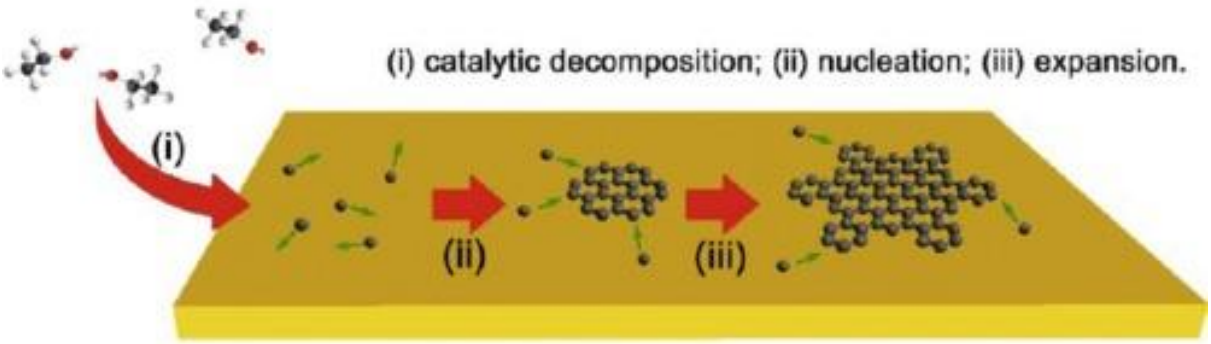

Figure 8 representation of CVD graphene grown on copper: (i) decomposition of the carbon source, **(ii)** nucleation on the Cu surface and **(iii)** graphene grown[42]**.**

CVD allows large areas of graphene to be prepared, however the graphene produced is polycrystalline. Therefore, graphene produced by CVD consists of relatively small areas (grains) randomly oriented and divided by grains boundaries (Figure 9) that reduce significantly the intra-grain carrier mobility[43]. Another disadvantage is related to the transferring process of CVD graphene from the growth plate to other substrate materials which is challenging and causes wrinkles, folding and cracks[44]. However, CVD remains one on the most reliable techniques to produce graphene for large-scale production for electronic applications, despite the aforementioned disadvantages and excessive energy requirements inherent to the current process conditions.

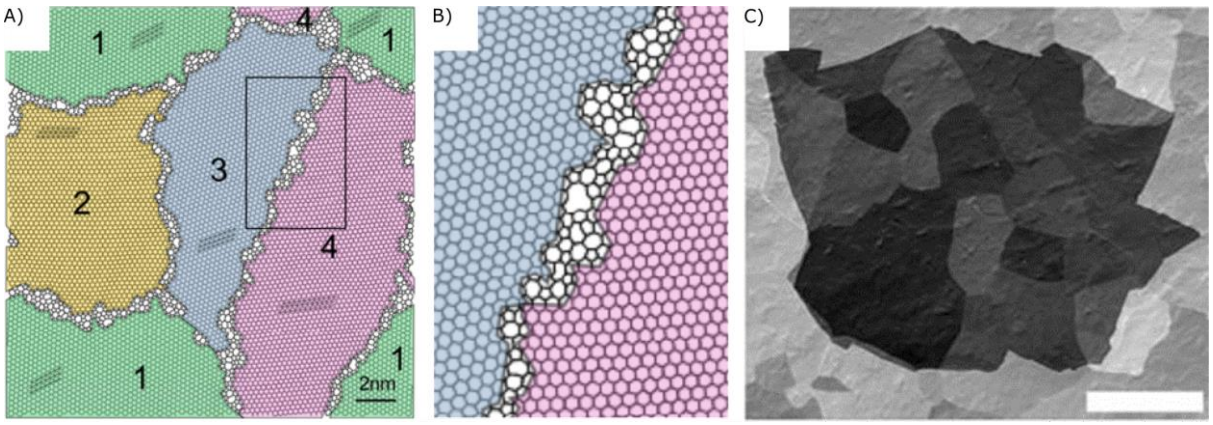

Figure 9 Representation of CVD polycrystalline graphene: A) simulation of polycrystalline graphene with graphene grains shaded in different colours[45]. **B**) Detail of figure (a) that highlight the binderies defects [45]. **C**) SEM image of polycrystalline monolayer graphene grown on Pt, scale bar 100 µm[46].

2.3.3 Liquid phase exfoliation:

The production of single layer graphene has been achieved by non-chemical solution-phase exfoliation by ultra-sonicating a graphite dispersion[47]. Hernandez et al. have utilised a range of solvents where the graphite-solvent interaction is comparable to graphite surface energy (Van der Waals layer interaction), therefore to exfoliate the graphite, only a minimum energy is required and is achieved through the sonication[47]. The monolayers produced consist of high quality and defect free graphene, however with a small mass yield of 1 wt% and relatively small flakes size less than few microns (Figure 10)[47].

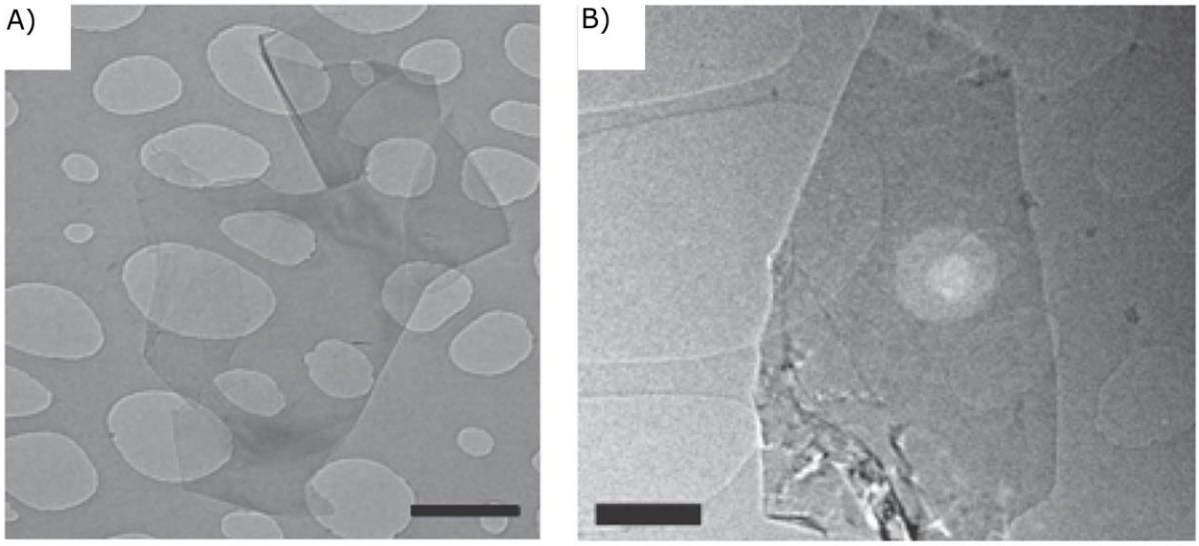

Figure 10 TEM images of graphene flakes produced via **non-chemical solution-phase exfoliation (A** monolayer graphene flakes **(B** bilayer graphene flakes (scale bars 500 nm)[47]**.**

A similar approach to Hernandez *et al.* was used by Paton *et al.*, producing a scalable, high quality and high quantity a few layers graphene by simply shear mix graphite in stabilising solvent, N-methyl pyrrolidone (NMP) a highly toxic chemical[48]. The nanosheets produced in this work were defect free and formed by less than 10 layers thick however, were relatively small, with a lateral flake size distribution of approximately only one micron (Figure 11).

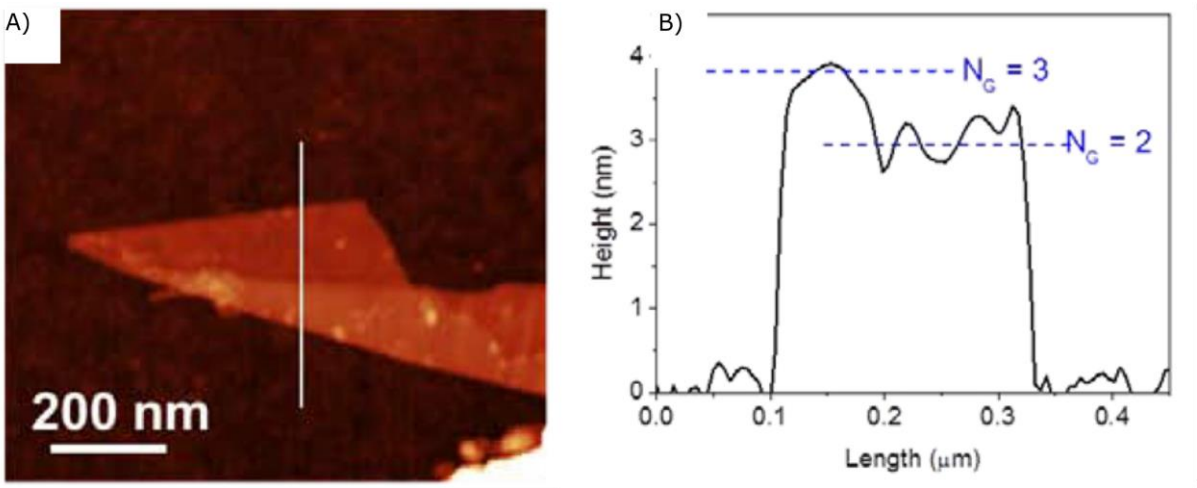

Figure 11 AFM image of Nano-sheet graphene produced via shear mixer AFM. A) AFM image of multi-layer graphene flakes. **B)** AFM profile multi-layer Graphene flakes [48]

Another possible route to produce graphene is through the chemical exfoliation of graphite in dispersion which is brought about by strongly oxidising graphite and subsequently exfoliating the material, producing graphene oxide (GO) (Figure 12). The graphene oxide produced is used as a material in its own right[49] or as a precursor for graphene synthesis by either chemical or thermal reduction process[50] to produce reduced graphene oxide (rGO).

It is important to highlight that the oxidation of graphite introduces a significant number of defects in the form of oxygenated functional groups and sp^2 lattice defects[51], that can strongly affect its mechanical and electronic proprieties[52]. On the other hand, the presence of these chemical species can provide a significantly advantage for different applications and makes GO extremely interesting from a synthetic chemistry point of view [50].

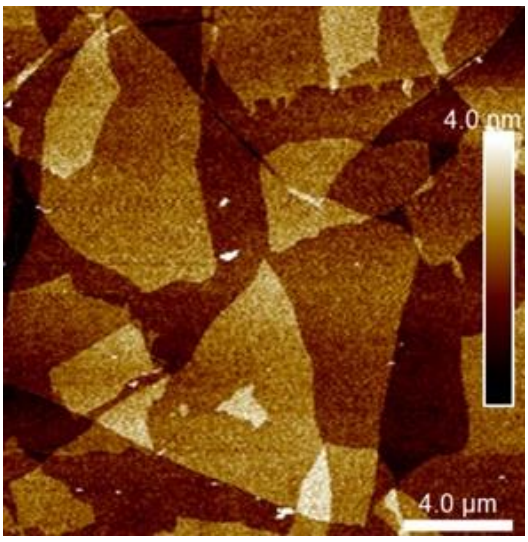

Figure 12 AFM topological image graphene oxide flakes onto SiO_2 that overlapped within each other[53]**.**

3 Graphene Oxide

3.1 Synthesis of Graphene Oxide:

The synthesis of graphene oxide was developed by British chemist Brodie in 1859[54], by mixing graphite with potassium chlorate and fuming nitric acid was able to synthesise graphite oxide and with retrospect, quite possibly the 2D counterpart, graphene oxide although he could not characterise it at the time.

40 years later Staudenmaier (1898), improved the Brodie graphite oxide synthesis by adding multiple aliquots of chlorate, instead of single addition. Subsequently, in order to increase the acidity of the mixture Staudenmaier used concentrate sulfuric acid which produced graphite oxide with a C:O ratio of 2:1 [55].

In 1958 Hummer and Offeman developed a different method to produce graphite oxide. In their method, graphite was oxidized in a mixture of concentrated sulfuric acid, sodium nitrate, and potassium permanganate at 45˚C for two hours, achieving a similar C:O ratio. Nowadays, Hummer's method is most common route to synthesis GO [56,57]

Several other methods have been developed, however, these three methods represent the major routes to synthesising GO. The GO produced strongly depends on reaction conditions, the specific oxidants used and on the initial graphite source [5] which can lead to a variety of GO materials being produced and reported on with varying properties[58].

3.2 Oxidation process:

Graphite intercalation compound (GIC) chemistry has been explored for almost 150 years[59] however, only recently with the advent of graphene and it has become extremely relevant as a possible route to produce graphene based materials[60].

Graphite, due to it is layered structure, allows species such as molecules, ions and atoms (called intercalates) to be laid in between the layers. The intercalation reaction weakens the interlayer attraction between the graphite layers therefore, increasing the distances between the adjacent layers from 3.35 Å to 6.8 Å [61]. Moreover, the space of the adjacent graphite layer can vary significantly by the amount of water presents in the sample that can lead to a successive increase of the distance between the layers [61].

The exfoliation of graphite intercalation compounds can be achieved by mild sonication, producing graphene oxide if oxidised during the intercalation process[62–65].

The intercalation with halogen compounds allows a precise control of numbers of layers in the final GO. For instance, it is possible intercalate every layer of graphite:, producing intercalated graphene at every layer (stage I GIC); or intercalated every second layer(stage II GIC); or third layer(stage III GIC), producing bilayer and trilayer graphene respectively[66].

3.3 Reduction of Graphene Oxide:

GO can be considered as an intermediate stage for graphene production by chemical, thermal and electrochemical reduction processes.

The reduction process of the GO is extremely important as it has a huge impact on the quality of the reduced graphene oxide (rGO) produced. A high quality rGO means that the π -electron structure of the graphene is partially restored and with it, some of his superior proprieties [67].

3.3.1 Chemical reduction:

A common route to chemically reduced GO involves the use of hydrazine, a highly toxic chemical [68], Additionally, Shin *et al.* (2009) showed that hydrazine can partially functionalize the GO flakes with nitrogen atoms [69]. A big effort has been made to find alternative chemicals to hydrazine that are able to strongly reduce GO. In 2010 Moon *et al.* was successful in reducing GO by using a solution of hydriodic acid and acetic acid(HI-AcOH), at low temperature (40°C)[70,71]. Furthermore, Fernández-Merino *et al.* reduce GO in a comparable way as the hydrazine by using a solution of ascorbic acid a safety and innocuous chemical[72].

Chemical reduction processes have the advantage of being a very scalable methods however, the chemical reduction compromises the proprieties of the rGO in terms of electronic conductibility and stability in water surface area [73].

3.3.2 Electrochemical reduction:

Electrochemical reduction of GO is a potential route to production that consists of depositing a thin film of GO on a substrate, such as indium tin oxide (ITO) or glass and then creating a circuit through the GO by using two electrodes. This method produces a very high-quality rGO in terms of structure, almost identical to pristine graphene, and high conductivity: 8500 S/m, higher then silver. Another advantage of this technique is that it does not use hazardous

chemicals, however, it has not been possible to find a way to scale up this process due to the difficulty in depositing GO in bulk quantity onto the electrodes [74].

3.3.3 Thermal Reduction:

Thermal reduction is a process to highly reduce GO, through exposing GO elevated temperatures ~1000°C. A disadvantage of thermal reduction is that it introduces vacancies, defects and imperfections in the rGO produced [5]. This is due to the release of CO_2 and CO that can affect the mechanical and electrical proprieties of GO. However, thermally reduced rGO has a very high surface area and bulk conductivities of 1000–2300 S m^{-1} indicating an effective GO reduction [5,75,76].

Although the superior proprieties of graphene are strongly diminished in graphene oxide (GO), the relatively facile synthesis and their unique properties make it appealing for several applications and fundamental research.

The polar oxygen functional groups render GO hydrophilic, therefore dispersible in water another polar solvents [60,77,78]. Aqueous GO dispersions can be easily deposited via drop casting, spray and spin coating onto a range of different substrates, in order to create thin films. These thin GO film can be reduced and therefore can become electrically conductive [68,79]

The oxygen species present on the surface of GO can be used as sites for chemical modification and functionalisation, altering the physiochemical properties of GO itself [80]. For example modifying the chemical composition of GO can change it from an insulator to semi-conductor and semi-metallic material [80–82].

GO is also used for reinforcement in composite materials to enhanced their physical proprieties [2,3].

3.4 Graphene Oxide Structure:

3.4.1 Models of Graphene Oxide

The main difference between GO and graphene consists of the hybridisation of the carbon atoms. In pristine graphene, each carbon atom is hybridised sp^2 originating in a perfect honeycomb-lattice; where in GO there is the presence of a large number of sp^3 hybridised carbon bonds that are covalently bonded with oxygen functional groups (Figure 13)[65,83]. This causes the oxidised regions to perturb the original lattice of graphene sheet. These oxidised areas are randomly displaced on the surface of individual GO flakes [51].

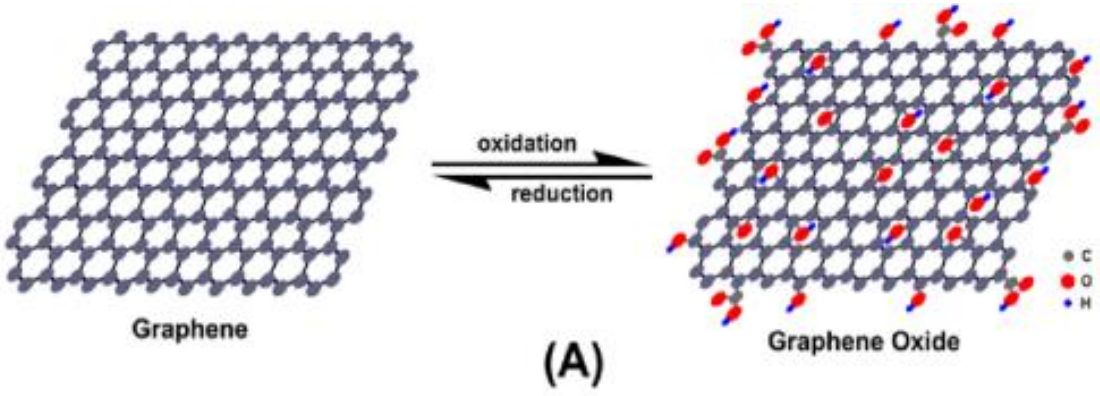

Figure 13 representation of pristine graphene lattice and graphene oxide lattice. A) illustration of Graphene lattice **B)** illustration of Graphene oxide lattice [84]

Several structures of GO models (Figure 14) have been proposed during the last 80 years however, the GO structure has not yet been elucidated[5,65,85,86]. This is primarily due to the nonstoichiometric chemical composition, variance in production methods, and the absence of sensitive characterisation techniques for an unambiguous indication of the chemical species on GO flakes[4,5,78].

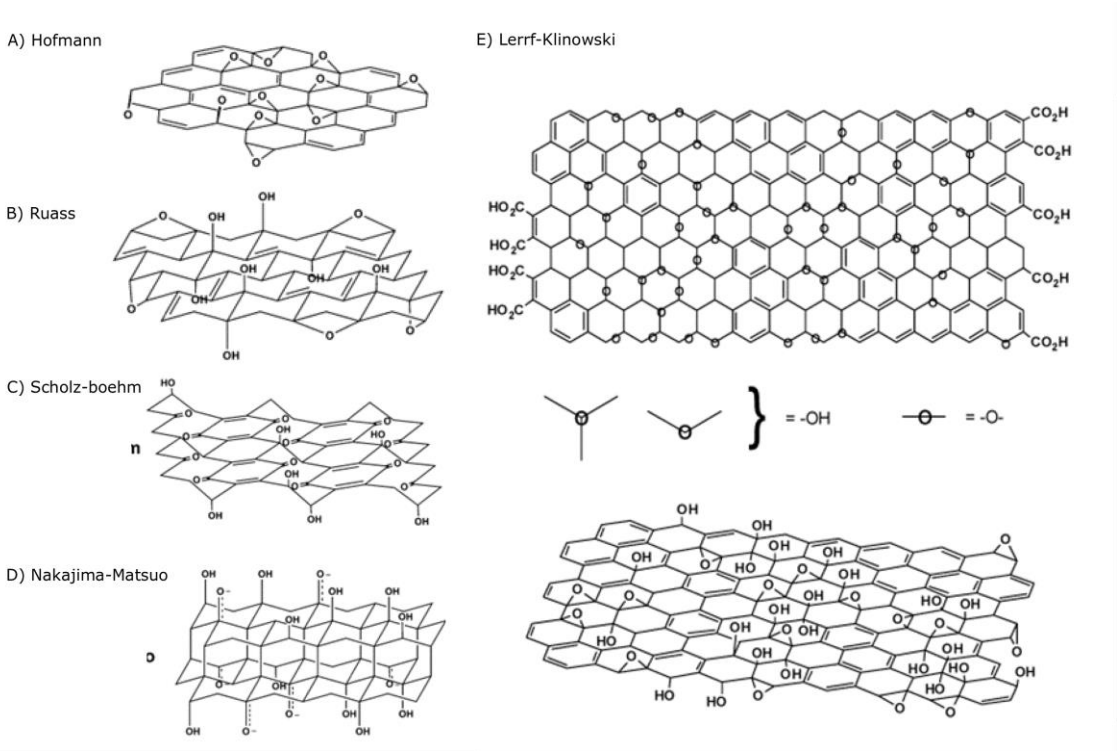

Figure 14 summary of the different GO models proposed: **A)** Hofmann, **B)** Ruess, **C)** Scholz-Boehm, **D)** Nakajima-Matsuo **E)** Lerf-Klinowski, the majorly accepted structural models[65].

According to the most commonly accepted structural models, that proposed by Lerf and Klinowski (Figure 14)[65], GO flakes are made of a single layer of carbon atoms decorated with oxygen functional groups. On the basal plane there are mainly hydroxyl and epoxy groups, while at the edge and out of plane there are carboxyl, carbonyl, phenol, lactone and quinone functional groups[82,87] but this is still the subject of some debate[65].

3.4.2 Current techniques for Characterisation of GO Structure

To investigate the GO structure in greater detail, various microscopic and spectroscopic characterisation techniques have been performed. The thickness of GO has been detected by atomic force microscopy (AFM) as approximately 1 nm (Figure 15)[84,88–90]. Furthermore, by using a conductive AFM it has been possible to detect the electrical defects on the GO surface[91].

The structural features of GO flakes have been further examined through scanning tunnelling microscopy (STM), where it has been possible to observe the lack of ordered lattice due to the presence of oxygen groups (Figure 15) [84,90,92].

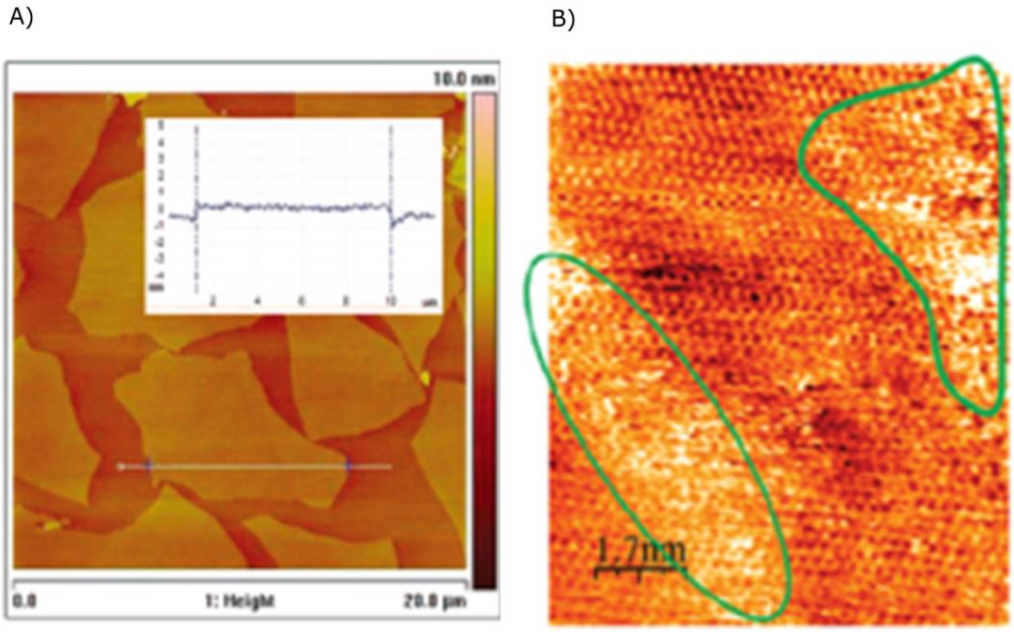

Figure 15 AFM image and STM images of GO. A) Topological map of graphene oxide flakes and measurement of GO profile, approximately 1 nm. **B)** Monolayer GO STM images deposited onto highly oriented pyrolytic graphite substrate [84].

The direct observation and quantification of the structural defects (holes, graphitic regions and oxidised regions) in monolayer GO has been achieved by using high-resolution transmission electron microscopy (HRTEM) (Figure 16)[52,93–95]. Erickson e*t al.* (2010) proposed that the holes (2%) in GO flakes are formed during the oxidation and exfoliation processes due to the liberation of CO and $C0_2$. The graphitic regions (16%) are areas that preserve the graphene structural lattice and are formed by an incomplete oxidation process. The disordered regions of the basal plane consist of highly oxidized regions (82%) where each

carbon atom is most likely to be oxidized with no well-defined functionalities in general hydroxyls, epoxied and carbonyls.

Further research has used aberration-corrected HRTEM to exploit the topological defects in GO, such as in-plane distortions, strain in the surrounding lattice and dominant clustered pentagons and heptagons[52].

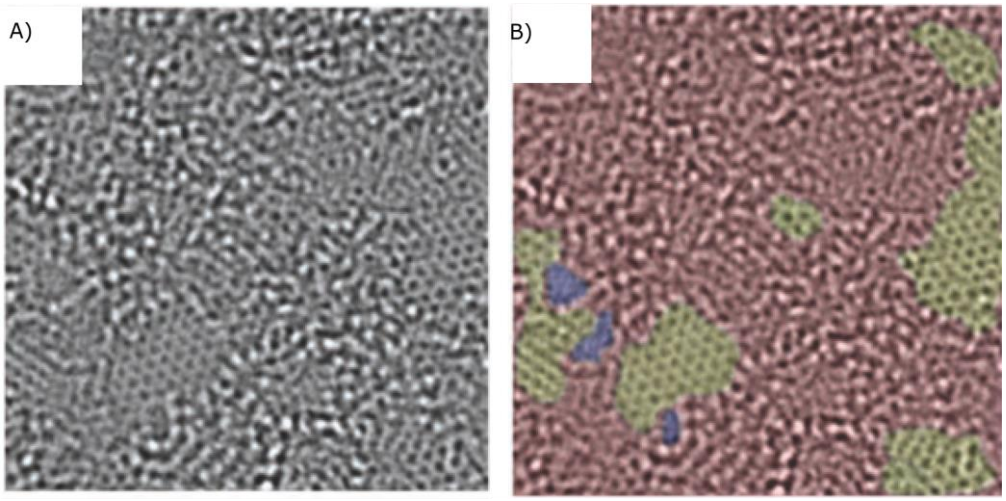

Figure 16 Aberration-corrected TEM images of suspended monolayer GO. A) TEM image of Single layer of suspended GO**. B)** Highlighted in yellow the graphitic areas, in blue the holes and in red the disorder regions, indicating the presences of oxygen functionalities[93]**.**

By using a scanning transmission electron microscope (STEM) combined with electron energy loss spectroscopy (EELS), further supports the consensus that the oxygen atoms are randomly distributed to the GO flakes and the carbon atoms attached to the oxygen atoms are hybridized sp^3(Figure 17) [96].

While these resolution microscopy techniques give valuable insights into the nanoscale structure of graphene oxide, the techniques are prone to damaging the sample with high energy electrons, only image an small area and employ ultra-high vacuum therefore may not always be directly compared to analysis in ambient conditions.

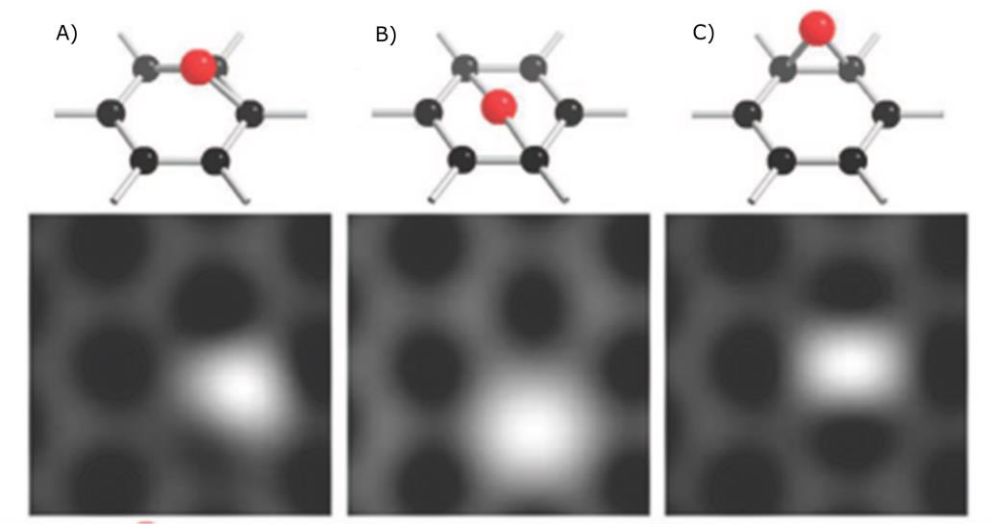

Figure 17 STEM images of graphene oxide, A-C) the images show in white the oxygen atom bonded to the graphene lattice, the ball-stick models represented the possible structures for each pictures [96].

3.4.3 Chemical characterisation techniques

One of the most powerful techniques to chemically characterise GO has been solid state 13C magic angle spinning NMR. The NMR spectra identifies three main peaks (Figure 18); the first peak around 60ppm is assigned to the carbon atoms bonding to the epoxy group; the second peak at 70 ppm is to identify the carbon bonded to hydroxyl group; the last peak around 130pp is attributed to the graphitic sp^2 carbon[86,97]. High resolution C- NMR was able to detect thee other small peaks assigned to lactols (101ppm), ester carbonyls (167ppm) and ketone groups (191ppm)[86]. The spatial resolution of 13C NMR itself is only limited to the order of microns and therefore cannot give this information at smaller resolutions currently.

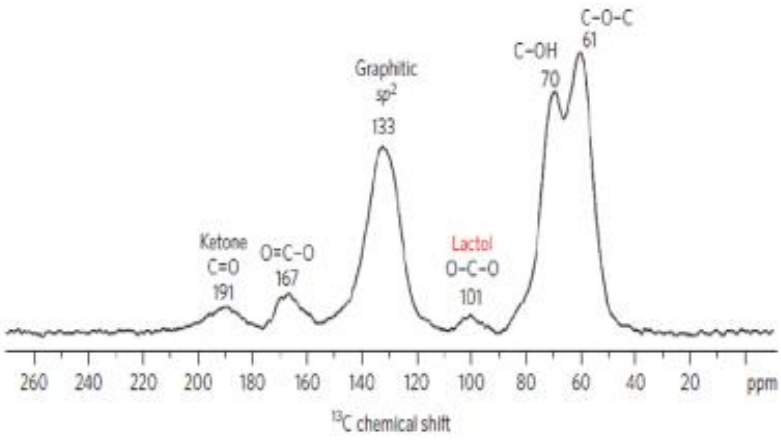

Figure 18 GO Solid state 13C magic-angle spinning NMR spectra of GO. The spectra show the three strong peaks relate to graphitic sp^2, C-OH and C-O-C. Moreover the spectra display three broader peak assigned to ketone, O=C-O and O-C-O [86].

X-ray absorption near-edge spectroscopy (XANES) experiments reveal information regarding the degree of carbon bond hybridisation, namely sp^2 and sp^3. In addition, it gave information about the bonding configurations of the functional atoms and the degree of alignment of the graphitic region in GO [98] but again has micron spatial resolution.

XPS analysis quantify the different states of the Carbon Oxygen bonds: unoxidized carbons (sp2 carbon), C-O, C=O and COOH. The C1s peaks can be de-convoluted into sp^2 carbons in aromatic rings, C-OH, C-O-C, C=O and COOH (Figure 19)[80,98,99].

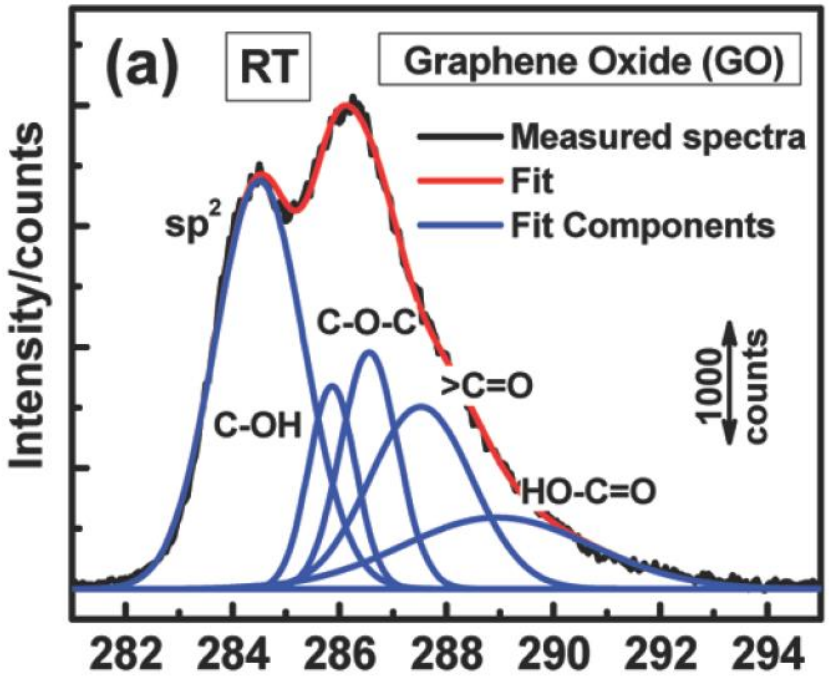

Figure 19 high resolution C1s XPS spectra of Graphene Oxide. Through the deconvolution of C1s it is possible quantify the chemical oxygen species (aromatic rings, C-OH, C-O-C, C=O and COOH) present in sample[98].

By dividing the area of the C2p peak by the C1s peak area it is possible to determine the sp2 carbon fraction and monitor the degree of oxidation in GO during reduction condition. The O1s peak can provide additional/similar information as C1s [80,98].

Raman spectroscopy gives important information regarding the degree of disorder in the sp^2 carbon lattice and therefore the degree of oxidation from sp^3 bonding. A typical spectrum (Figure 20) of GO shows a D-Band (~1340 cm^{-1}) and broad G-band (~1580 cm^{-1}) the former generated by the structural imperfections, more precisely by the in-plane oxygenated groups. The G-band (~1580 cm^{-1}), characteristic of all sp2 carbon lattices, is generated by single phonon scattering in the E2g phonon modes of graphite in the centre of the first Brillouin

zone [99,100]. The D peak is due to defect scattering in the basal plane. By calculating the ratio of the D and G band intensities (ID/IG) it is possible to quantify the quality of the sample [80,100] although it stops at giving further structural elucidation than this due to the spatial resolution and different physical processes contributing to the intensity, peak width and positions of the D-band and G-bands. By employing visible light, the resolution on a conventional Raman spectrometer is around 500 nm[101].

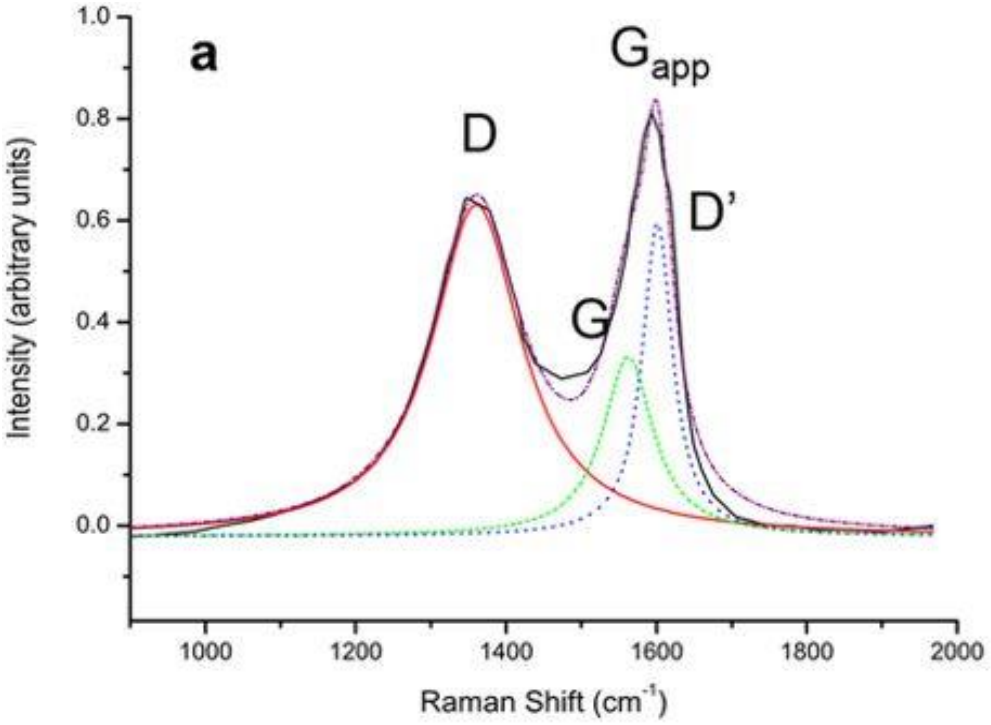

Figure 20 Raman spectrum of Graphene Oxide [102]

FTIR analysis has a fundamental role in characterising the bulk GO functional groups and has been investigated in great detail by Acik et al. [103].

In this work, Acik et al. found that the IR absorbance spectra of multilayer GO produced via the Hummers method (Figure 21) leads to three broad peaks at 3000-3700 cm^{-1}, 1500 -1850 cm^{-1} and 800-1330 cm^{-1}. These broad peaks are the result of complicated overlapping of the IR vibrational mode of IR active species. In addition, there is a substantial shift in frequency related to proximity and conjugation effects [103].

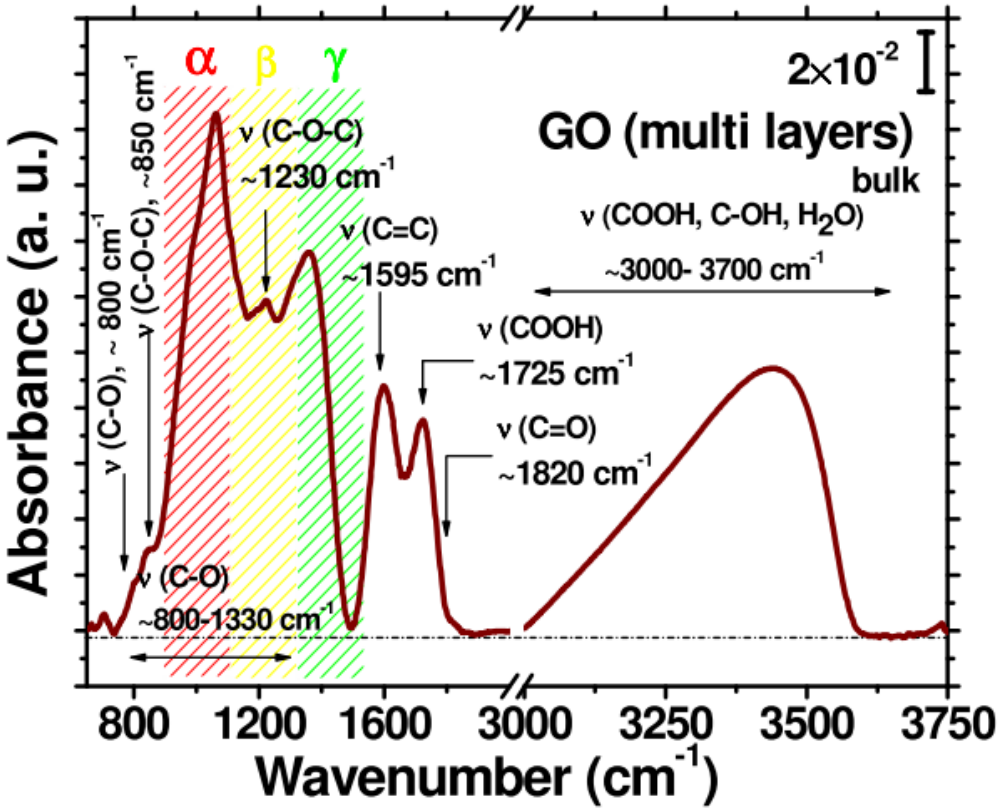

Figure 21 Bulk FTIR spectra at room temperature of multi-layer graphene oxide[103].

The broad peak at 3000-3700 cm^{-1} was assigned to the IR radiation absorption of several oxygen species, mainly hydroxyl groups (both basal plane and at the edge) and from additional contributions of C-OH attributed to carboxyl groups (~3550 cm^{-1}), five-member-ring lactols (~3619 cm^{-1}) and water intercalated between the GO flakes [103].

The IR peak at 1500 cm^{-1} to 1850 cm^{-1}, is the result of the overlap between the sp^2-hybridized C=C asymmetric stretch (1500 to 1600 cm^{-1}) and the stretching of ketones and 1,3 benzoquinones. The bands between 1600 and 1750 subsist IR signal domination of C-OH vibrational modes related to the carboxyl group (COOH) onto the C=O of the ketones (1600 to 1850). Moreover, in that spectral region 1600-1750 cm^{-1} subsists a contribution from H_20 scissor mode occurs (water molecules physiosorbed on the GO surface membrane or trapped between the GO flakes) [103].

The broad peak that covers the whole fingerprint region (800-1500 cm^{-1}) is generating by the contributions of several IR active species. It is possible to be divided into three regions: 900-1100 cm^{-1}, 1100-1280 cm^{-1} and 1280-1500 cm^{-1} [103].

From 900 to 1100 cm^{-1} the IR vibrational mode ethers (peroxides, furans and dioxolanes) dominate this part of the spectra, with weak contribution of hydroxyls and carboxyls. Between 1100 to 1280 cm^{-1} weaker absorption of ketones (pyrenes and γ-butyrolactones) overlapping the peroxides (1267 cm^{-1} and 1185 cm^{-1}) and pyrans (1103 cm^{-1}). Between (1280 to 1500 cm^{-1}) the most contributions arrive from epoxides (1280 -1320 cm^{-1}), ketones and 1,3-benzoquinones (1453-1523 cm^{-1}).

The epoxides show also some weak vibrational modes at (1070 cm^{-1} and 1170 cm^{-1}) and additional contribution at 850 cm^{-1}, five-membered ring lactols (949 cm^{-1} and 1131 cm^{-1}), dioxanes (1036 cm^{-1} and 1064 cm^{-1}) and weak vibrational modes of carboxyl (1081 cm^{-1}) and hydroxyls (1040-1095 cm^{-1}).

Moreover, Acik *et al.* also demonstrated the thickness dependence of the GO IR absorption spectra. They proposed that this effect could be related to a different concentration of the IR active species in each sample and/or the change of the proximity and conjugation of the oxygen species. In addition, the presence of water molecules intercalated between the layers or physiosorbed onto the surface could lead a significant broadening of the peaks[103,104].

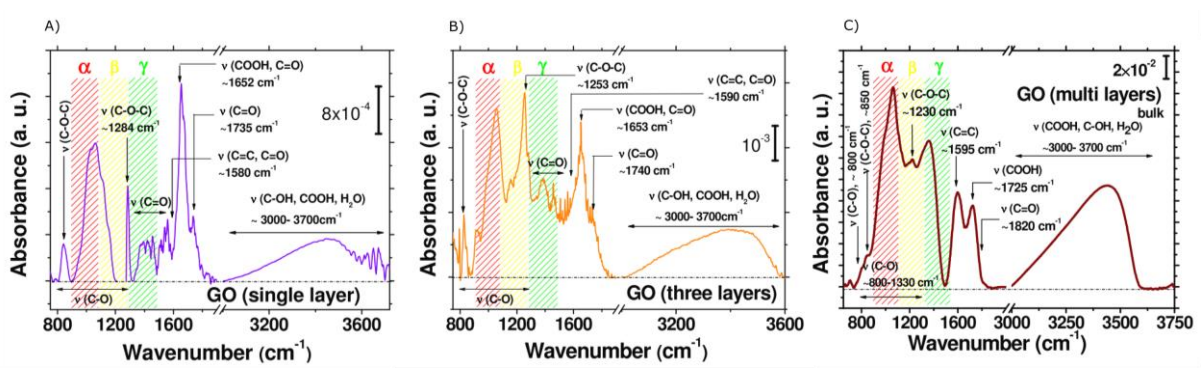

Figure 22 thickness dependency of GO FTIR spectra[103] **A)** Monolayer GO FTIR spectra. **B)** Three layers GO FTIR spectra. **C)** Multilayer GO FTIR spectra

3.5 Atomic Force Microscopy Infrared Spectroscopy

Infrared spectroscopy (IR) is one of the most commonly used, reliable and well-known analytical techniques for chemical characterisation, however, the main drawback in IR spectroscopy is the spatial resolution is limited by diffraction to 2.5 to 20 µm[105].

Over the past decades, a great effort has been made to improve the spatial resolution of the IR spectroscopy to greater than the optical diffraction limit, most of these approaches are through the coupling of a scanning probe microscope with an IR source [106–108].

In 1999 Hammiche *et al.* was the first to overcome the diffraction limit of IR spectroscopy by combining an FTIR with a scanning thermal microscope [109]. The detector was a miniature temperature sensor designed to measure the temperature fluctuation onto the surface sample, induced by the IR absorption[109].

One year later Anderson (2000), coupled a commercial FTIR and an atomic force microscope (AFM) and he was the first to measure the tip deflection due to the thermal expansion of the sample[110]. Subsequently in 2004, Hammaiche *et al* acquired the first thermal expansion spectrum [111]. Dazzi and co-workers in 2005, designed one of the most successful IR nanoscale characterisation instruments, by coupling an IR tuneable source and a commercial contact mode AFM, from here came the name AFM-IR[112].

The Dazzi AFM-IR technique required the sample to be deposited onto a ZnSe prism and illuminated through the prism with IR irradiation via total internal reflection (Figure 23). The induced photo thermal expansion on surface of the sample is then detected by an AFM tip. It was demonstrated that with this setup, it was possible overcome the diffraction limit of the IR spectroscopy and have a spatial resolution less than 100 nm [112].

Moreover, the Dazzi AFM-IR setup prevents any unwanted cantilever thermal expansion, as the tip is not directly illuminated by the IR laser beam [113].The only drawback of this technique is that the sample must have sufficient thickness to detect the thermal expansion of the sample and needs an IR transparent substrate[113].

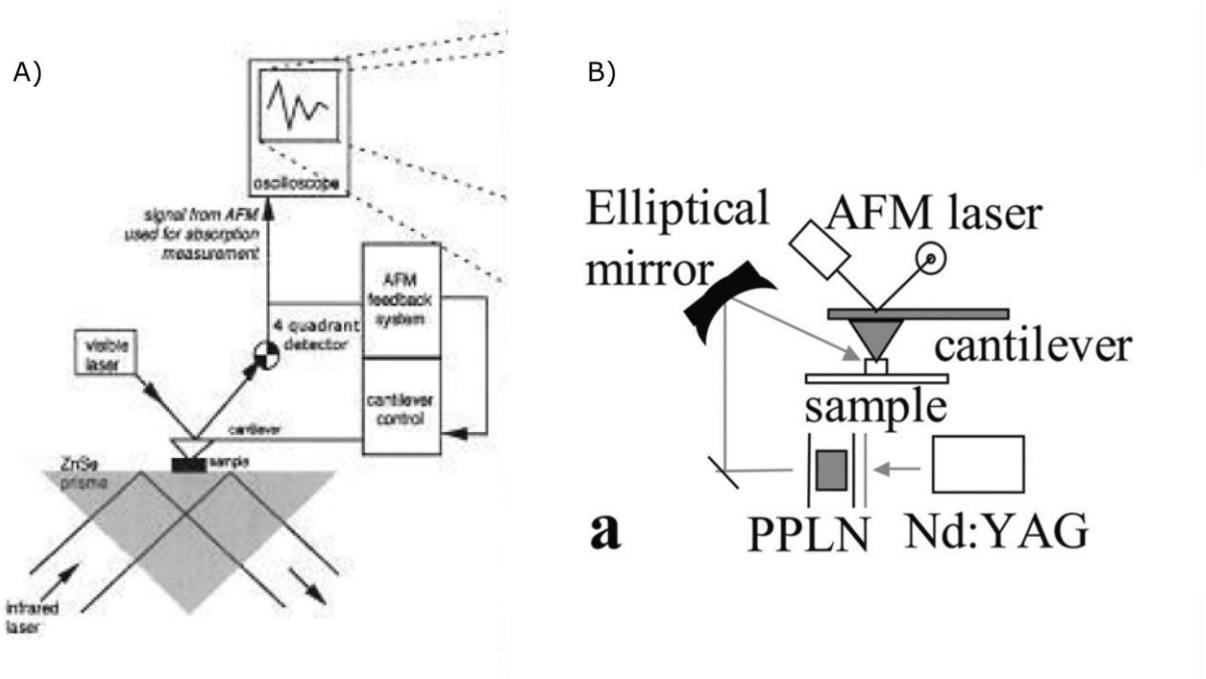

Figure 23 Experimental setups of AFM-IR :A) Experimental setup of the AFM-IR designed by Dazzi in 2005[112], the sample is irradiate via total internal reflection**. B)** Experimental setup of the AFM-IR designed by Hill *et al.* in 2005[114].

In 2009 Hill *et al.* proposed a different AFM-IR setup (Figure 23) [114], based on induced resonant motion phenomena, that enable the simultaneous acquisition of IR amplitude map and topography images, with a spatial resolution of approximately 200 nm. In contrast to the method designed by Dazzi *et al. (2005),* the sample surface is targeted by a 'top-down' IR beam, allowing a surface characterisation of any sample. The main disadvantage of this top-down illumination setup is that the AFM tip inevitably absorbs the radiation which generates additional peaks related to the thermal expansion of the tip [114].

Over the past years, the sensitivity of the instrument has been improved and therefore commercialised. The first version of the AFM-IR commercialised was based on both the 2005 Dazzi *et al.* AFM-IR setup[112] and 'top-down' variant[113]. Since then, the acquisition times have been significantly reduced by introducing an optical parametric oscillator laser sources with a repetition rate of 100 nm[115,116].

Dazzi *et al.* demonstrate that the thermal expansion of the sample is linearly proportional to the absorption coefficient of the sample. However, the AFM-IR signal strength depends also on the other sample proprieties , such as thermal expansion coefficient, heat capacity, density and modulus [105].

Lu *et al.* in 2011 used a quantum cascade laser (QCL), that allow an easy tuning of pulse length and the repetition rate[117]. By matching the repetition rate of QCL with the contact mode resonances of the AFM cantilever, they demonstrated that it was possible to improve drastically the sensitivity, the spatial resolution (<50 nm) while using a low-power illumination[117]. This discovery lead to a new AFM-IR mode, called "resonance enhanced AFM-IR" [105]. Moreover, the same group demonstrated that by using a metal-coated (generally gold) tip and substrate, it is possible to enhance the AFM-IR sensitivity even more[117]. This enhancement has been called "lightning rod effect" and is generated by a focused and intensified local electric field of the IR radiation at the apex of the tip (Figure 24). The "lightning rod effect" has led to subsequent improvements of spatial resolution, limited only by the AFM tip apex size (20nm). Additionally it has been possible to characterise samples as thin as 5 nm and even 2 nm self-assembled molecules [7]. Therefore, AFM-IR has the potential to become one of the main spectroscopic techniques for chemical characterization of 2D materials that are IR active[4,118].

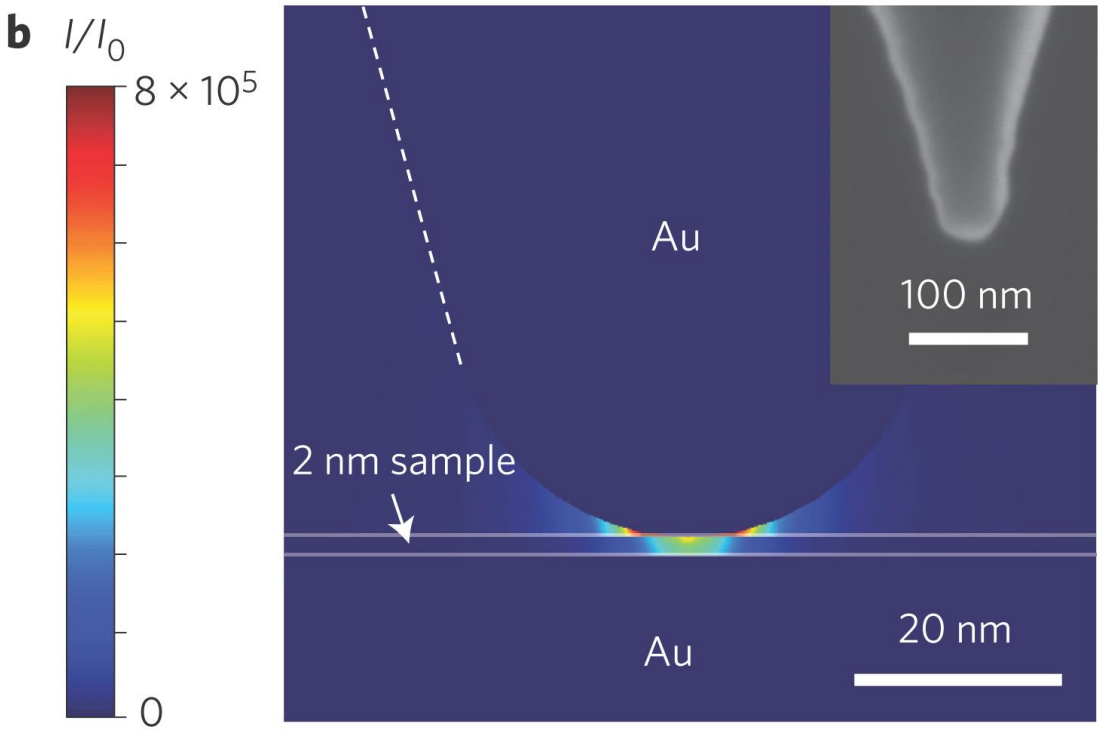

Figure 24 three dimensional simulation of lightning rod effect for a 2nm-thick molecular monolayer on gold[7].

Currently only one paper has been published regarding the characterisation of GO using Contact mode AFM-IR[118] As the thickness of GO is extremely low, 1 nm thick, the thermal expansion of the sample is tremendously low and IR amplitude spectra acquired (Figure 24.1 C), results in an poor signals and it is almost impossible to distinguish if the signal is coming from the substrate or from the GO itself. Despite the poor signal that is coming from the sample, IR amplitude maps generate enough contrast to distinguish this small signal, especially in the C-O region (1080-1200 cm-1) (Figure 24.1 A) however, in the spectrum region (1500-1700 cm-1) the signal is so low that the IR amplitude of the of the monolayer GO flakes blends in with the background (Figure 24.1 B).

Resonance-enhanced CM-AFM IR have the potential to increase the sensibility of the instrument, however as this method is relatively new, there has not been any published work using this techniques to characterise materials thinner as 1 nm.

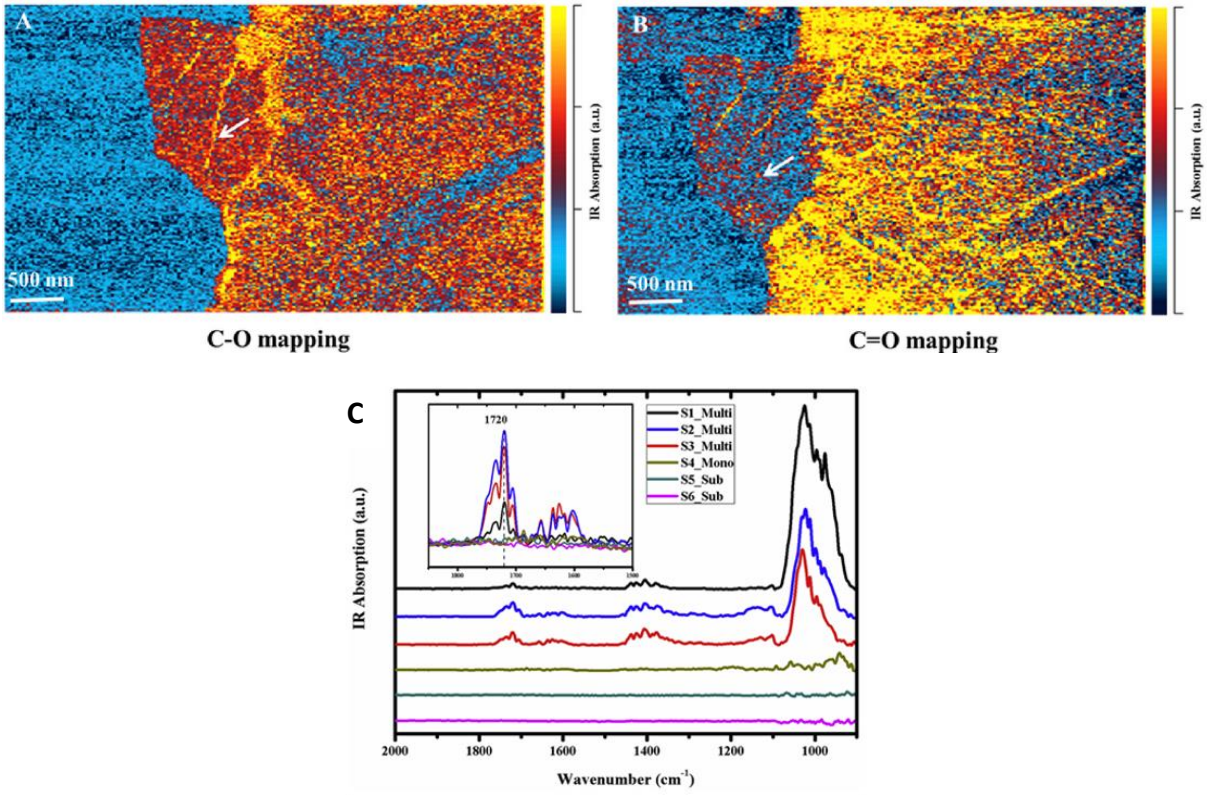

Figure 24.1 IR amplitude maps : A (1080) and B (1720 cm^{-1}) and IR amplitude spectra and acquired by Liu *et al. 2018* of multilayer and monolayer GO [118].

4. Experimental Principles and Procedures

4.1 Techniques

4.1.1 XPS Spectroscopy

X-ray photoelectron spectroscopy (XPS) is one of the most reliable surface sensitive characterisation techniques for a quantitative identification of the chemical composition of the sample surface. XPS is based on the photoelectric effect described by Einstein (1905)[119] and developed 1950 by Siegbahn *et al.*, awarded with the noble prize for physics in 1981[120].

The X-ray beam is shone onto a sample. The surface atoms absorbed the radiation, and if the radiation has enough energy, the external shell of the electrons will be ejected. By quantifying the kinetic energy and the number of electrons that are expulsed from the materials it is possible acquire information regarding the nature of the chemical bond and the surface elements.

XPS can provide information only from the surface as the electrons are ejected only between the top layer and 10 nm in depth.

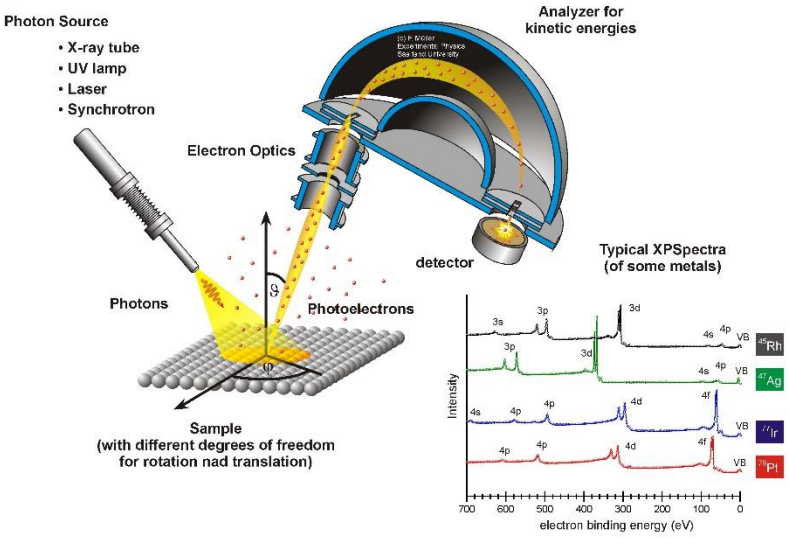

Figure 25 representation of XPS setup [121]

4.1.2 RAMAN Spectroscopy

Raman spectroscopy[122] is a powerful and non-destructive characterisation technique, which provides electronic and structural information of the crystal sample.

Raman spectroscopy is based on the inelastic scattering of a light by phonons in the sample. The elastic scattering (Rayleigh effect) occurs when the photons by interacting with the sample change only its direction where their energy remains invariant. In the inelastic scattering there is a change in the direction and in the photons' energy that leads in an increase or a decrease of the scattered photon energy.

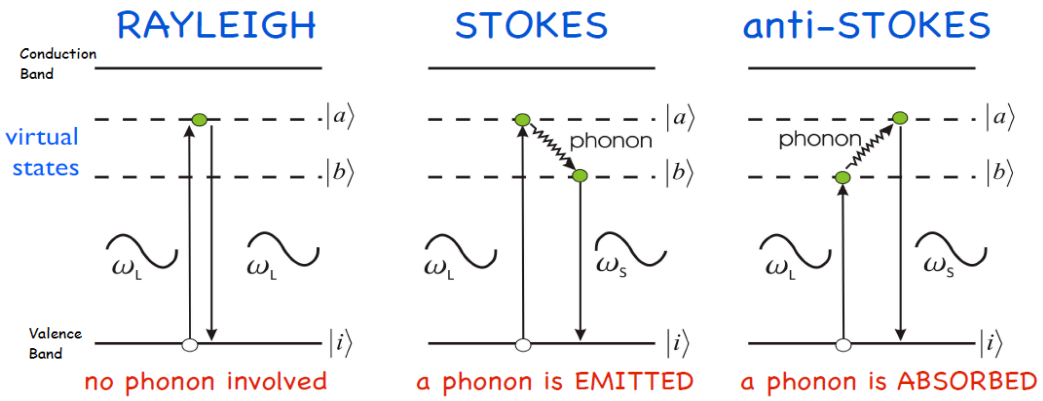

Figure 26 representation of the different light scattering processes in a semiconductor: Rayleigh and Raman (Stokes and anti-Stokes scattering)[123]

Raman Scattering is well described in terms of electronic transition as the interactions between the incident light and phonons is extremely weak compared to the coupling between the incident radiation and the sample electrons. When electrons have been excited to a virtual state by the incident radiation light, it can absorb or emit a phonon which causes an increase or a decrease of its relative energy, respectively (Figure 26). Subsequently, when the excited electron returns to the ground state it emits a photon. If the emitted photon is lower in energy in respect of the incoming photon due to phonon emission, the process is called Stokes Scattering. Vice versus, if the emitted photon has higher energy due to phonon absorption then the emitted photon is called anti-Stokes scattering. Raman scattering is observed when the outcoming photon is shifted in energy due to this transition. Typical Rayleigh scattering does not effect the energy of the emitted photon therefore no measured effect can be observed.

The laser beam is targeted downwards towards the sample, in general with a visible radiation. The radiation emitted from the spot onto the sample is focused by using a lens through a monochromator. The Raman scattering, typically really weak (~1 per 10^6 photons), is separated by a filter (notch or edge pass filter) from the Rayleigh scattering and subsequently detected.

Raman spectra are obtained by plotting the intensity of the scattered light as a function of the "Raman shift", defined as the difference between the incoming (incident) and emitted (scattered) photon energy.

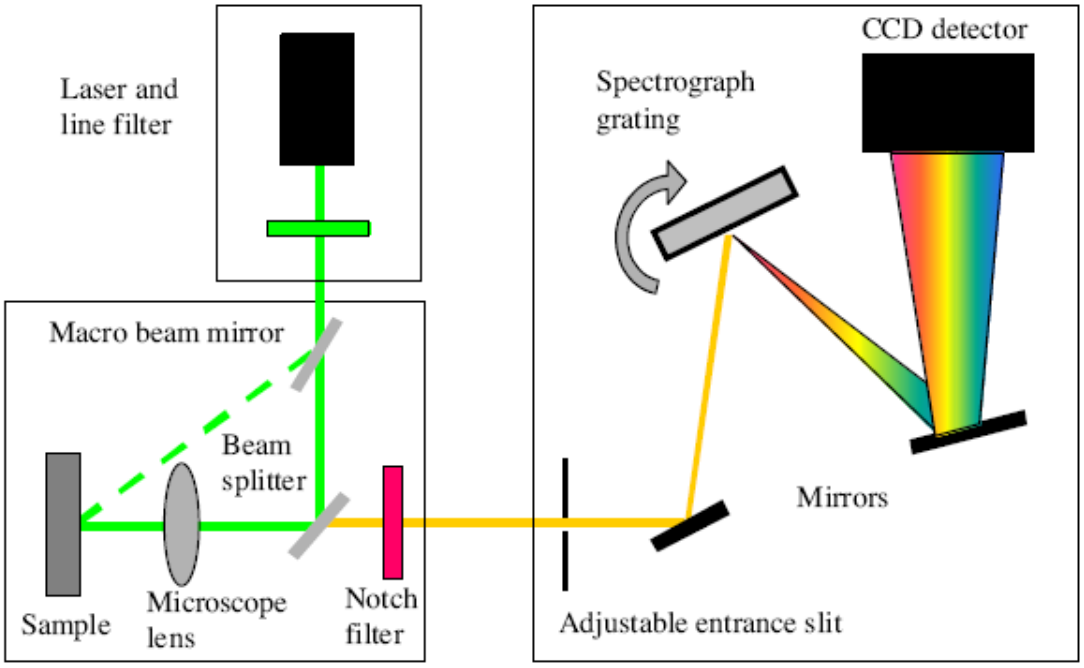

Figure 27 Representation of Raman spectrophotometer [124]

4.1.3 Scanning Electron Microscope Spectroscopy

Scanning electron microscope (SEM) is used to produce sample images by scanning the surface with a focused electron beam. The interaction of the electron beam and the sample atoms generate several signals that contain information regarding the surface topography and composition of the sample. The electrons beam can be focused onto the sample using an electron magnetic field and the sample is scanned in in a raster scan pattern. Combining the position of the beam with the detected signal produces high resolution images,

improving as the limit of diffraction of the photon-based microscopy, 400 nm, by employing the De Broglie phenomenon for the wavelength of electrons[125].

There are several SEM modes. The most common mode is the detection of emitted secondary electrons of the sample atoms while excited by the beam (Figure 28).

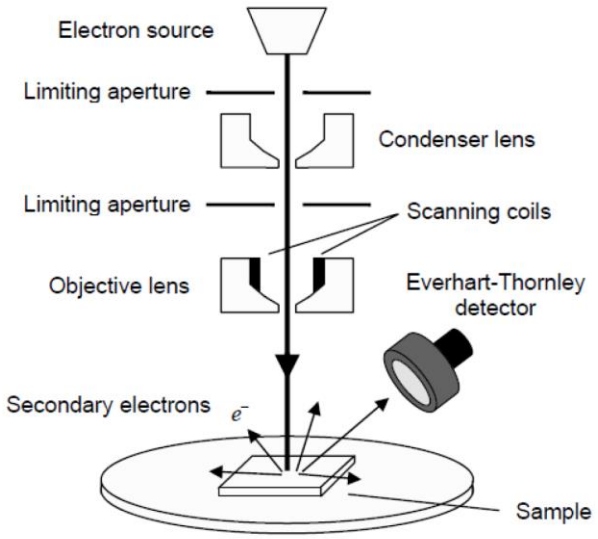

Figure 28 schematic diagram of an SEM setup [126]

4.1.4 IR Spectroscopy

Infrared spectroscopy (IR) is one of the most important, reliable and well-known analytical techniques. IR spectroscopy studies the vibrational mode of the atoms and molecules when excited by an IR radiation. The IR spectrum shows what fraction of the IR beam is absorbed by the sample. The energy absorbed corresponds to the frequency of vibrational modes of the atoms and molecules in the sample.

A sample is IR active if there is a change of the electric dipole moment during their vibrational mode:

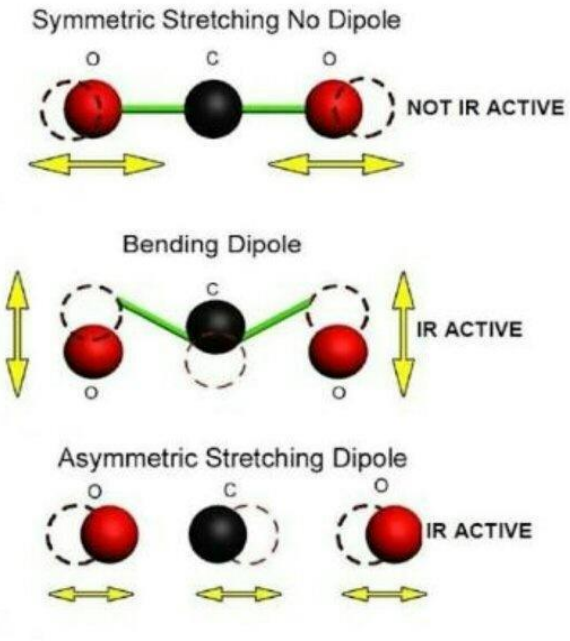

Figure 29 schematic representation of the IR active and IR inactive vibrational mode of CO_2 [127]

The most significant improvement in IR spectroscopy has come by the introduction of Fourier-transform infrared (FTIR) spectrometers. FTIR spectroscopy has radically improved IR analysis, enhancing the quality of the IR spectra and reducing the spectral acquisition time.

For FTIR in transmission geometry, the sample is placed directly into the IR beam, the transmitted energy is measured, and the spectrum is generated (Figure 30). The main disadvantage of this set-up is the sample preparation, the sample is required to be thin enough to allow the beam to pass through and must deposited or mixed with a IR transparent substrate. This is typically KBr, a material that is hygroscopic, further complicating the process.

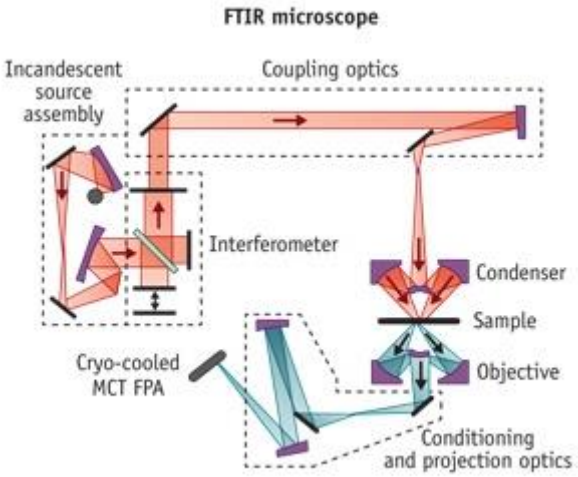

Figure 30 schematic of a transmission FTIR setup using broadband source to create the beam and a Michelson interferometer to generate the interferogram[128].

Attenuated total reflection Fourier transform infrared spectroscopy (ATR-FTIR) is a fast and simple characterisation technique to characterises solid or liquid samples without any further preparation[129]. The sample is deposited into an ATR crystal that is illuminated with a total internal reflection angle (Figure 31), therefore the beam is reflected several times into the crystals. The reflections of the beam that are in contact with the sample forms evanescent waves which penetrate several microns into the sample. The beam exits the crystal and the IR absorption of the sample is measured by a detector. It is important to highlight that the evanescent effect occurs only if the refractive index (RI) of the ATR crystal is higher than the material analysed. If not, the beam can pass into the sample and no detection occurs. Therefore germanium (RI ~4) should be used for carbonaceous materials compared with commonly used diamond crystals (RI 2.42)[130] which is similar to graphite.

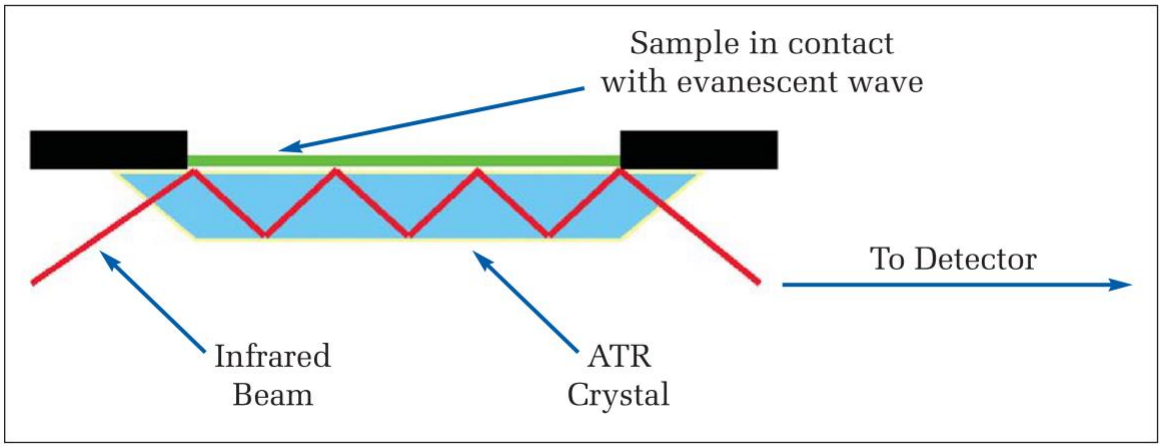

Figure 31 attenuated total reflection in a crystal [129]

4.1.5 Atomic Force Microscopy

Atomic force microscopy (AFM) is a powerful surface characterisation technique that measures the sample topology with extreme accuracy. Moreover, through a more sophisticated AFM it is possible to determinate many other material proprieties, such as friction, electrical forces, capacitance, magnetic forces, conductivity, viscoelasticity, surface potential and resistance.

The AFM consists of a sharp tip, less than <30 nm, attached to a cantilever that is used to scan the sample surface. By measuring the cantilever deflection, it is possible to map the sample surface at nanoscale resolutions. The small fluctuations of the cantilever are amplified and detected by a laser beam that is shone onto the cantilever and is then reflected into a photodetector (Figure 32).

The interaction between the tip and surface follow the Van der Walls potential. Therefore, the tip could be attracted to the surface or deflected from it. The force tip-surface is measured indirectly by knowing the stiffness and the deflection of the cantilever and applying Hooke's Law-

$$F = -kz$$

-where F is the force, k is the stiffness of the lever, and z is the bent height of the lever.

The cantilever is regulated via a Z feedback loop that adjusts the height of the tip. The feedback loop uses the laser deflection to monitor the force and tune the tip height.

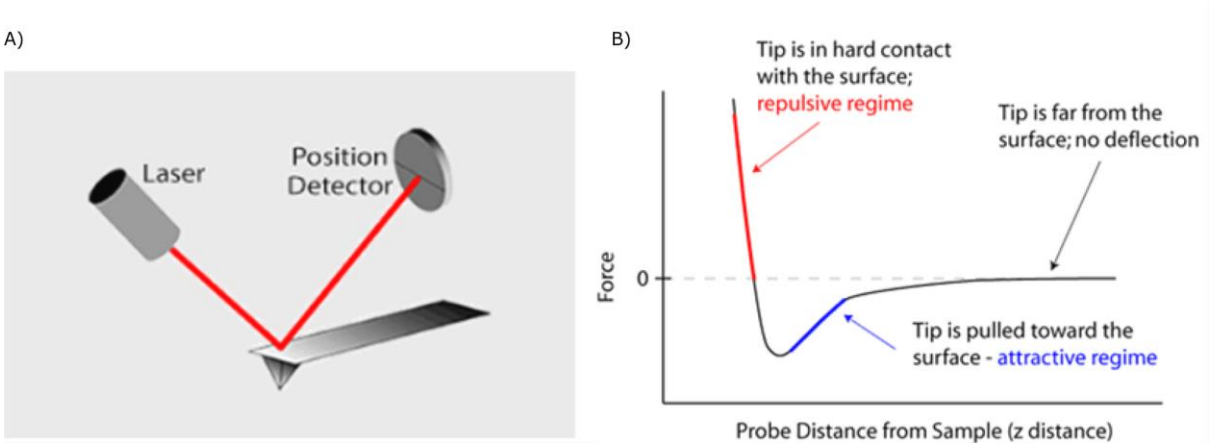

Figure 32 A) schematic of an AFM interaction. B) Tip sample is describe by the Wan der Val potential[131].

Based on the tip-surface interaction there are different AFM modes, such as contact mode or tapping mode. In contact mode AFM, the tip is always in contact with the sample, in repulsive regime (figure32). In tapping mode, the tip touches the sample surface only for a short time as the tip is maintained in continuous oscillation near its resonant frequency. This significantly improves the image resolution and the durability of the tip by avoiding the issue related to dragging the tip across the surface and limiting the lateral forces.

4.1.6 Atomic force microscope infrared spectroscopy

The Atomic force microscope infrared spectroscopy (AFM-IR) is a system that combines contact mode atomic force microscope (CM-AFM) and tuneable IR source. The AFM component of the instrument is initially used to generate a topology map of an area of interest, and subsequently by illumination by a tuneable coherent IR source it is possible to acquire local IR spectra or generate an IR map of the entire area at a particular wavenumber by simultaneously scanning for thermal expansion with the AFM cantilever.

Contact mode AFM-IR (CM-AFM-IR) uses a pulse tuneable IR laser to excite the molecular absorption in the sample. When IR active molecules absorbed the radiation, the molecules are excited and start to vibrate. Subsequently, the molecule returns to ground state transferring this energy as heat to the lattice, the provoking a local and rapid thermal expansion. The AFM tip can sense the "induced" thermal expansion and this leads to pulse exciting resonant oscillations that decay in a character ring-down signal. The ring-down motions are analysed via Fourier transform algorithms to determine the amplitude and the frequencies of the cantilever oscillations. A detector component records the cantilever deflection in the function of the IR laser wavelength producing local, down to 30 nm, IR amplitude spectra that are comparable to the standard FTIR spectra [113].

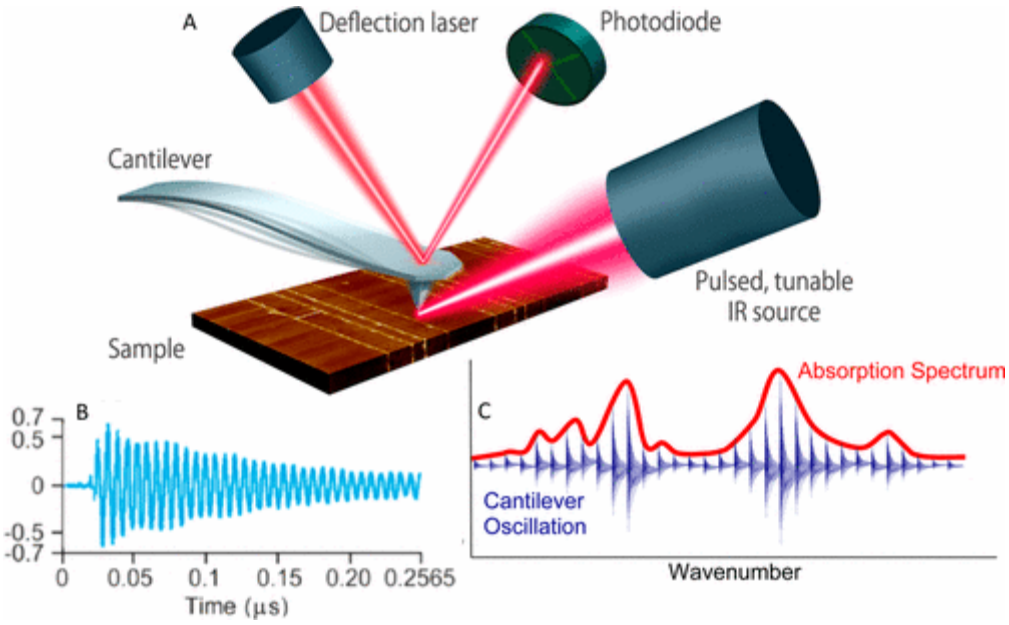

Figure 33 A) schematic diagram of AFM-IR represented the AFM cantilever and the IR beam focused onto the AFM tip. B) Ring-down oscillation of the AFM cantilever generate by the thermal expansion of the sample. C) IR amplitude spectra generate by measuring the cantilever oscillation as a function of the wavenumber correspond to the conventional FTIR spectra [105].

5 Experimental Methods

5.1 Materials

The material used in this project is a commercial graphene oxide dispersion (1% wt.). The table 1 summarise the information given by the supplier.

Table 1 data sheet of as-received GO dispersion used in the project [132]

	Graphene Oxide dispersion
Supplier	William Blythe GOgraphene
Appearance	orange-brown dispersion
Odour	Odourless
Concentration	1%, equivalent to 10 mg/mL
Flakes size distribution	variable
PH	>2
Elemental analysis	Oxygen : > 30 % Carbon: 60-70 % Nitrogen : < 1 % Sulfur : < 2 %
Trace Metals	< 0.1 %

5.2 Preparation of the Samples

Different GO samples have been prepared and analysed using variety of characterisation techniques: XPS, FTIR, Raman SEM, AFM and AFM-IR.

Different concentrations of GO dispersion have been produced, by adding aliquots of water to the raw material. Subsequently, the GO dispersion produced has been deposited via drop casting or spin coating to a specific substrate required by the analytical techniques.

XPS analysis requires the sample to be deposited in a bulk quantity onto a substrate. Therefore, a thick film of GO has been prepared via drop casting a GO dispersion with a concertation of 10 mg/ml on SiO_2 substrate (290 nm on Si).

The ATR-FTIR sample has been produced via freeze-drying the initial GO dispersion (10 mg/ml). Drop casting techniques have also been used to produce GO membranes with different thickness, by drop casted same aliquots (0.2ml) of GO dispersion at different concentration (5mg/ml and 1 mg/ml) and thicknesses measured with micrometre calipers.

Transmission-FTIR sample requires the sample to be deposited on an IR transparent substrate. The substrate used was a CaF_2 crystal (Crystrain Limited CaF_2 - Raman grade), that shows a bland IR absorption in the spectra region of interest (800-2000 cm^{-1}).

The GO Monolayer sample has been produced by spin coating a GO dispersion with a concentration of 0.1 mg/ml. The GO few layer sample (FLGO) was prepared via two-step spin coating procedure, consisting of depositing an aliquot of GO dispersion (0.1 mg/ml), spin coating and repeating the procedure once on the same substrate.

Raman sample has been prepared by spin coating a GO dispersion (0,1 mg/ml) onto SiO_2 substrate (290 nm on Si).

The AFM-IR samples were deposited to a gold substrate, thermal evaporated gold (ThAu) on Si and commercial strip-template Au (TsAu, Amsbio) has been used. ThAu was prepared by depositing a 5 nm Cr adhesion layer followed by 50 nm Au using a Moorfield evaporator. The thick film samples (form 1 μm to 0,5 μm) have been produced via drop casting a GO dispersion and subsequently depositing onto a ThAu substrate. The difference in the film thickness has been achieved by drop casting same aliquots (0.2 ml) of different concentrations of GO dispersion (from 1 mg/ml to 0,1 mg/ml) .

The thinner films have been prepared via spin coating techniques. Homogenous films of ∼60 nm and ∼10 nm has been produced by using a GO dispersion of 10 mg/ml and 2mg/ml respectively, where individual flakes samples have been prepared with a GO dispersion of 0.1mg/ml. The same methodology has been used to produce individual flakes sample onto template stripped gold (TSAu).

XPS analysis have been performed by self-assembled XPS, Axis Ultra spectrometer, Kratos analytical Limited, Manchester UK. The X-ray source is a monochromatic Al Kα (1486.7 eV). Raman spectra have been recorded on individual flakes using an InVia spectrometer (Renishaw) with a 514 nm laser at <1 mW power. Baseline correction and peak intensity measurements were carried out using WiRE 4.1 (Renishaw).

Bulk FTIR spectra have been obtained on vacuum dried GO films, using an ATR FTIR spectrometer (Nicolet iS50 spectrometer, Thermo Scientific) with a germanium crystal, for each spectra (700-4000 cm^{-1}) 64 co-averages has been collected, with a resolution of 4 cm^{-1}.

FTIR spectroscopy in transmission geometry has been performed by using VERTEX 80, Bruker FT-IR spectrometer and HYPERION Microscope, using an MCT (mercury cadmium telluride) liquid-N2-cooled detector at a resolution of 4 cm^{-1} and 512 Co-averages for spectra. SEM images has been acquired with a Zeiss Ultra Plus microscope with an InLens Detector and 5 keV gun voltage.

The AFM measurement have been performed by using a Multimode 8, Bruker AFM, in tapping mode, with Bruker tip (TESPA-V22).

AFM-IR measurement have been performed on NANO NanoIR2 system (Anasys Instruments) operating with top-down illumination, and a tuneable infrared laser (optical parametric oscillator, 10 ns pulses at a repetition rate of 1 kHz, approximate beam spot size 30 µm) as an IR source. For the present study, IR amplitude spectra (850 cm^{-1} to 2000 cm^{-1}, Co-average 1024) and The IR amplitude images (128 co-average, 256x256 resolution) has been acquired using a gold-coated silicon nitride probe (0.07–0.4 N/m spring constant, 13 ± 4 kHz resonant frequency, Anasys). The power was reduced to <1% to avoid sample damage.

6 Results and Discussion

6.1 Conventional Characterisation

A comprehensive characterisation of the commercial graphene oxide by 'GOgraphene' was achieved through optical microscopy, SEM, AFM, XPS, Raman and FTIR spectroscopy.

A GO sample was prepared by spin coating SiO_2 with a GO dispersion (0.1 mg/ml) and analysed via optical microscope and SEM. The optical microscope images (Figure 34) highlight the monolayer nature of the GO dispersion, in addition displaying few impurities and regions characterised by an agglomeration of flakes. These regions were probably generated by an overlap of several flakes during the spin coating process, instead of a partial exfoliation of the graphite residues.

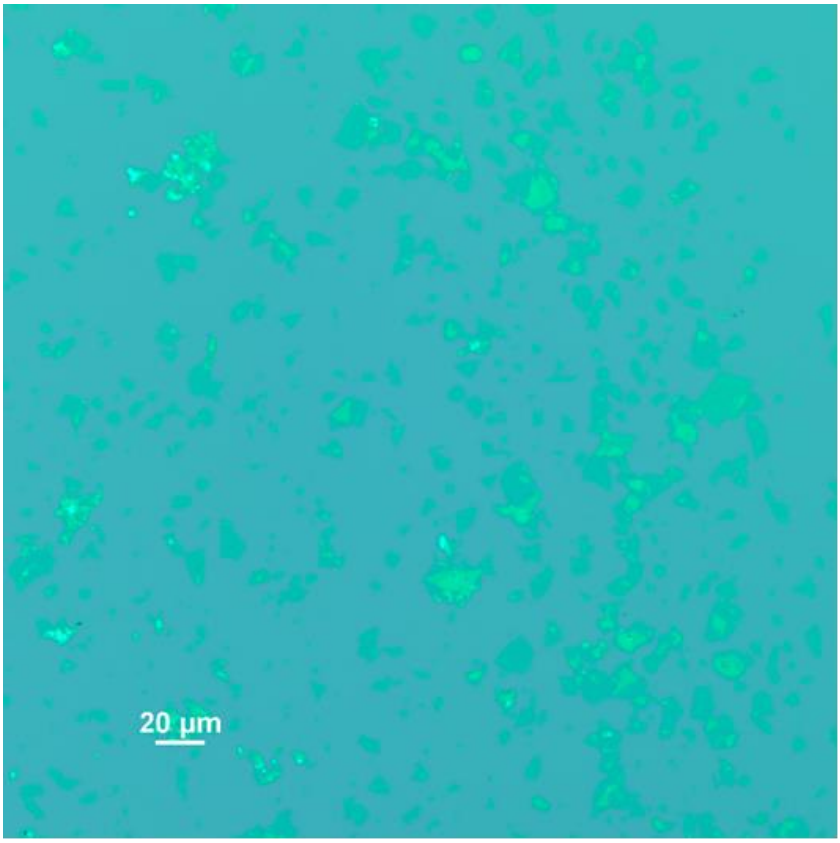

Figure 34 Optical image of GO flakes on SiO_2, the image highlights the monolayer flakes (light green) nature of the GO dispersion.

Low magnification SEM images (Figure 35) of the same sample confirm the predominance of monolayer over the whole images. The SEM images also display the impurities found in the

optical microscope results (Figure 35),which have been attributed mainly to surface contamination and to small metallic residues and un-oxidised graphite[132].

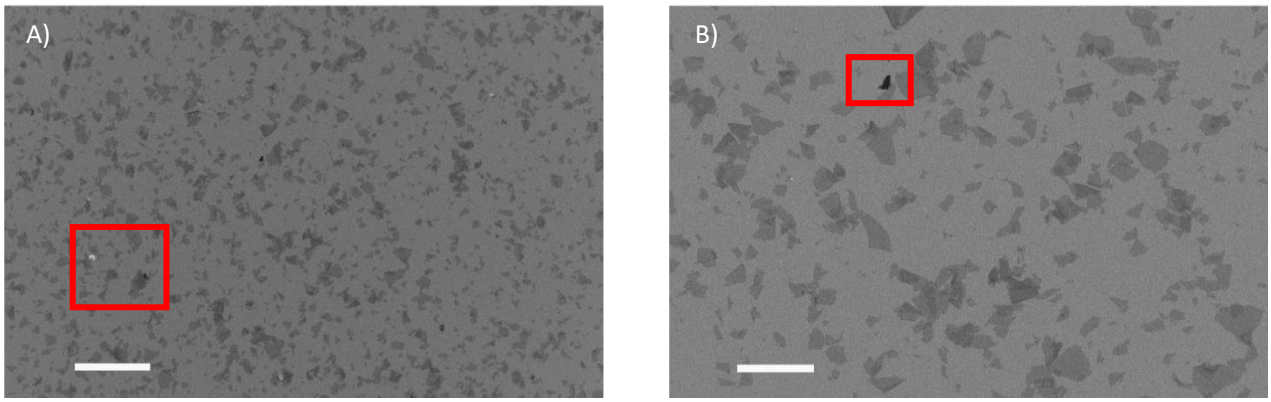

Figure 35 SEM images of GO flakes on gold substrate. A) Low magnification SEM image GO flakes (50 µm scale) **B)** high magnification SEM image of GO flakes (20 µm scale). Insets in both images highlight observed impurities.

The flake size distribution was measured by high magnification SEM imaging (Figures 35, 36), measuring the lateral size of 200 flakes. The average flake size has been found to be 3.65 µm with a standard deviation of 2.14 µm showing a significant difference between the flakes sizes but typical for graphene oxide[133].

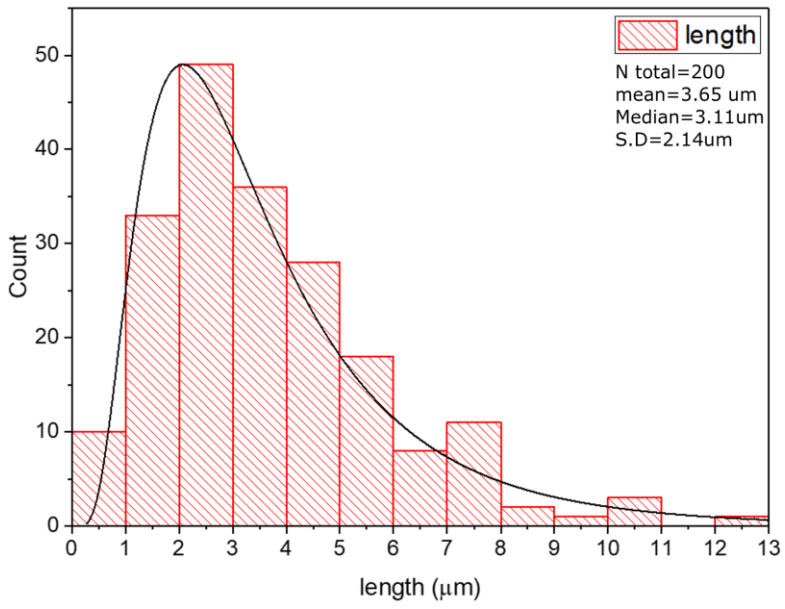

Figure 36 Histogram representing the GO flake size distribution, measured of 200 flakes, with lognormal fitting curve.

The AFM analysis results (Figure 37) are in agreement with the SEM and optical microscope images and analysis, therefore confirming the single layer nature of the GO dispersion. The AFM images show the distinctive profile height of the monolayer GO, approximately 1 nm[134].

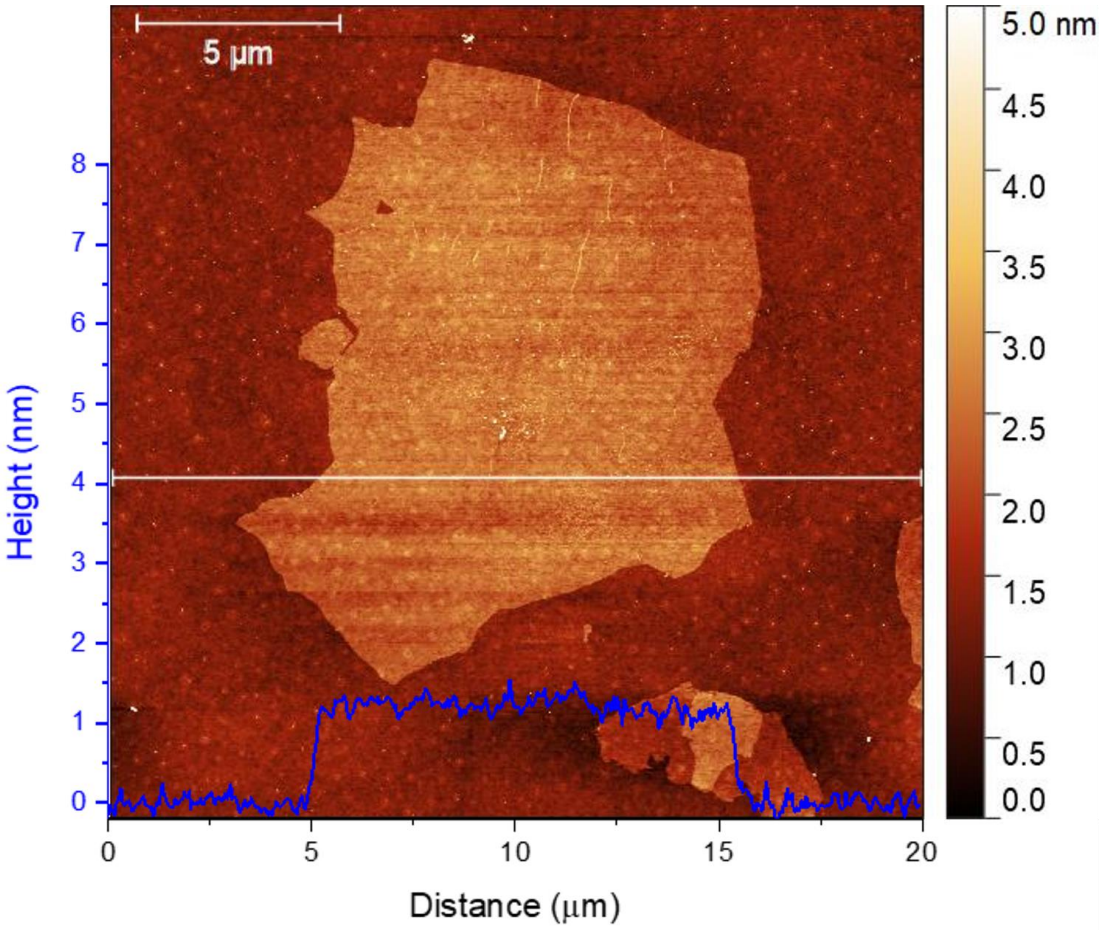

Figure 37 Tapping mode AFM topology of monolayer GO flakes. In blue the flake profile shows the characteristics monolayer GO height, approximately 1nm.

Additional chemical information can be gained by Raman analysis of GO flakes. The averaged spectra (Figure 38) shows the presence of the characteristic GO peaks, the D peak (1347 cm^{-1}) and G peak (1593 cm^{-1}). The ID/IG ratio has been found to be 0.9 by taking the ratio of these two. The broad D peak is associated with the out of plane vibrations related to the sp3 defects in GO, confirms the presence of a highly defective basal plane in the GO flakes. The G peak is associated with the in-plane vibrations of the sp2 carbon bond. The ID/IG ratio is a typical metric to quantify the level of defectiveness of graphene materials and is similar to those found in previous works[135]. The 2D band (~2700 cm^{-1}) shows the typical broad peak shape found in the literature and gives little information for graphene oxide materials[136].

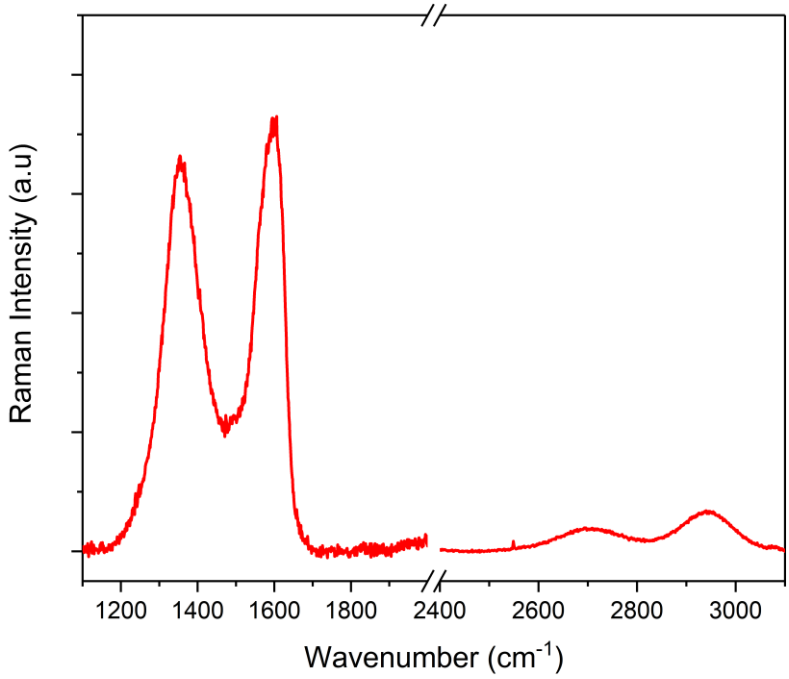

Figure 38 Averaged Raman spectra of Graphene Oxide

The chemical composition of GO has been quantified using XPS analysis. The C:O ratio has been measured by integrating the C 1s and O 1s peaks, at 284 and 530 eV respectively, in the survey XPS spectra (Figure 39). By dividing the C 1s areas by the O 1s areas, the C:O ratio was found to be 7:3, showing in a highly oxidised graphene. It can also be seen in the survey spectrum that there is little other contamination within the sample.

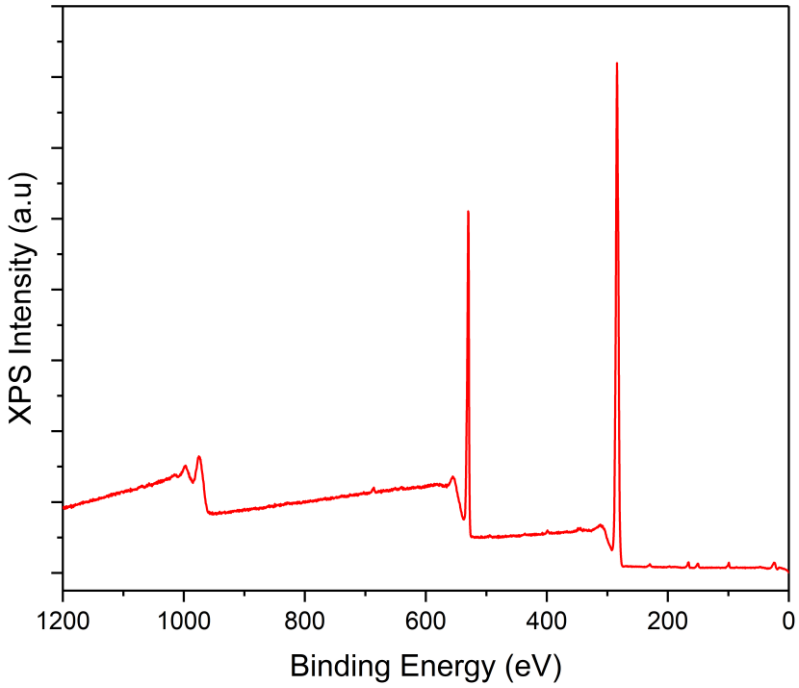

Figure 39 Survey XPS spectra, showing the oxygen O1s (530 eV) and C1s (284 eV) peaks.

The quantification of the carbon-oxygen species has been achieved by the deconvolution of the C1s peaks in the high resolution spectra (Figure 40)[80,98,136].

As expected from the Raman spectrum, the most representative oxygen species is the C-C and C-H groups (286.6 eV), making up 44.63% of the total carbon species. This correlates with the high intensity of the D band seen in Figure 38. Hydroxyl (C-OH 288.0), carbonyl (C=O, 289.0 eV) and ether groups (C=O, 287.9 eV) follow with 11.69%, 8.34% and 5.56% respectively. Moreover, XPS analysis also gives information regarding the sp^2 carbon (C=C) in the aromatic rings (284.5 eV) that represents 29.78% of the total C 1s peak area. Finally, less than 1 % of the area has been attributed to C-C satellites and cannot be determined with the peak fit employed in this analysis.

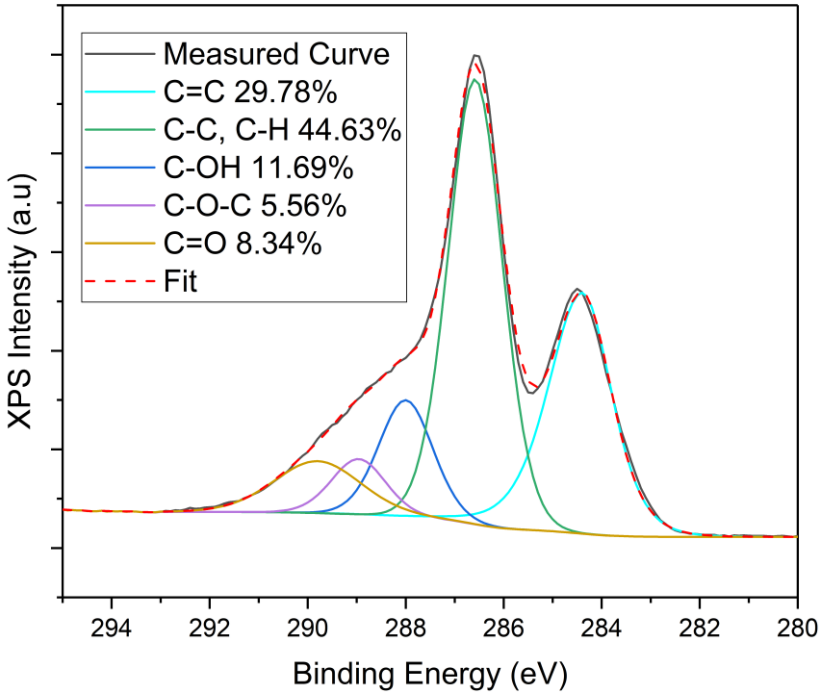

Figure 40 deconvolution of the C1s peaks in the high resolution XPS spectra

6.2 FTIR Characterisation

Bulk ATR-FTIR (Bulk-IR) analysis was also employed to investigate the chemical composition of the GO dispersion. A GO freeze dried sample was analysed on an ATR FTIR spectrometer using a germanium crystal.

The GO bulk-IR spectra (Figure 41) is in agreement with literature previously discussed[103], showing the three IR absorbance peaks characteristic of bulk GO. Based on Acik's work[103], an interpretation of the peaks has been given (Figure 41) and the reader is directed to this work for further discussion and reading.

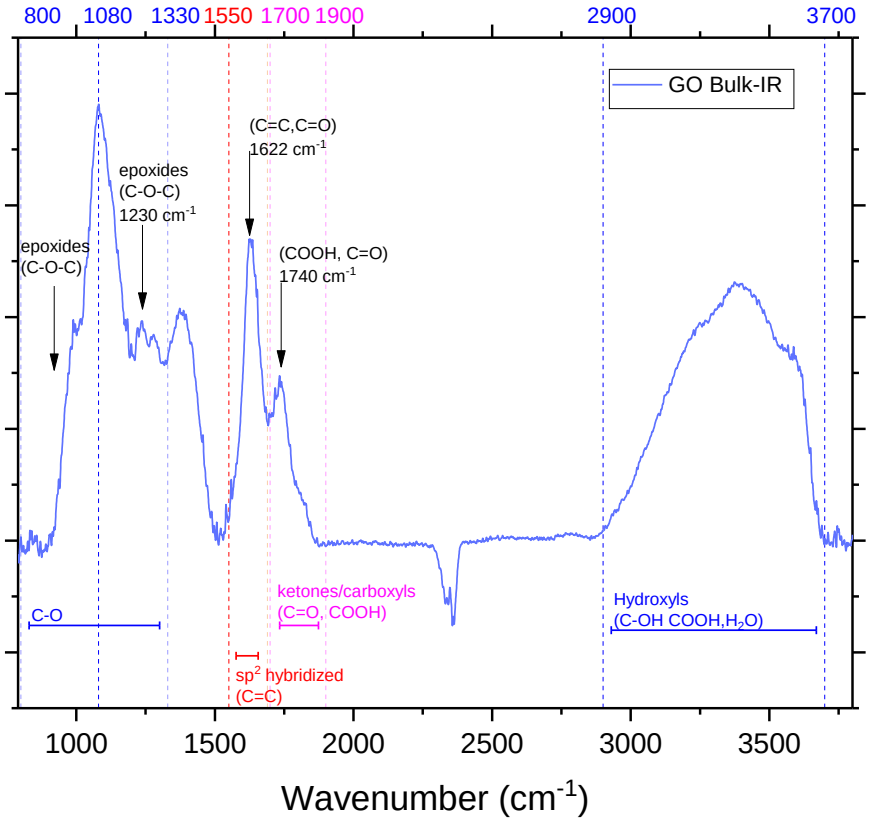

Figure 41 ATR-FTIR spectra of freeze drying Graphene oxide acquired with a germanium crystal

The intense peak at 3000 cm^{-1} to 3700 cm^{-1} can be attributed to hydroxyl groups and intercalated H_2O between the GO flakes, with secondary contributions of carboxyls and five member-ring lactols groups, ~3550 cm^{-1}, ~3619 cm^{-1} respectively.

The IR peak between 1500 cm^{-1} to 1850 cm^{-1} is the complex result of the overlapping between the asymmetric stretch of sp^2 C=C in the aromatic rings (1500-1600 cm^{-1}), C-OH vibrational

modes of carboxyl group (COOH, 1600-1750 cm^{-1}) and carbonyl groups from the ketones (1600 -1850 cm^{-1}). In addition, there are further contributions of the H_2O scissor mode trapped between the layer and/or physiosorbed on the GO membranes (1600-1750 cm^{-1}).

The finger print region (800-1500 cm^{-1}) is an intricate overlap of IR absorption signals that results in a large broad peak. The region within 900 cm^{-1} and 1100 cm^{-1} is dominated by the IR vibrational mode of ethers and weak contributions of hydroxyl and carboxyl groups. The absorption between 1100 cm^{-1} and 1280 cm^{-1} can be assigned to the weak absorption of ketones, peroxides (1267 cm^{-1} and 1185 cm^{-1}) and pyrans (1103 cm^{-1}). The region between 1280 cm^{-1} to 1500 cm^{-1} is dominated by the vibrational modes of epoxides (1280-1320 cm^{-1}), ketones and 1,3-benzoquinones (1453 cm^{-1}-1523 cm^{-1}). Moreover, epoxides have a weak vibrational mode between 1070 cm^{-1} and 1170 cm^{-1} with an additional contribution at 850 cm^{-1}.

The bulk IR analyses is in good agreement with the previous XPS analysis however due to the complexity and the huge amount of chemical information gained by GO Bulk-IR spectra, it has not been possible to quantify the chemical species. This is mainly due to the complexity of the vibrational modes which overlap within each other and the substantial shifts in frequency relating to the proximity and conjugation effects as reported by Acik, M. *et al.*[103].

Thinner GO membranes (Figure 42) were produced in order to investigate the thickness dependence of the GO IR absorbance spectra [103]. At the critical thickness of ~1µm, detected using a micrometre, the bulk-IR was not able to detect the anything from sample, showing the limit of detection of the ATR-IR technique. Therefore, to characterise thin GO membranes a Micro FTIR (T-IR) was employed in transmission geometry.

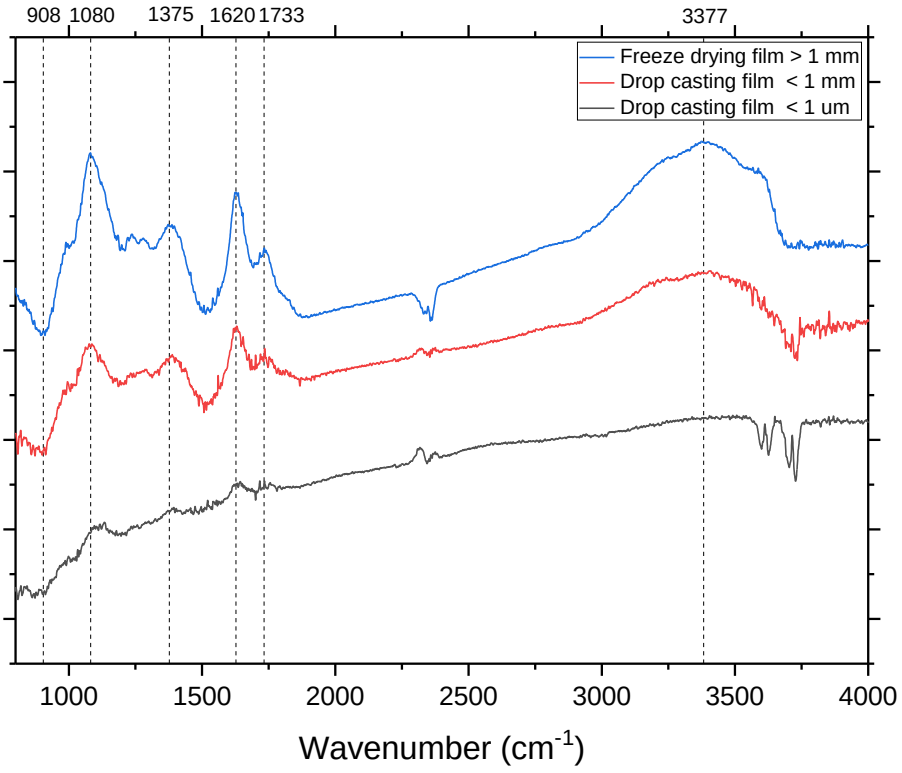

Figure 42 investigation of limit of detection ATR FTIR

Monolayer GO and Few Layer GO (FLGO) samples have been prepared by spin coating a GO dispersion (0.1 mg/ml) on calcium fluoride (CaF_2). Due to the CaF_2 roughness, it has not been possible detect the exact thickness of the samples via AFM so SEM was employed to confirm the distribution of single flakes for the monolayer GO sample.

The GO T-IR spectra (figure 43) displays a low IR absorption due to the extremely small thickness of the sample compared to strong absorption generated by the CaF_2 substrate. However, CaF_2 absorption could easily be subtracted from the spectra revealing the three characteristic peaks of GO IR absorption spectrum.

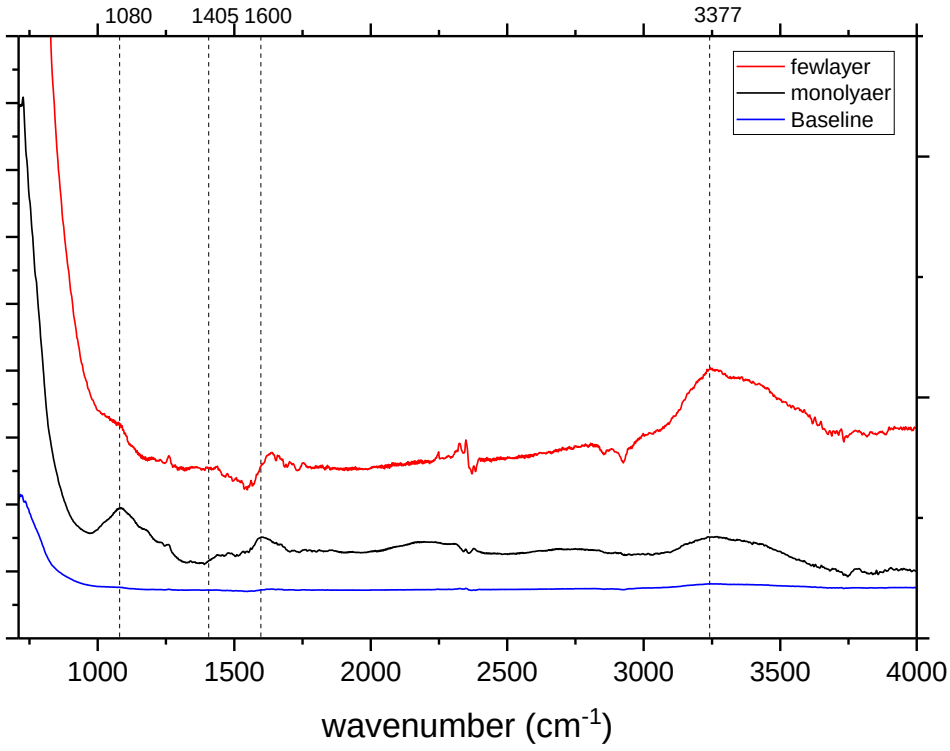

Figure 43 a) T-FTIR spectra in transmission setup: in red the spectra of few layer GO, in black monolayer GO spectra and in blue of CaF2 IR absorption spectra

Figure 44 compares the GO Bulk-IR and T-IR spectra in the region between 800 to 2000 cm^{-1}. A significantly different spectrum has been recorded between GO B ATR-IR and monolayer GO T-IR whereas, similar spectrum of GO Bulk-IR was observed in the FLGO T-IR. Showing that at the thickness of FLGO the two IR techniques are equivalent and proving the reliability of both techniques.

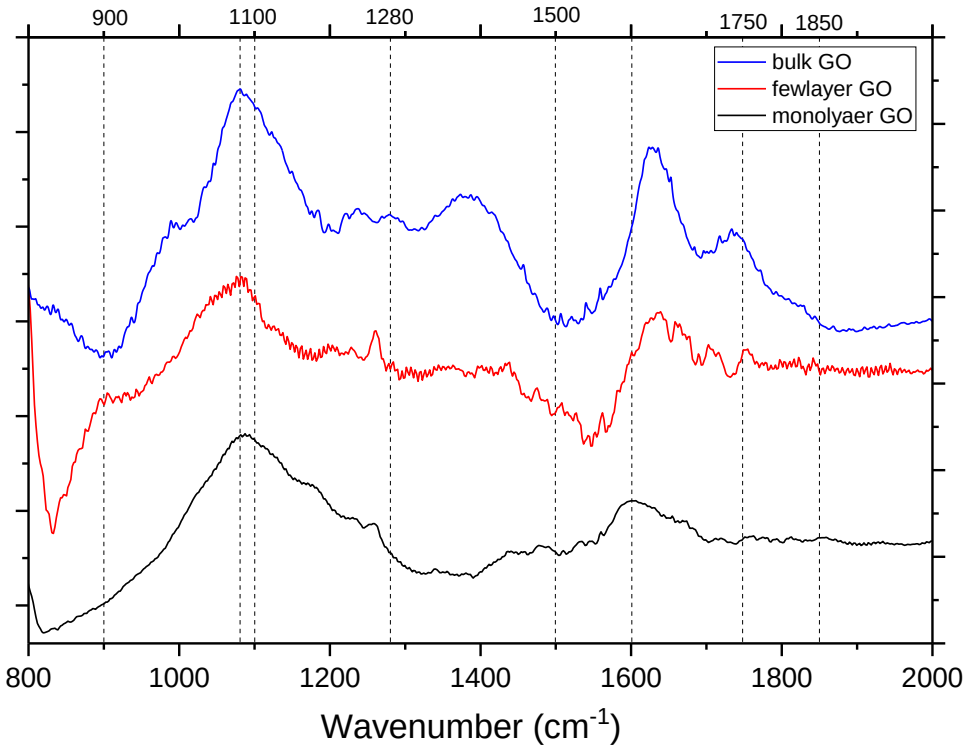

Figure 44 the image summrise the FTIR GO spectra, in Blue the GO bulk spectra, few layer GO and in black monolayer GO

GO Bulk-IR and FLGO T-IR spectra shows a broad peak that covered the entire finger print region (900-1500 cm^{-1}), peaking at 1080 cm^{-1}. In contrast, the monolayer T-IR spectrum shows a narrow peak from 900-1280 cm^{-1} resulting in a loss of the typical shoulder at 1000 cm^{-1}. Furthermore, the spectrum completely lacks the IR signal from 1280 cm^{-1} to 1400 cm^{-1}, with a just minor peak at 1400-1500 cm^{-1}.

In the region 1500-1850 cm^{-1} of the spectra, the Bulk-IR shows an intense peak at 1630 cm^{-1} followed by a secondary peak at 1750 cm^{-1}. In contrast FLGO T-IR spectrum shows only a low absorption peak at 1630 cm^{-1}, whereas in the monolayer spectrum the peak is significantly shifted from 1630 cm^{-1} to 1600 cm^{-1}.

The radical changes in the IR spectra in different samples, could be the result of several factors including:

The detection limit of the T-IR which is not able to measure the chemical species less represented in the sample. Another factor could be related to the different amount of H_2O trapped within the flakes and/or physiosorbed onto the sample surface that could lead to a significant broadening of the peaks[103]. In addition in monolayer GO sample and thicker samples subsist a change in the proximity and conjugation of the oxygen species[103]. Moreover, due to the lack of the spatial resolution it is not possible exclude the possibility of an inhomogeneity of the sample in the monolayer sample that can potentially lead to locally different T-IR spectra although this is unlikely as the spot size for these measurements is in the order of microns, therefore analysing the whole flake, as determined by the previously discussed flake size analysis.

6.3 AFM-IR Thickness Dependence and Comparison with Conventional FTIR

To investigate whether the local structure of GO flakes and thin films (<1 µm) can be measured with high spatial resolution, AFM-IR was employed. Initial studies were carried out to correlate conventional FTIR spectra (IR absorbance spectra) and AFM-IR spectra (IR amplitude spectra). In order to do so, six samples of GO with varying thicknesses (from 1.5 µm to 1 nm) were prepared.

Three thicker GO samples (from 1.5 µm to 0.3 µm) were prepared (see Experimental Methods) and characterised with the AFM-IR, where the sample thickness was measured via contact mode AFM. For each sample, 10 spectra were acquired and averaged.

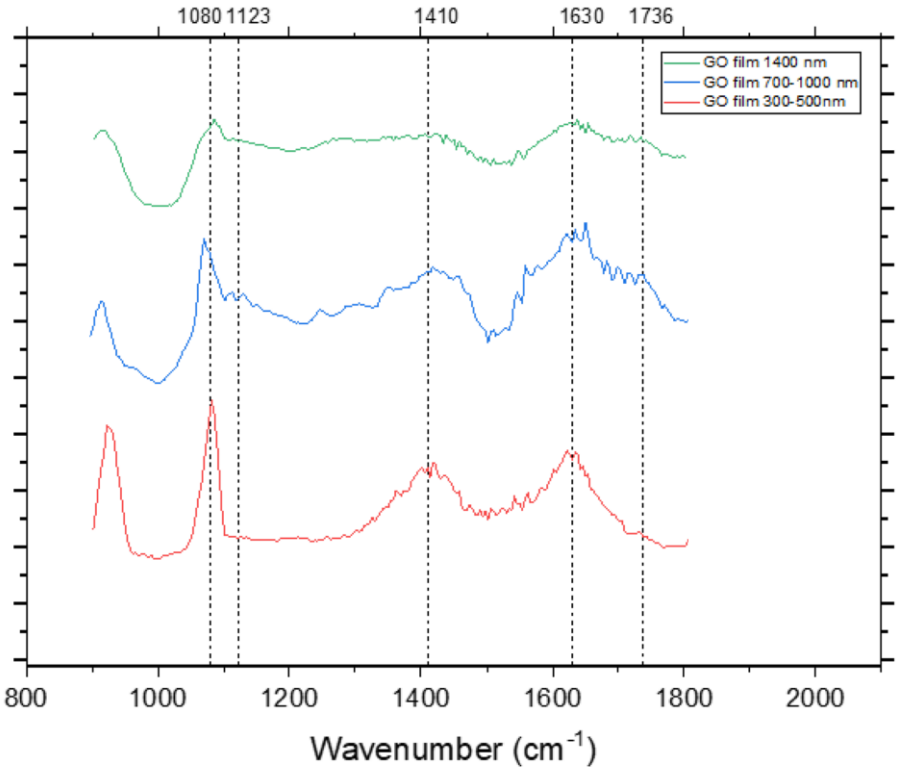

Figure 45 AFM-IR spectra of thick GO films: in green the averaged spectra acquired on a GO membranes of ~ 1.4 µm thick, in blue ~1 µm and in red ~500 nm thick.

It can be clearly seen in Figure 45 that the averaged IR amplitude spectra are significantly different from each other. The thickest sample, ~1400 nm , represented in green in the figure 45 shows a continuum of absorption all over the spectrum[105]. In terms of peak ratio and shape, the IR amplitude spectra of the sample with a thickness of ~1 µm is comparable to the

spectra acquired with the Bulk-IR, with the only difference relating to the low absorption in the region between 900 cm^{-1} and 1000 cm^{-1}.

The IR amplitude spectrum of the sample with the thickness of ~ 0.4 µm (GO 4-IRA) shows a drastically different spectra compared to the bulk ATR-IR. Within the bulk ATR-IR spectra a broad peak is always seen (finger print region 900-1500 cm^{-1}) instead, GO 4-IRA displays only two sharp bands; which are narrow and intense at 920 cm^{-1} and 1080 cm^{-1} with the suppression of the signals between 930 -1000 cm^{-1} and 1130 cm^{-1} - 1400 cm^{-1}.

Continuing with the characterisation of the thinner GO materials using the AFM-IR and the interpretation of GO in FTIR[103], a sample of ~60 nm was prepared and 100 spectra were acquired. In order to exclude the possibility of a reduction of the GO by the IR beam, the laser power was kept below 1% and 50 spectra were acquired on a sample and measurements were repeated twice on the exact same points (Figure46). The two batches of 50 spectra were averaged and both averages show identical results, therefore no reduction occurs at <1% laser power.

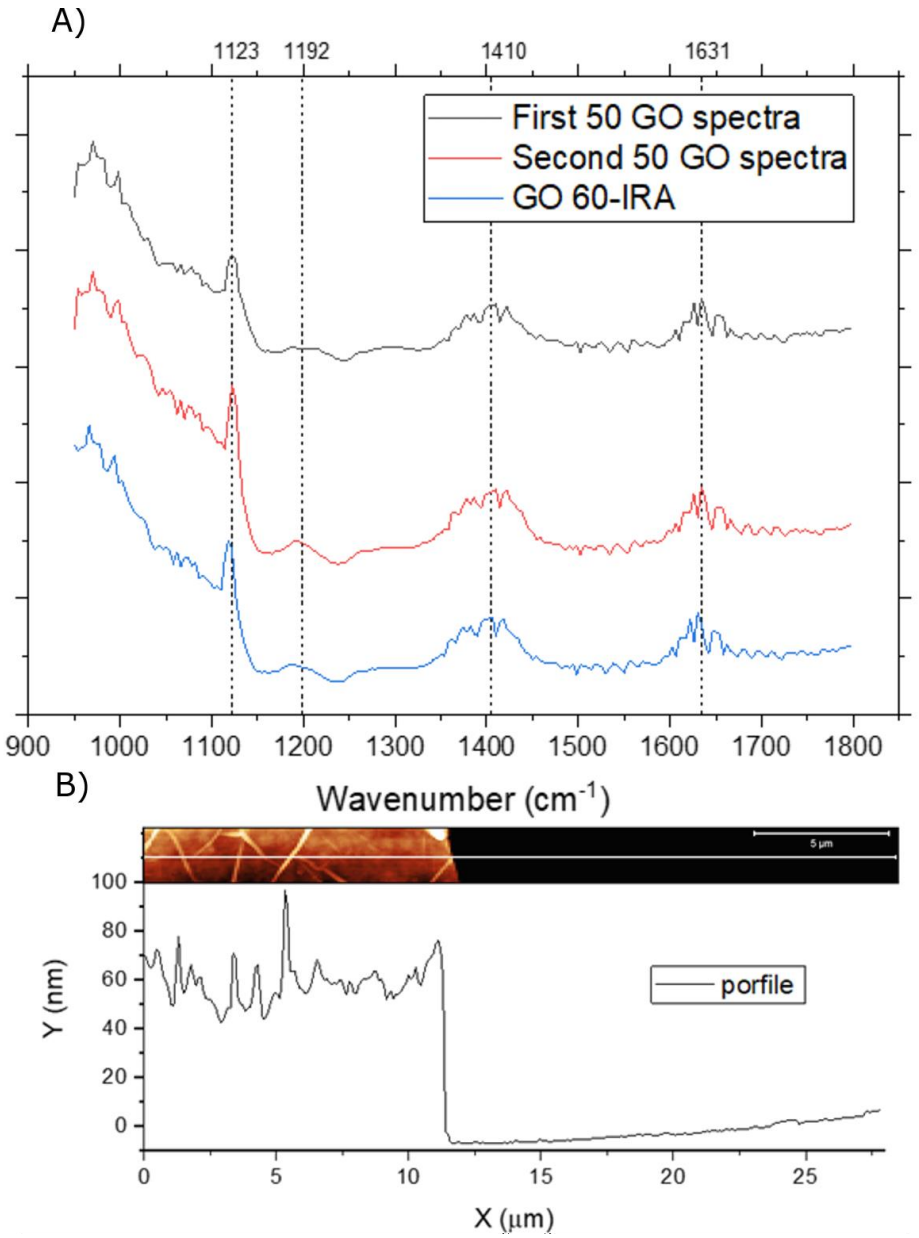

Figure 46A) AFM-IR spectra of GO sample with a thickness 60 nm. In black the average of the first 50 GO spectra, and in red the second batch of 50 spectra, in Blue the average of 100 spectra (GO 60-IRA).**B) AFM topology reveals the sample thickness of 60 nm.**

The average of 100 IR amplitude spectra acquired on 60 nm (GO 60-IRA) was expected to be consistent with the GO Bulk spectra acquired with the conventional FTIR (GO Bulk-IR and FLGO T-IR) however, the spectra recorded is significantly different from the Bulk IR spectra. Based on Acik's result, an interpretation of the spectrum has been proposed. The IR amplitude spectra shows a strong broad peak from 950 cm^{-1} to 1140 cm^{-1}, with the maximum at 970 cm^{-1}. The maximum is shifted by more than 100 cm^{-1} compared to GO B ATR-IR and FLGO T-IR. The strong absorption in this region (950 cm^{-1} to 1140 cm^{-1}) indicates that AFM-IR is able to detect well the chemical species vibrating in that region, such as peroxides, furans and

dioxolanes, with a weak contribution of hydroxyl and caboxyl groups as seen in the bulk ATR-IR spectra. The band at 1125 cm^{-1} could be related to the combination of the vibrational modes of pyrones, 5-membered-ring lactols and weak absorption of acid anhydrides[137].

The suppression of the IR signal in the region 1150-1331 cm^{-1} could suggest that the weak absorption of ketones that dominate the region (1100-1280 cm^{-1}) are not sensed by the AFM tip. The peak with a maximum at 1400 cm^{-1} could be generated by the strong ketones and 1,3-benzoquinones absorption with a contribution of epoxides.

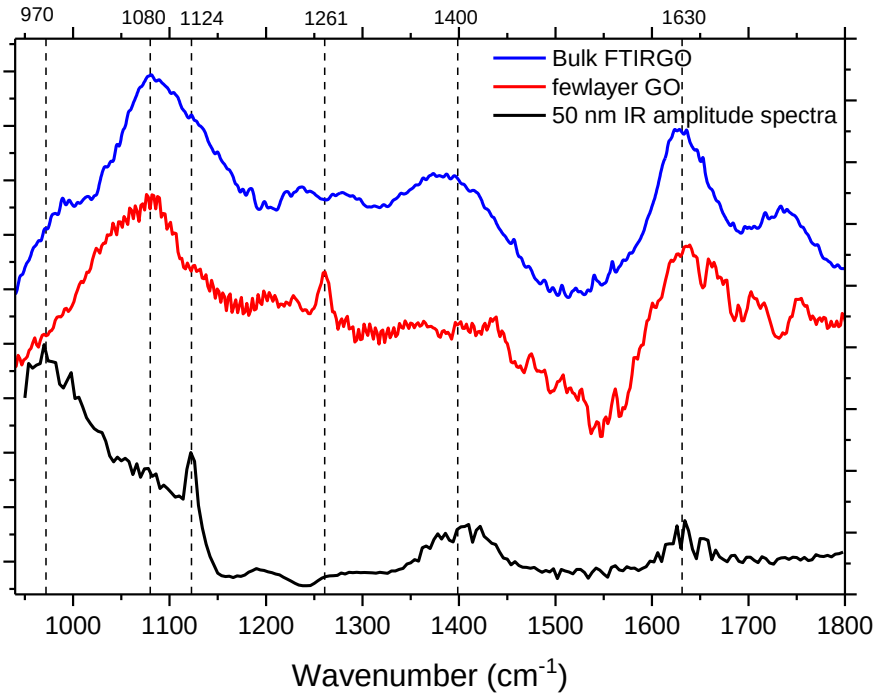

Figure 47 spectra comparison between conventional FTIR (GO Bulk IR and GO T-IR) and spectra acquired with AFM-IR (GO 60-IRA spectra).

The peak at 1630 cm^{-1} is similar in shape to the FLGO T-IR spectrum. This indicates that the AFM-IR has been able to detect the thermal expansion related to the vibrational mode of carboxyl groups (1600-1750 cm^{-1}) and carbonyl group of the ketones (1600 -1850 cm^{-1}), with additional contributions of H_2O scissor mode of the water. It is important to note the complete absence of the IR amplitude signal related to the C=C in plane vibrational mode (1500-1600 cm^{-1}) which could either be due to a lack of sensitivity to this weak vibration, due to a lack of a dipole, or the fact that the in plane vibration will not induce a vibration perpendicular to the material, thereby inducing a detectable tip oscillation.

The IR amplitude spectra is in good agreement with the literature [118] and a similar interpretation of the IR amplitude spectra multi-layer graphene has been achieved by Liu *et al*. [118]. The strong IR signal from 900 to 1100 cm^{-1}, peaked at 1025 cm^{-1}, can be attributed to C-O vibrational mode of epoxy resembling configuration. The peak between 1300-1450 cm^{-1} has been assigned to the hydroxyl attached to aromatic carbon or to the hydroxyl in carboxyl configuration. The peak at 1600 cm^{-1} is assigned to the aromatic bond stretching of the carbon plane. In addition, Liu *et al*. the peak at 1720 cm^{-1} has been attributed to the C=O carbonyl vibrational mode [118].

6.4 Thin Film and Monolayer GO AFM-IR Analysis

Focusing on the characterisation of thinner GO materials with the AFM-IR, a ~10 nm sample has been prepared via drop casting a GO dispersion of 2 mg/ml onto a gold substrate and 70 IR amplitude spectra (GO 10-IRA) were acquired and averaged (Figure 49).

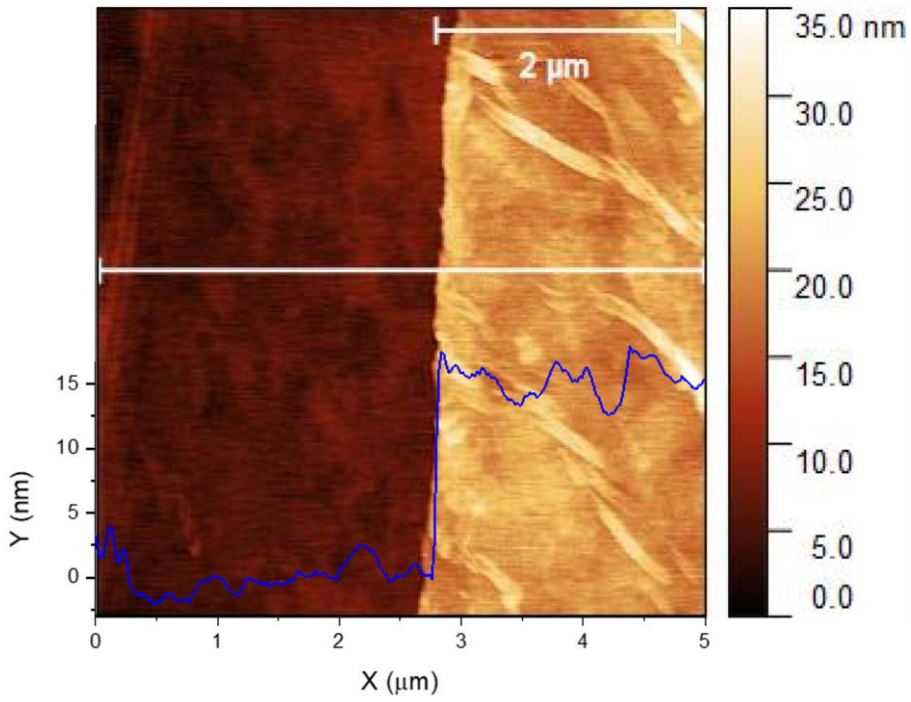

Figure 48 CM-AFM topology was used to measure the thickness of the sample, ~10 nm.

The averaged IR amplitude spectrum (GO 10-IRA) (Figure 49) display a strong and narrow peak at 1080 cm^{-1}, assigned mainly to the vibrational mode of ether functionality previously discussed. The small absorption at 1220 cm^{-1} can be attributed to the weak absorption of

ketones, peroxides and pyrans, whereas the small peak at 1620 cm^{-1} is due to the C-OH vibrational modes of the carboxyl group and the carbonyl group of the ketones (1600 -1850 cm^{-1})[103]. The spectra (GO 10-IRA) differs from the GO 60-IRA and other works, mainly by the narrower peak at 1080 cm^{-1}, the absence of peak at 1400 cm^{-1} and significant decrease in intensity and shift of peak from 1630 cm^{-1} to 1600 cm^{-1}. This could be due to the removal of coordinated oxygen moieties that has been seen to effect the spectra in previous sections and other works[103].

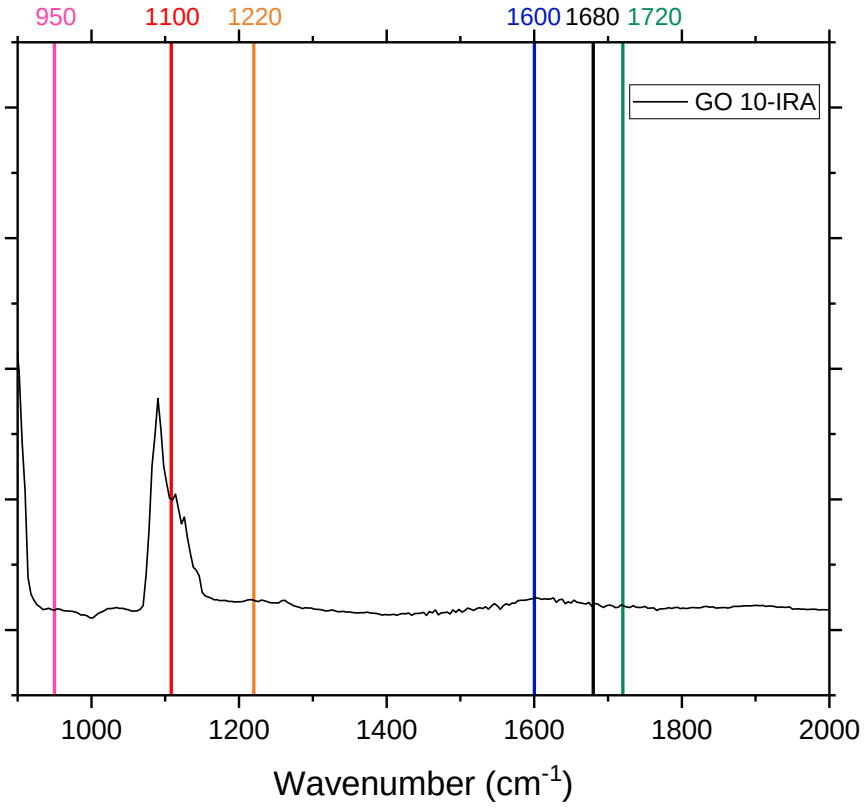

Figure 49 IR amplitude spectra of GO 10-IRA acquired with AFM-IR

A further capability of AFM-IR, in addition to spectral acquisition, is the ability to perform IR response maps at a fixed wavelength. This allows for the spatial determination of functional groups for a given thermal response[101]. Four IR amplitude maps at different wavelengths

(Figure 50) were acquired in exactly same position in order to investigate the possible local differences in the chemical composition of the 10 nm sample in Figure 48.

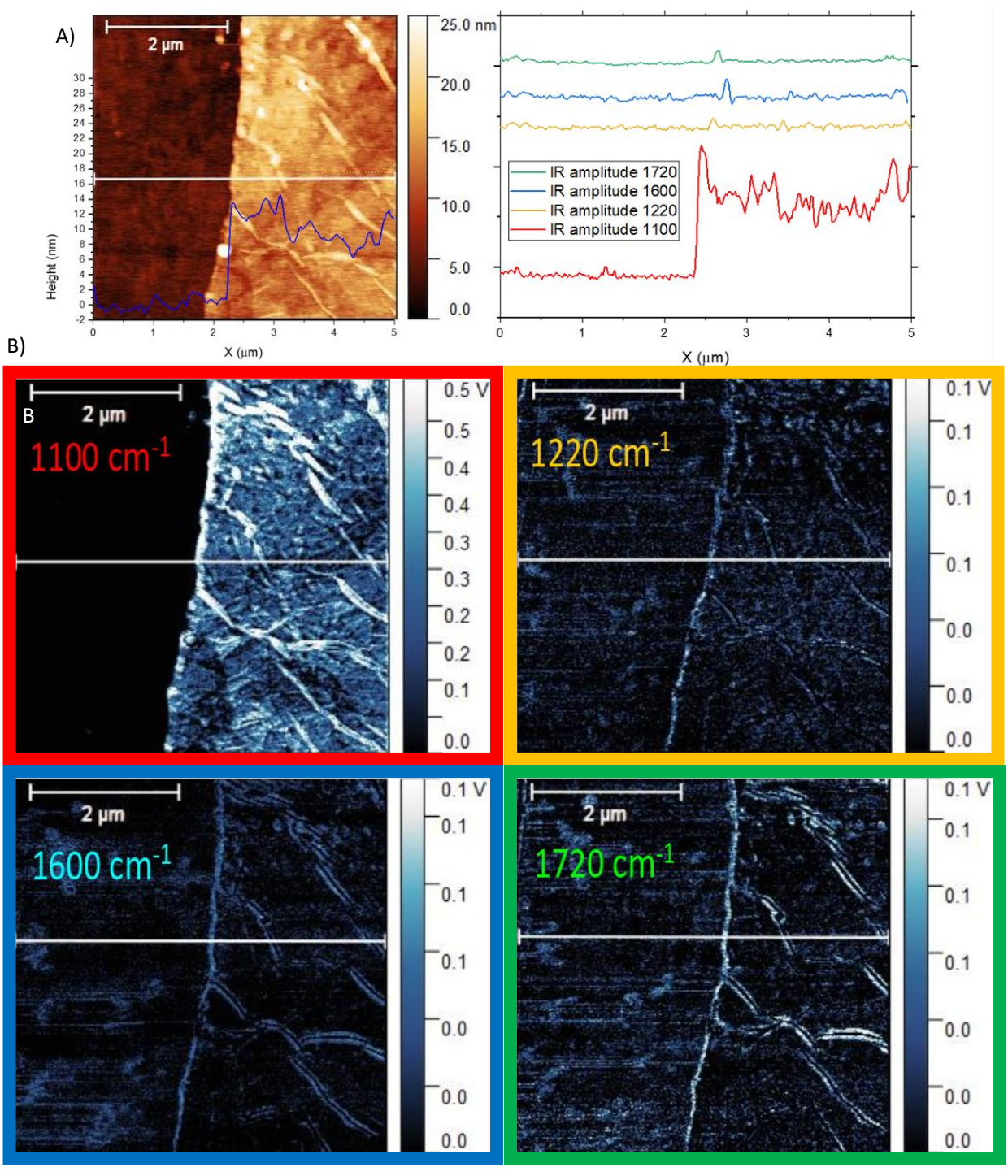

Figure 50 CM AFM confirmed the thickness, ~ 10 nm(A), GO sample and four IR amplitude maps were acquired at the wavenumbers indicated on each map. The corresponding profiles (top right) for each map and corresponding colour are shown.

The IR amplitude map at 1100 cm^{-1} (principally relate to the C-O vibrational mode) shows a strong IR amplitude signals that agree well with the strong peak displayed by the GO 10-IRA spectra. No significant thermal expansion occurred at the maps recorded at 1220 cm^{-1} (related to the absorption of ketones, peroxides and pyrans) also at 1600 cm^{-1} and 1720 cm^{-1} (carboxyl group and carbonyl group of the ketones). However, a strong IR amplitude signal has been detected near the wrinkles and edges for all the IR amplitude maps recorded. To prove that these signals are not artefacts created by the AFM-IR, mapping was acquired at 950 cm^{-1}, which is a wavenumber where no thermal expansion should occur agreeing with GO 10-IRA spectra and conventional FTIR. The IR amplitude map at 950 cm^{-1} shows a blank image, where only the noise has been detected and therefore proving the reliability of the AFM-IR map and that the increase in signal is real at responsive wavelengths.

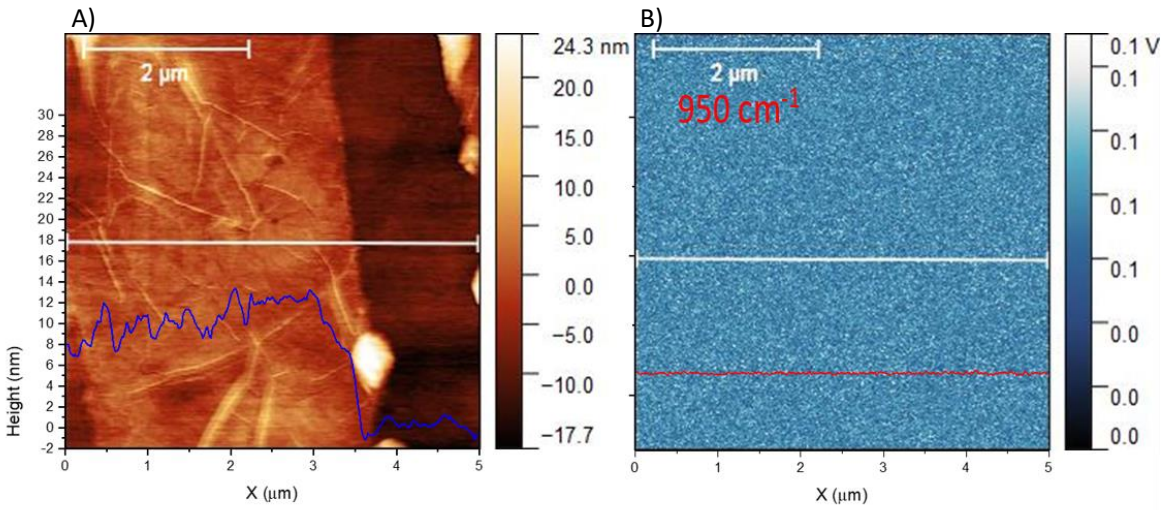

Figure 51 topology map (A) and IR amplitude (B) maps acquired at 950 cm^{-1}

Liu *et al*. [118] suggest that the different signal intensity recorded on the edge and on the wrinkles could be related to a different composition of the chemical species. This proposed theory would suggest that the samples would show a higher concentration of all the oxygen species only near the wrinkles and edges compared to the other regions of the sample. Within the sample maps in Figure 50, the edges have been created manually by scratching the sample surface therefore it is unlikely that these increasing of the signal on the edges is related to different chemical composition. A possible explanation of these enhancements has been attributed to the peculiar topology of the wrinkles and edge itself orientating the graphene plane into that of the tip, increasing the sensitivity of the instrument to in plane vibrations

which has implications for further work and possible enhancement of the technique. Finally, a monolayer sample (1 nm thick) was prepared by spin coating a GO dispersion (0.1 mg/ml) onto a thermally evaporated gold coated substrate (ThAu). The monolayer flakes were analysed with the AFM-IR and IR amplitude spectra (GO 1-IRA) and an IR map at 1754 cm^{-1} was acquired (Figure 52).

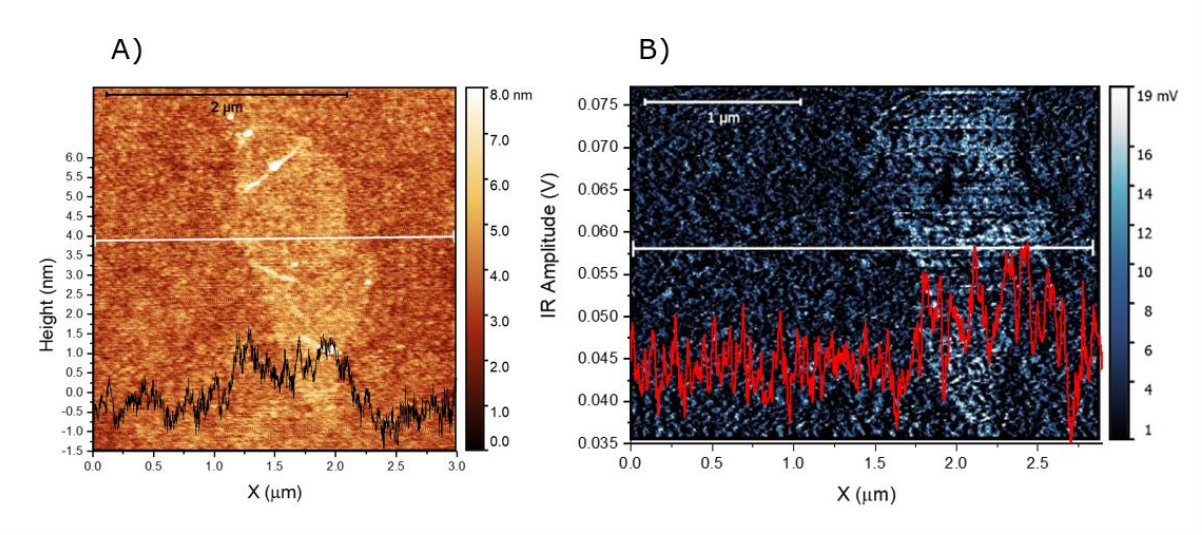

Figure 52 a) AFM topology of monolayer GO an ThAu b) IR amplitude map of monolayer GO flake on ThAu (1654 cm^{-1})

The IR amplitude map on ThAu at 1654 cm^{-1} is particularly noisy and not well defined (Figure 52) due to the high background signals and low IR amplitude signals detected from the flakes. The IR amplitude map seems to suggest that the C-OH of carboxyl group and carbonyl group of the ketones, is not homogenously display onto the flakes, in fact there are some areas where the IR amplitude signal is stronger and where it is less. A similar map has been acquired by Liu *et al.*[118], however, it was not possible to find any difference of the signal near the wrinkles and the edges as Liu reported.

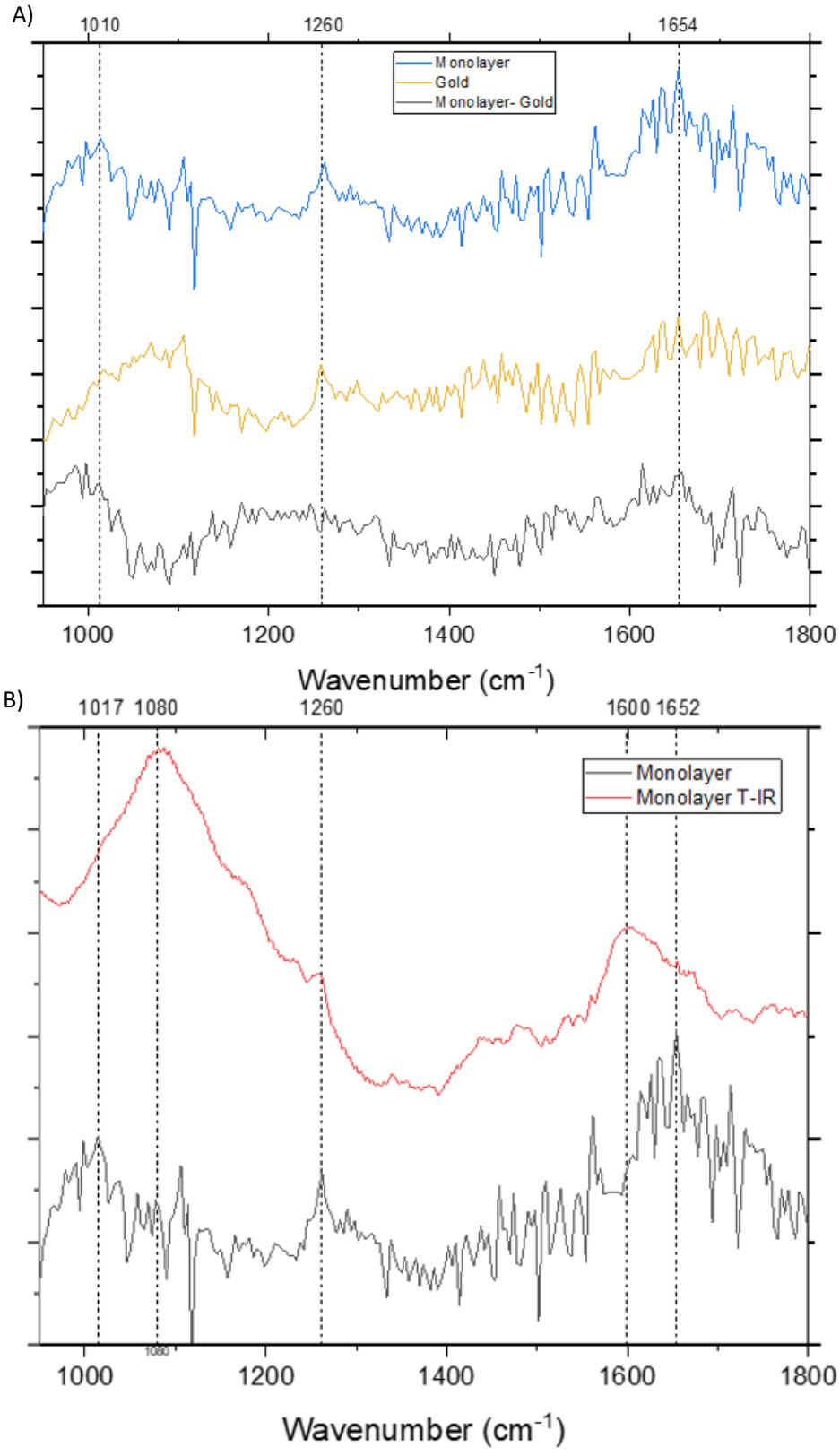

Figure 53 a) Spectra obtained with AFM-IR on monolayer GO (A) prepared by spin coating a GO dispersion (0.1 mg/ml) onto a gold substrate (ThAu) (black) and transmission FTIR (B, red) of monolayer GO (1nm) prepared by spin coating a GO dispersion (0.1 mg/ml) onto CaF_2.

The AFM-IR spectrum (Figure 53) shows only two small peaks at 1010 cm^{-1} and 1260 cm^{-1}, whereas the monolayer T-IR (Figure 53) has a strong absorption peak from 900 cm^{-1} to 1280 cm^{-1} with a maximum at 1080 cm^{-1}. It is interesting to note that the two peaks (1100 cm^{-1} and 1260 cm^{-1}) in IR amplitude spectra (GO 1-IRA) are contained in the FTIR peak (Figure 53), suggesting that only few vibrational modes have been detected by the AFM-IR tip. Moreover, the AFM-IR spectrum shows an absorption at 1650 cm^{-1} with a small shoulder at 1720 cm^{-1}, that could be assigned to the C=O species, which is in good agreement with the conventional FTIR, however with a substantial shift of peak maximum from 1600 cm^{-1} to 1650 cm^{-1} can be observed.

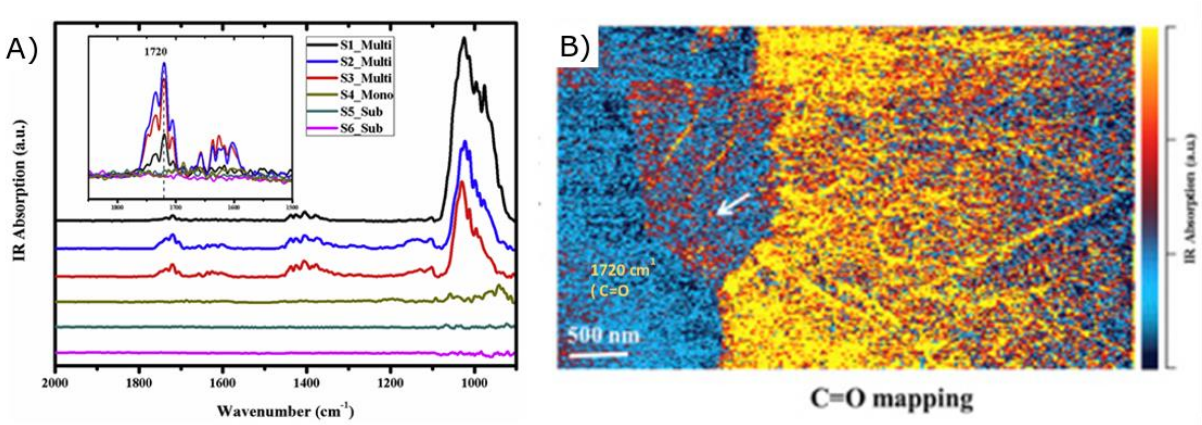

Figure 54 IR amplitude spectra and IR amplitude map (1720 cm^{-1}) acquired by Liu *et al. 2018* of multilayer and monolayer GO [118]

As reported in the literature (Figure 54) [118], the monolayer spectra (GO 1-IRA) displays a low absorption however, it is also possible to distinguish some of the characteristic peaks related to the oxygen species of the GO . Again, one potential explanation for this observed decrease in the IR amplitude signal is the limit of detection of the AFM-IR, where the thermal expansion of the monolayer GO at the particular wavelengths (1754 cm^{-1}) is too low to be sensed by the AFM tip.

Another reason of the low IR amplitude signals could be related to the gold roughness that allows the monolayer GO to expand into the nanometric cavities of the gold surface instead having a z positive expansion. Moreover, the roughness of the gold can reduce significantly the enhancement proposed by Lu *et al.*[7] where the gold substrate, acting as a mirror, focuses the IR signal on the apex of the tip, enhancing the IR amplitude signal. A rougher gold substrate would result in a higher proportion of diffuse reflection and diminish this effect.

6.5 Influence of Substrate on AFM-IR Measurements of GO

To investigate the changes of the IR amplitude signal in relation with the gold roughness, AFM images have been acquired on strip-templated gold (TAu) and thermal-evaporate gold (ThAu). ThAu shows a homogenous roughness all over the sample, Rms ~0,513 nm, whereas TAu displays a grains topology with areas atomically smooth (0,17nm) between the observed Au boundaries (2nm depth).

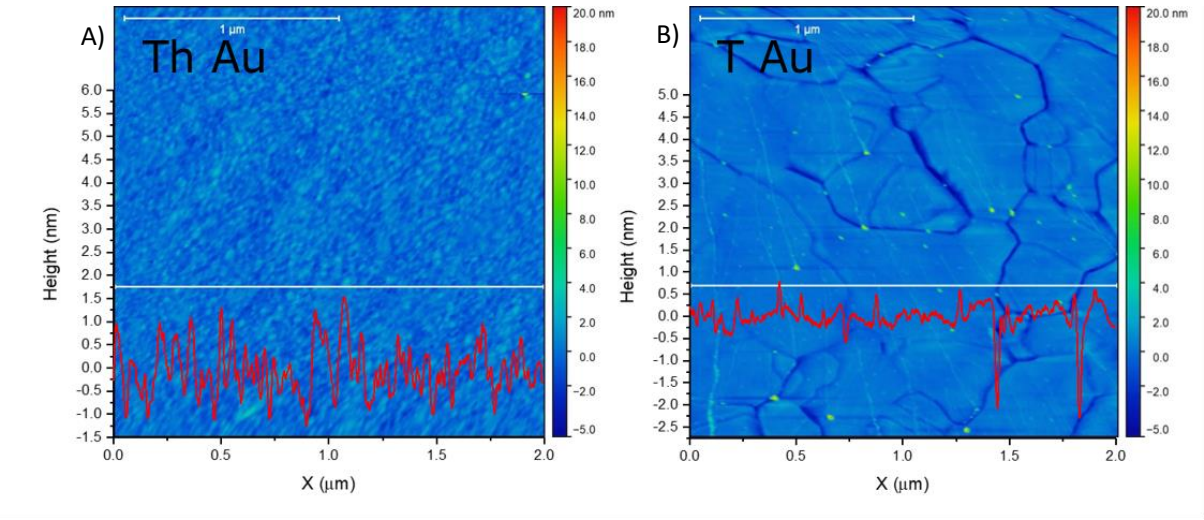

Figure 55 Comparison between ThAu (A) and TAu (B) measured by tapping mode AFM with profiles shown in red.

A monolayer GO sample has been prepared by spin coating a GO dispersion (0.1 mg/ml) onto TAu and subsequently has been analysed by AFM-IR. A GO single flake has been identified by CM-AFM (Figure 56) and three IR amplitude spectra has been acquired on monolayer, three-layer and few-layer GO. Furthermore, four IR amplitude images at wavelength of 1100 cm^{-1} has been performed. Additional confirmation of the flake topology has been gained by SEM imaging (Figure56).

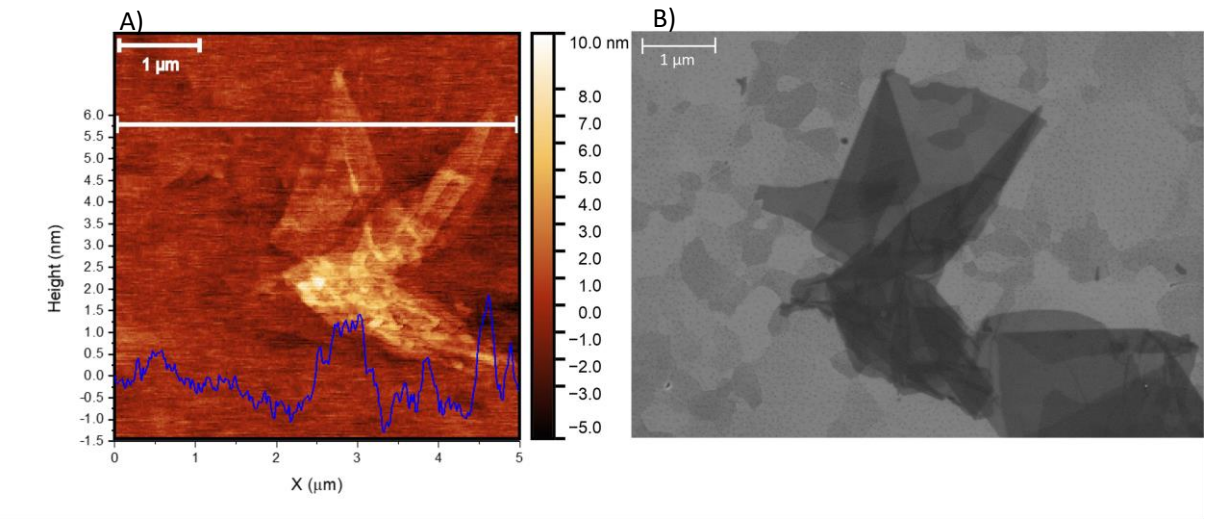

Figure 56 AFM image of monolayer GO flake on TAu with profile (A) and SEM image of the same flake (B).

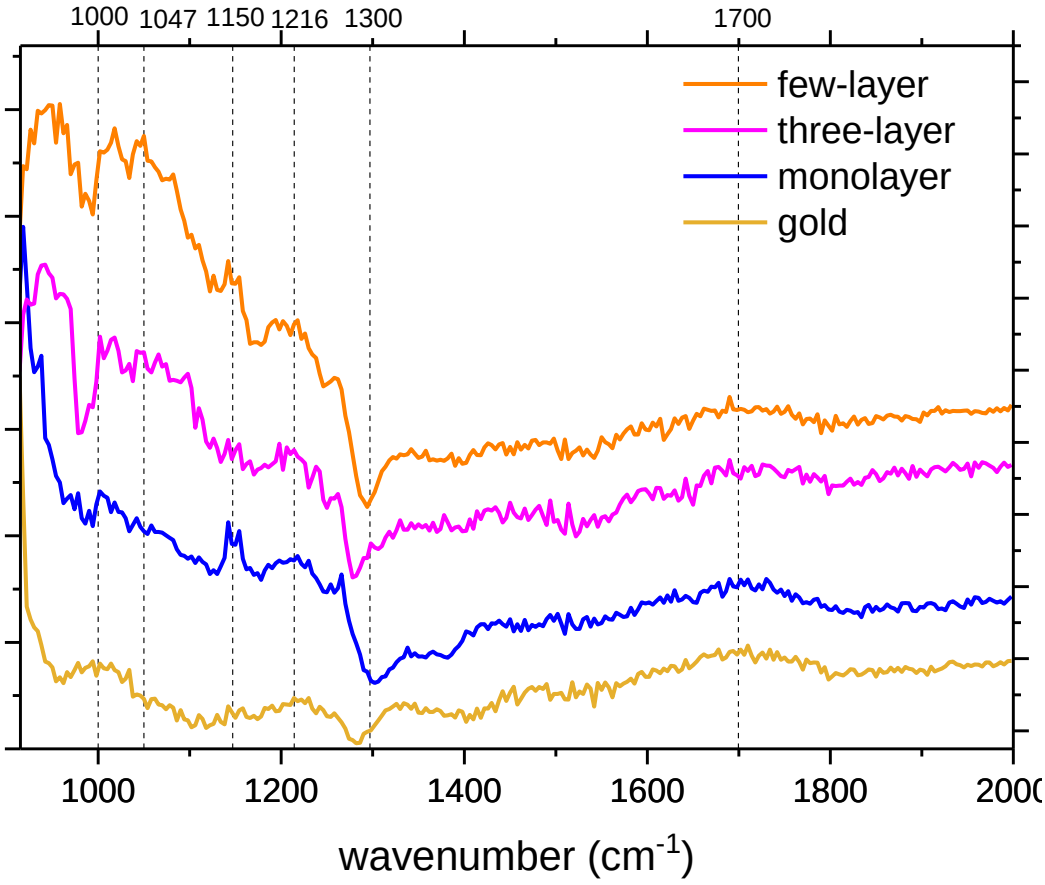

Figure 57 IR amplitude spectra of Multilayer GO, bilayer, monolayer on TAu

The IR amplitude GO spectra: monolayer, three-layer and few-layer show a strong and broad IR absorption peak between 900-1300 cm^{-1}(Figure 57) however, no additional peaks were detected in the 1300-2000 cm^{-1} spectral region.

By using an atomically smooth gold substrate (TAu), it can be seen that the IR amplitude monolayer signal related to the chemical species that vibrate between 900-1300 cm^{-1} are greatly enhanced compared to that on ThAu substrates. According to Acik work, these species include: ether, hydroxyls, carboxyls (900-1100 cm^{-1}), the weak absorption of ketones, peroxides and pyrans (1100-1280 cm^{-1}) and epoxides (1280-1320 cm^{-1}). A control spectrum has been acquired on the TAu gold substrate, the low absorption (1300-2000 cm^{-1}) has attributed to incorrect subtraction of background from the software, as the absorption 1300-2000 cm^{-1} is consistent in all the spectra acquired (monolayer, three-layer and few layer GO). (Figure 57)

Four low scan IR amplitude maps at 1100 cm^{-1} were then acquired on the same flakes and identical experimental conditions. A large enhancement of the IR amplitude signals at 1100 cm^{-1} has been recorded therefore, the laser power has been reduced by 3/4. The IR amplitude signal in the first map acquired exceed the upper limit of 1V all over the flakes (Figure 58). All four IR images show a low signal from the gold substrate (TAu) in comparison with the literature (Liu et al. 2018) and IR amplitude maps acquired on the monolayer sample on ThAu (Figure 52).

Visibly, it can be seen that the GO flake contrast from the substrate has a high level of sharpness and full of details that the CM-AFM images, that were simultaneously acquired, were unable to detect. Moreover, the IR amplitude maps highlights the monolayer region presents in the flakes that was completely invisible in the topology map.

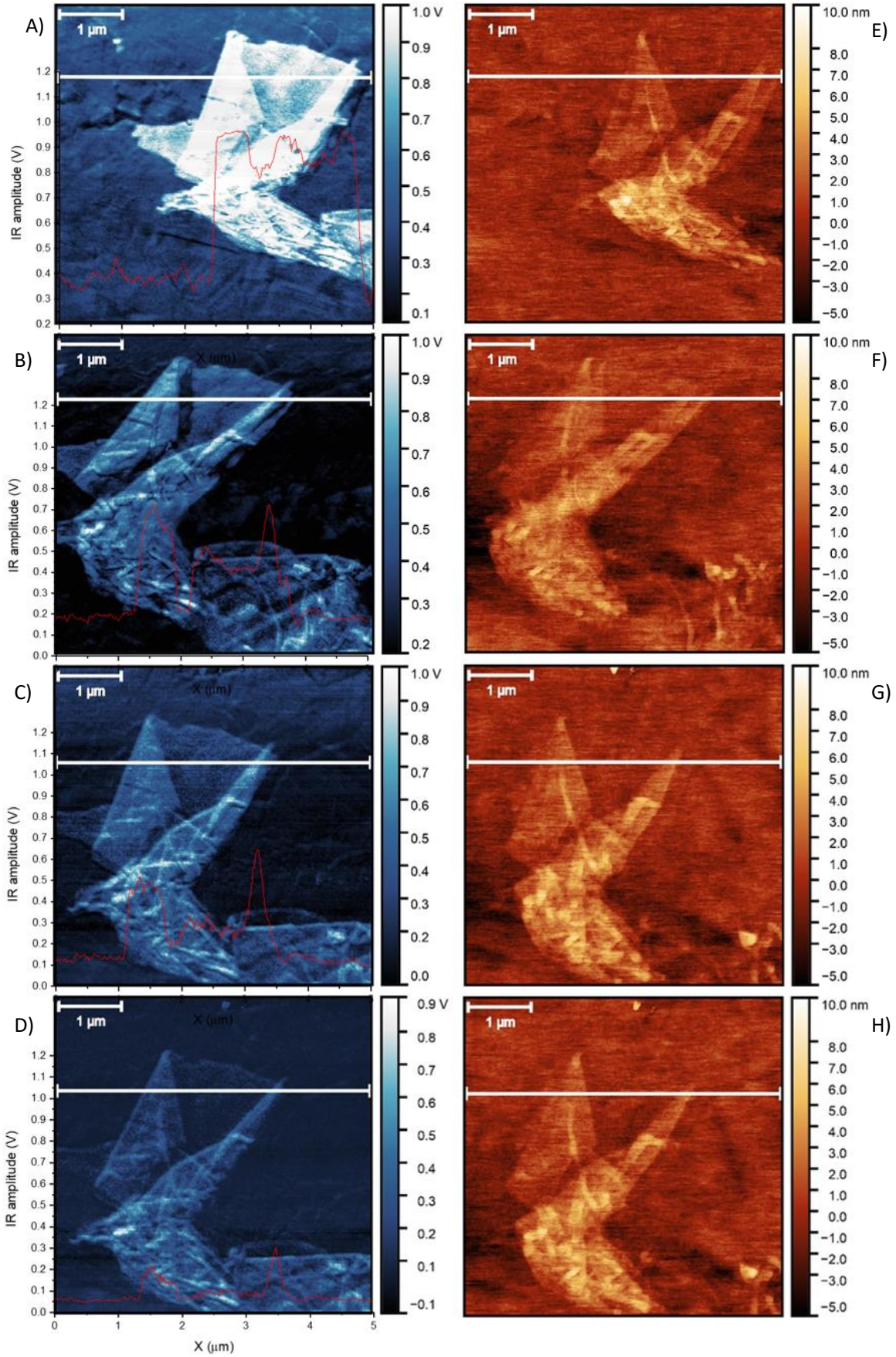

Figure 58 simultaneous acquisition of CM AFM images (E,F,G,H) IR amplitude maps(A,B,C,D) at 1100 of GO flakes and topology (left). The images are scans (top to Bottom) showing decrease is signal during scanning

The decrease of the signal from A) to D) IR amplitude map can be attribute to the loss of the tip-substrate enhancement described by Belkin[138]. Gold coated tips have a relatively low hardness (2.5 Mohs scale) and ductility meaning that the gold coated tip is subject to a grinding process while is scanning onto the surface. This eventually results in the complete removal of the gold coating and the loss of signal enhancement. SEM images of AFM-IR tip has been acquired before and after the measurement highlighting the partial grained of the apex of AFM tip form 30 nm to 100 nm and the losses of the gold coating onto the tip apex (Figure 59).

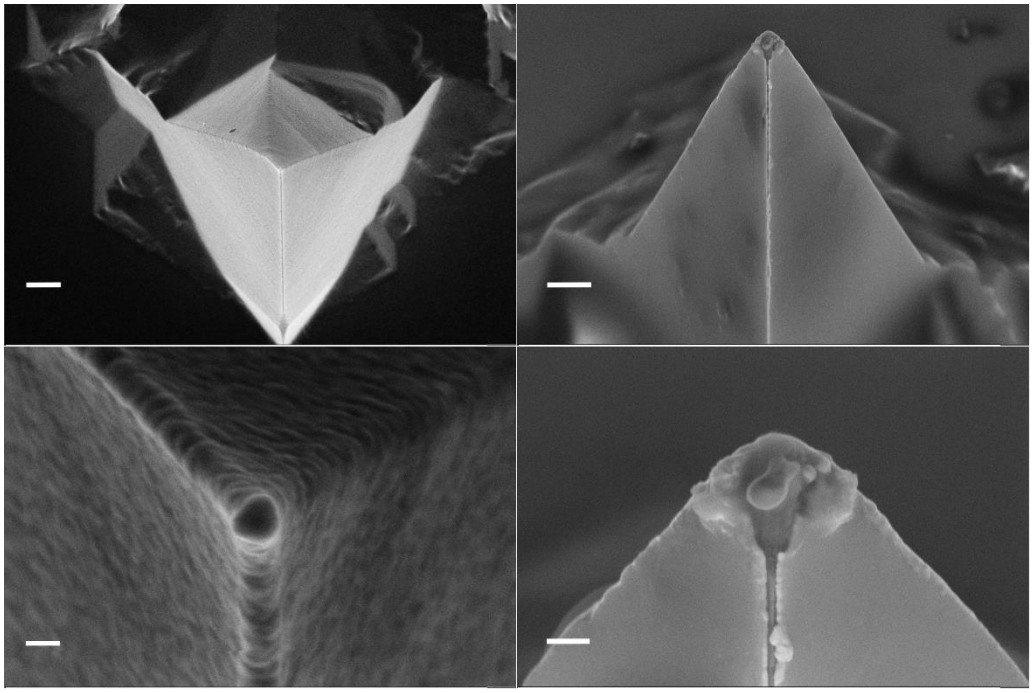

Figure 59 SEM imaging of an new AFM-IR tip at low magnification (top left, scale - 1 µm), high magnification (bottom left, scale – 40 nm) and a used AFM-IR tip at low magnification (top right, scale - 1 µm), high magnification (bottom right, scale – 200 nm).

To prove the repeatability of the mapping with new AFM-IR tips, a second monolayer sample has been prepared on TAu and three IR amplitude maps (1100 cm^{-1}, 1500 cm^{-1} and 1754 cm^{-1}) were acquired in the same region. As expected, a strong IR signal related mainly to the C-O vibrational mode was detected at 1100 cm^{-1}. At 1754 cm^{-1}, the thermal expansion of the carboxyl and carbonyl group can be seen to a lesser extent to the IR map at 1100 cm^{-1}. A control map at 1500 cm^{-1} has been acquired showing blank map and this result agrees with the conventional FTIR where no IR signal is expected. This map goes some way to showing the optimisation of the AFM-IR technique for monolayer characterisation of GO flakes. By optimisation of the tip and substrate, reliable IR spectroscopic maps of GO can be achieved at the nanoscale[139].

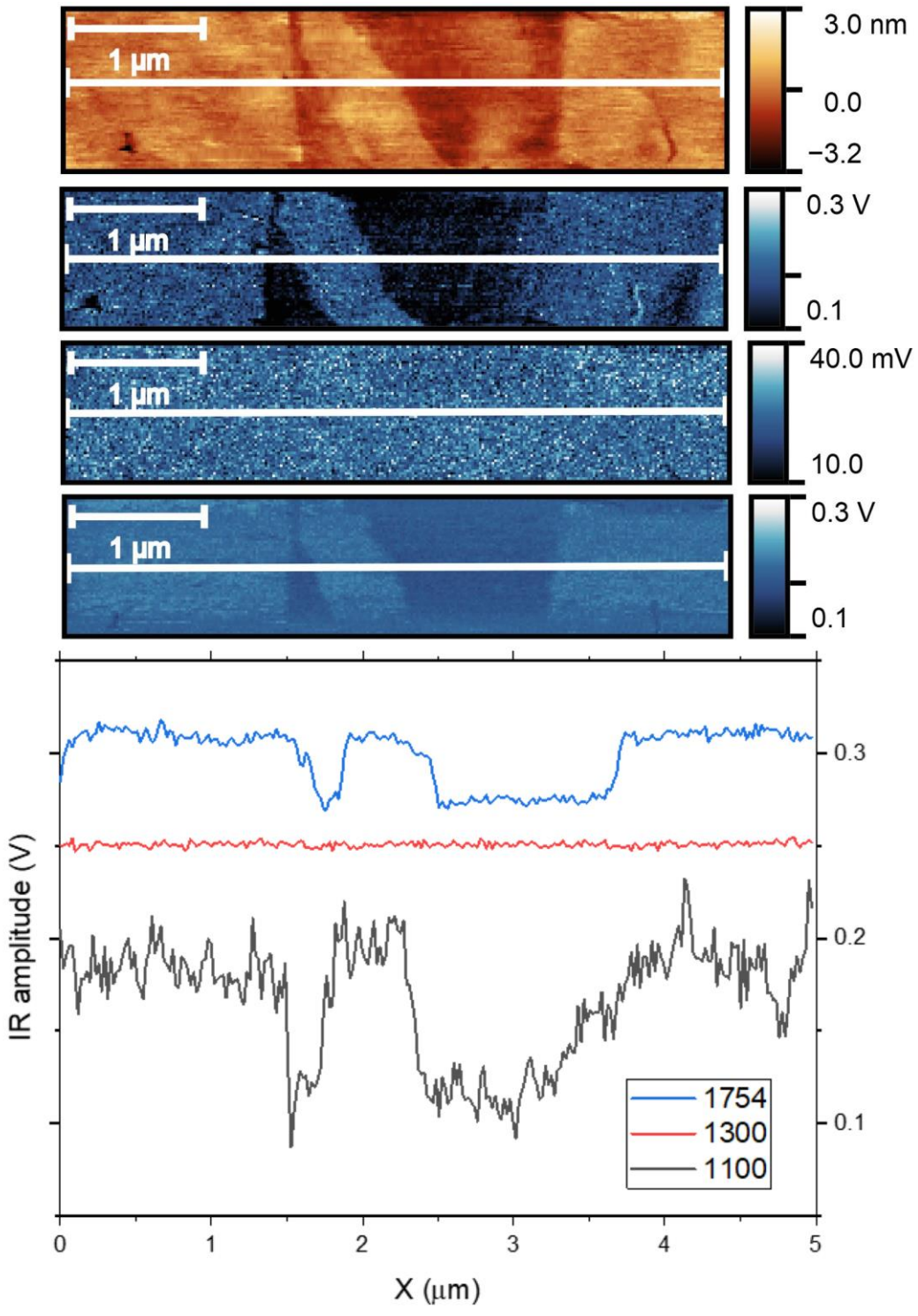

Figure 60 From top to bottom - AFM topology, and IR amplitude maps at 1100, 1300, 1754 cm^{-1}. The graph at the bottom shows the profile from the IR amplitude maps (inverted)

7 Conclusions and Further Work

In the initial part of this project a comprehensive characterisation of commercial GO was achieved by SEM, AFM, XPS, ATR-FTIR and Raman spectroscopy. AFM imaging has been used to confirm the monolayer nature of the GO dispersion. High magnification SEM images were acquired to measure the flake size distribution and Raman spectroscopy analysis indicated the high level of oxygen defects on the GO flakes. The level of oxidation has been quantified through XPS measurement, consisting in highly oxidised GO.

Bulk GO FTIR analysis confirmed the presence of several oxygen species including ethers, carbonyl ketones, carboxyl, hydroxyls, peroxides and epoxides. Transmission FT-IR analysis has been used to acquire FTIR spectra of monolayer and few-layer GO, highlighting the thickness dependency of the IR GO spectra.

The results obtained through comparing ATR-FTIR on bulk GO material and AFM-IR analysis on thin films and monolayer flakes highlight the discrepancy between the two IR spectroscopy techniques, below the critical samples thickness of 0.7 µm. The IR amplitude signal decreased drastically within the sample thickness from 60 nm to 1 nm, especially in the monolayer sample, which display an extremely low IR amplitude signal, in agreement with the previous literature[118].

The effect of substrate roughness on AFM-IR analysis was also investigated. By using an atomically smooth gold substrate, it has been shown that the IR amplitude signal of monolayer GO can be enhanced in the region 900-1300 cm^{-1}, relating to the vibrational mode of ether, hydroxyls, carboxyls ketones, peroxides, pyrans and epoxides, showing features on the nanoscale that are present in bulk ATR-FTIR measurements. Moreover, using this gold substrate has been possible to significantly improve signal intensity and the quality of the IR amplitude maps acquired, which can be attributed to improved specular reflection. The results obtained highlight the importance of using atomically smooth gold substrate in order to improve both spectral and spatial sensitivity in AFM-IR paves the way for improved 2D material mapping and structural determination with this technique.

AFM-IR is not currently widely used to characterise 2D materials and the potential avenues for exploration are far-reaching with this technique. The current limitation of using the AFM-IR to characterise GO, is the extremely low IR amplitude signal reported for monolayer GO in

the spectra region between 1300-2000 cm^{-1} . This could be related to orientation of the carbon-oxygen species and their vibrational mode. However, it is possible to qualitatively detect carbon-oxygen species (1300-2000 cm^{-1}) by acquiring a high resolution IR amplitude map. Resonance-enhanced AFM-IR could have the potential to increase the signal to noise ratio, by matching the resonance mode of the cantilever and the laser pulse.

The spectral enhancement that was noted on edges and wrinkles discussed in SECTION is potentially one of great interest. An exciting property of 2D materials is that they can be suspended[140], and their planar geometry can be manipulated. If this enhancement truly is caused by orientating the GO in different planes, then this has great potential to increase the spectral sensitivity of this technique even further.

References:

1. Ferrari, A. C. *et al.* Science and technology roadmap for graphene, related two-dimensional crystals, and hybrid systems. *Nanoscale* **7**, 4598–4810 (2015).
2. Iliut, M., Silva, C., Herrick, S., McGlothlin, M. & Vijayaraghavan, A. Graphene and water-based elastomers thin-film composites by dip-moulding. *Carbon N. Y.* **106**, 228–232 (2016).
3. Leaper, S. *et al.* Flux-enhanced PVDF mixed matrix membranes incorporating APTS-functionalized graphene oxide for membrane distillation. *J. Memb. Sci.* **554**, 309–323 (2018).
4. Bartlam, C. *et al.* Nanoscale infrared identification and mapping of chemical functional groups on graphene. *Carbon N. Y.* **139**, 317–324 (2018).
5. Dreyer, D. R. *et al.* The chemistry of graphene oxide. *Chem. Soc. Rev.* **39**, 228–40 (2010).
6. Morsch, S., Liu, Y., Greensmith, P., Lyon, S. B. & Gibbon, S. R. Molecularly controlled epoxy network nanostructures. *Polym. (United Kingdom)* **108**, 146–153 (2017).
7. Lu, F., Jin, M. & Belkin, M. A. Tip-enhanced infrared nanospectroscopy via molecular expansion force detection. *Nat. Photonics* **8**, 307–312 (2014).
8. Proctor, J. E., Armada, D. M. & Vijayaraghavan, A. *An Introduction to Graphene and Carbon Nanotubes*. (CRC Press LLC, 2017).
9. Kroto, H. W., Heath, J. R., O'Brien, S. C., Curl, R. F. & Smalley, R. E. C60: Buckminsterfullerene. *Nature* **318**, 162–163 (1985).
10. Iijima, S. Helical microtubules of graphitic carbon. *Nature* **354**, 56–58 (1991).
11. Ehrenfreund, P. & Foing, B. H. Astronomy. Fullerenes and cosmic carbon. *Science* **329**, 1159–60 (2010).
12. Wallace, P. R. & Ace, P. R. W. The Band Theory of Graphite. *Phys. Rev.* **71**, (1947).
13. Katsnelson, M. I. Graphene: carbon in two dimensions. *Mater. Today* **10**, 20–27 (2007).
14. Novoselov, K. S. *et al.* Electric field effect in atomically thin carbon films. *Science* **306**, 666–9 (2004).
15. Fasolino, A., Los, J. H. & Katsnelson, M. I. Intrinsic ripples in graphene.

Nat. Mater. **6**, 858–861 (2007).

16. Li, W. *et al.* Flexible Circuits and Soft Actuators by Printing Assembly of Graphene. *ACS Appl. Mater. Interfaces* **8**, 12369–12376 (2016).
17. Duplock, E. J., Scheffler, M. & Lindan, P. J. D. Hallmark of Perfect Graphene. *Phys. Rev. Lett.* **92**, 225502 (2004).
18. Vaiva Nagyte. Raman Spectroscopy of Graphene-based Formulations.
19. Novoselov, K. S. *et al.* Two-dimensional gas of massless Dirac fermions in graphene. *Nature* **438**, 197–200 (2005).
20. Cahn, R. W. Physics of graphite: B.T. Kelly (Applied Science Publishers, London, 1981) pp. 477. price: £48. *J. Nucl. Mater.* **114**, 116 (1983).
21. Novoselov, K. S. *et al.* Electric Field Effect in Atomically Thin Carbon Films. *Science (80-.).* **306**, 666–669 (2004).
22. Katsnelson, M. I., Novoselov, K. S. & Geim, A. K. Chiral tunnelling and the Klein paradox in graphene. *Nat. Phys.* **2**, 620–625 (2006).
23. Shearer, C. J., Slattery, A. D., Stapleton, A. J., Shapter, J. G. & Gibson, C. T. Accurate thickness measurement of graphene. *Nanotechnology* **27**, 125704 (2016).
24. Lee, C., Wei, X., Kysar, J. W. & Hone, J. Measurement of the elastic properties and intrinsic strength of monolayer graphene. *Science* **321**, 385–8 (2008).
25. Balandin, A. A., Ghosh, S., Bao, W. & Calizo, I. Superior Thermal Conductivity of. *Nano Lett.* **8**, 902–907 (2008).
26. Nair, R. R. *et al.* Fine structure constant defines visual transparency of graphene. *Science (80-.).* **320**, 1308 (2008).
27. Hu, S. *et al.* Proton transport through one-atom-thick crystals. *Nature* **516**, 227–230 (2014).
28. Raccichini, R., Varzi, A., Passerini, S. & Scrosati, B. The role of graphene for electrochemical energy storage. *Nat. Mater.* **14**, 271–279 (2015).
29. Novoselov, K. S. *et al.* A roadmap for graphene. *Nature* **490**, 192–200 (2012).
30. Bolotin, K. I. *et al.* Ultrahigh electron mobility in suspended graphene. *Solid State Commun.* **146**, 351–355 (2008).
31. Morozov, S. V. *et al.* Giant Intrinsic Carrier Mobilities in Graphene and Its Bilayer. *Phys. Rev. Lett.* **100**, 016602 (2008).

32. Du, X., Skachko, I., Barker, A. & Andrei, E. Y. Approaching ballistic transport in suspended graphene. *Nat. Nanotechnol.* **3**, 491–495 (2008).

33. Vijayaraghavan, A. Graphene - Properties and characterization. in *Springer Handbook of Nanomaterials* 39–82 (Springer Berlin Heidelberg, 2013). doi:10.1007/978-3-642-20595-8_2

34. Geim, A. K. & Novoselov, K. S. The rise of graphene. *Nat. Mater.* **6**, 183–191 (2007).

35. Li, X. *et al.* Large-area synthesis of high-quality and uniform graphene films on copper foils. *Science* **324**, 1312–4 (2009).

36. Dong, X. *et al.* Growth of large-sized graphene thin-films by liquid precursor-based chemical vapor deposition under atmospheric pressure. *Carbon N. Y.* **49**, 3672–3678 (2011).

37. Papageorgiou, D. G., Kinloch, I. A. & Young, R. J. Mechanical properties of graphene and graphene-based nanocomposites. (2017). doi:10.1016/j.pmatsci.2017.07.004

38. Marchini, S., Günther, S. & Wintterlin, J. Scanning tunneling microscopy of graphene on Ru(0001). *Phys. Rev. B* **76**, 075429 (2007).

39. Vázquez de Parga, A. L. *et al.* Periodically Rippled Graphene: Growth and Spatially Resolved Electronic Structure. *Phys. Rev. Lett.* **100**, 056807 (2008).

40. Sutter, P. W., Flege, J.-I. & Sutter, E. A. Epitaxial graphene on ruthenium. *Nat. Mater.* **7**, 406–411 (2008).

41. Ruan, G., Sun, Z., Peng, Z. & Tour, J. M. Growth of Graphene from Food, Insects, and Waste. *ACS Nano* **5**, 7601–7607 (2011).

42. Chen, X., Zhang, L. & Chen, S. Large area CVD growth of graphene. *Synth. Met.* **210**, 95–108 (2015).

43. Ago, H. *et al.* Epitaxial CVD growth of high-quality graphene and recent development of 2D heterostructures. *Tech. Dig. - Int. Electron Devices Meet. IEDM* **2016**–**Febru**, 27.2.1-27.2.4 (2015).

44. Suk, J. W. *et al.* Transfer of CVD-Grown Monolayer Graphene onto Arbitrary Substrates. *ACS Nano* **5**, 6916–6924 (2011).

45. Kotakoski, J. & Meyer, J. C. Mechanical properties of polycrystalline graphene based on a realistic atomistic model. *Phys. Rev. B* **85**, 195447 (2012).

46. Babenko, V. *et al.* Rapid epitaxy-free graphene synthesis on silicidated

polycrystalline platinum. *Nat. Commun.* **6**, 7536 (2015).

47. Hernandez, Y. *et al.* High-yield production of graphene by liquid-phase exfoliation of graphite. *Nat. Nanotechnol.* **3**, 563–568 (2008).

48. Paton, K. R. *et al.* Scalable production of large quantities of defect-free few-layer graphene by shear exfoliation in liquids. *Nat. Mater.* **13**, 624–630 (2014).

49. Gao, W., Recipes, R. & Hengqiu. *Graphene Oxide*. **45**, (Springer International Publishing, 2015).

50. Chen, D., Feng, H. & Li, J. Graphene oxide: Preparation, functionalization, and electrochemical applications. *Chemical Reviews* **112**, 6027–6053 (2012).

51. Schniepp, H. C. *et al.* Functionalized single graphene sheets derived from splitting graphite oxide. *J. Phys. Chem. B* **110**, 8535–8539 (2006).

52. Gómez-Navarro, C. *et al.* Atomic Structure of Reduced Graphene Oxide. *Nano Lett.* **10**, 1144–1148 (2010).

53. Fiorillo, M. *et al.* Graphene oxide selectively targets cancer stem cells, across multiple tumor types: Implications for non-toxic cancer treatment, via “differentiation-based nano-therapy” *Oncotarget* **6**, 3553–3562 (2015).

54. Brodie, B. C. On the Atomic Weight of Graphite. *Philos. Trans. R. Soc. London* **149**, 249–259 (1859).

55. Staudenmaier, L. Verfahren zur Darstellung der Graphitsäure. *Berichte der Dtsch. Chem. Gesellschaft* **31**, 1481–1487 (1898).

56. Hummers, W. S. & Offeman, R. E. Preparation of Graphitic Oxide. *J. Am. Chem. Soc.* **80**, 1339–1339 (1958).

57. Kovtyukhova, N. I. Layer-by-layer assembly of ultrathin composite films from micron-sized graphite oxide sheets and polycations. *Chem. Mater.* **11**, 771–778 (1999).

58. Singh, R. K., Kumar, R. & Singh, D. P. Graphene oxide: strategies for synthesis, reduction and frontier applications. *RSC Adv.* **6**, 64993–65011 (2016).

59. Dresselhaus, M. S. & Dresselhaus, G. Intercalation compounds of graphite. *Adv. Phys.* **30**, 139–326 (1981).

60. Compton, O. C. & Nguyen, S. T. Graphene Oxide, Highly Reduced Graphene Oxide, and Graphene: Versatile Building Blocks for Carbon-

Based Materials. *Small* **6**, 711–723 (2010).

61. Athanasios B. Bourlinos, † *et al.* Graphite Oxide: Chemical Reduction to Graphite and Surface Modification with Primary Aliphatic Amines and Amino Acids. (2003). doi:10.1021/LA026525H

62. Kovtyukhova, N. I. Layer-by-layer assembly of ultrathin composite films from micron-sized graphite oxide sheets and polycations. *Chem. Mater.* **11**, 771–778 (1999).

63. Anton Lerf, *,‡, Heyong He, §, Michael Forster, ‡ and & Jacek Klinowski*, †,§. Structure of Graphite Oxide Revisited‖. (1998). doi:10.1021/JP9731821

64. Lerf, A. *et al.* Hydration behavior and dynamics of water molecules in graphite oxide. *J. Phys. Chem. Solids* **67**, 1106–1110 (2006).

65. Szabó, T. *et al.* Evolution of Surface Functional Groups in a Series of Progressively Oxidized Graphite Oxides Evolution of Surface Functional Groups in a Series of Progressively Oxidized Graphite Oxides. *Chem. Mater.* **18**, 2740–2749 (2006).

66. Shih, C. J. *et al.* Bi- and trilayer graphene solutions. *Nat. Nanotechnol.* **6**, 439–445 (2011).

67. Chuang, C.-H. *et al.* The effect of thermal reduction on the photoluminescence and electronic structures of graphene oxides. *Sci. Rep.* **4**, 4525 (2014).

68. Scott Gilje, †, Song Han, ‡, Minsheng Wang, ‡, Kang L. Wang, ‡ and & Richard B. Kaner*, †. A Chemical Route to Graphene for Device Applications. (2007). doi:10.1021/NL0717715

69. Shin, H.-J. *et al.* Efficient Reduction of Graphite Oxide by Sodium Borohydride and Its Effect on Electrical Conductance. *Adv. Funct. Mater.* **19**, 1987–1992 (2009).

70. Moon, I. K., Lee, J., Ruoff, R. S. & Lee, H. Reduced graphene oxide by chemical graphitization. *Nat. Commun.* **1**, 1–6 (2010).

71. Pei, S., Zhao, J., Du, J., Ren, W. & Cheng, H.-M. Direct reduction of graphene oxide films into highly conductive and flexible graphene films by hydrohalic acids. *Carbon N. Y.* **48**, 4466–4474 (2010).

72. Fernández-Merino, M. J. *et al.* Vitamin C Is an Ideal Substitute for Hydrazine in the Reduction of Graphene Oxide Suspensions. *J. Phys. Chem. C* **114**, 6426–6432 (2010).

73. De Silva, K. K. H., Huang, H.-H., Joshi, R. K. & Yoshimura, M. Chemical

reduction of graphene oxide using green reductants. *Carbon N. Y.* **119**, 190–199 (2017).

74. Zhou, M. *et al.* Controlled Synthesis of Large-Area and Patterned Electrochemically Reduced Graphene Oxide Films. *Chem. - A Eur. J.* **15**, 6116–6120 (2009).

75. Michael J. McAllister, † *et al.* Single Sheet Functionalized Graphene by Oxidation and Thermal Expansion of Graphite. (2007). doi:10.1021/CM0630800

76. Hannes C. Schniepp, † *et al.* Functionalized Single Graphene Sheets Derived from Splitting Graphite Oxide. (2006). doi:10.1021/JP060936F

77. Paredes, J. I., Villar-Rodil, S., Martínez-Alonso, A. & Tascón, J. M. D. Graphene Oxide Dispersions in Organic Solvents. *Langmuir* **24**, 10560–10564 (2008).

78. Park, S. & Ruoff, R. S. Chemical methods for the production of graphenes. *Nat. Nanotechnol.* **4**, 217–224 (2009).

79. Kim, F., Cote, L. J. & Huang, J. Graphene Oxide: Surface Activity and Two-Dimensional Assembly. *Adv. Mater.* **22**, 1954–1958 (2010).

80. Mattevi, C. *et al.* Evolution of Electrical, Chemical, and Structural Properties of Transparent and Conducting Chemically Derived Graphene Thin Films. *Adv. Funct. Mater.* **19**, 2577–2583 (2009).

81. Eda, G., Fanchini, G. & Chhowalla, M. Large-area ultrathin films of reduced graphene oxide as a transparent and flexible electronic material. *Nat. Nanotechnol.* **3**, 270–274 (2008).

82. Eda, G. & Chhowalla, M. Chemically Derived Graphene Oxide: Towards Large-Area Thin-Film Electronics and Optoelectronics. *Adv. Mater.* **22**, 2392–2415 (2010).

83. Elias, D. C. *et al.* Control of Graphene's Properties by Reversible Hydrogenation: Evidence for Graphane. *Science (80-.).* **323**, 610–613 (2009).

84. Gómez-Navarro, C. *et al.* Electronic transport properties of individual chemically reduced graphene oxide sheets. *Nano Lett.* **7**, 3499–3503 (2007).

85. Lerf, A., He, H., Forster, M. & Klinowski, J. Structure of Graphite Oxide Revisited ‖. *J. Phys. Chem. B* **102**, 4477–4482 (1998).

86. Gao, W., Alemany, L. B., Ci, L. & Ajayan, P. M. New insights into the structure and reduction of graphite oxide. *Nat. Chem.* **1**, 403–408 (2009).

87. Li, X. *et al.* Highly conducting graphene sheets and Langmuir–Blodgett films. *Nat. Nanotechnol.* **3**, 538–542 (2008).

88. Stankovich, S. *et al.* Synthesis of graphene-based nanosheets via chemical reduction of exfoliated graphite oxide. *Carbon N. Y.* **45**, 1558–1565 (2007).

89. Cote, L. J., Kim, F. & Huang, J. Langmuir−Blodgett Assembly of Graphite Oxide Single Layers. *J. Am. Chem. Soc.* **131**, 1043–1049 (2009).

90. Paredes, J. I., Villar-Rodil, S., Solís-Fernández, P., Martínez-Alonso, A. & Tascón, J. M. D. Atomic Force and Scanning Tunneling Microscopy Imaging of Graphene Nanosheets Derived from Graphite Oxide. *Langmuir* **25**, 5957–5968 (2009).

91. Mativetsky, J. M. *et al.* Local Current Mapping and Patterning of Reduced Graphene Oxide. *J. Am. Chem. Soc.* **132**, 14130–14136 (2010).

92. Kudin, K. N. *et al.* Raman Spectra of Graphite Oxide and Functionalized Graphene Sheets. *Nano Lett.* **8**, 36–41 (2008).

93. Erickson, K. *et al.* Determination of the Local Chemical Structure of Graphene Oxide and Reduced Graphene Oxide. *Adv. Mater.* **22**, 4467–4472 (2010).

94. Pantelic, R. S., Meyer, J. C., Kaiser, U., Baumeister, W. & Plitzko, J. M. Graphene oxide: A substrate for optimizing preparations of frozen-hydrated samples. *J. Struct. Biol.* **170**, 152–156 (2010).

95. Pacilé, D. *et al.* Electronic properties and atomic structure of graphene oxide membranes. *Carbon N. Y.* **49**, 966–972 (2011).

96. Mkhoyan, K. A. *et al.* Atomic and Electronic Structure of Graphene-Oxide. *Nano Lett.* **9**, 1058–1063 (2009).

97. Cai, W. *et al.* Synthesis and solid-state NMR structural characterization of 13C-labeled graphite oxide. *Science* **321**, 1815–7 (2008).

98. Ganguly, A., Sharma, S., Papakonstantinou, P. & Hamilton, J. Probing the Thermal Deoxygenation of Graphene Oxide Using High-Resolution In Situ X-ray-Based Spectroscopies. *J. Phys. Chem. C* **115**, 17009–17019 (2011).

99. Yang, D. *et al.* Chemical analysis of graphene oxide films after heat and chemical treatments by X-ray photoelectron and Micro-Raman spectroscopy. *Carbon N. Y.* **47**, 145–152 (2009).

100. Pimenta, M. A. *et al.* Studying disorder in graphite-based systems by Raman spectroscopy. *Phys. Chem. Chem. Phys.* **9**, 1276–1290 (2007).

101. Bartlam, C. *et al.* Nanoscale infrared identification and mapping of chemical functional groups on graphene. *Carbon N. Y.* **139**, (2018).

102. King, A. A. K. *et al.* A New Raman Metric for the Characterisation of Graphene oxide and its Derivatives. *Sci. Rep.* **6**, 19491 (2016).

103. Acik, M. *et al.* The Role of Oxygen during Thermal Reduction of Graphene Oxide Studied by Infrared Absorption Spectroscopy. *J. Phys. Chem. C* **115**, 19761–19781 (2011).

104. Acik, M. *et al.* The Role of Intercalated Water in Multilayered Graphene Oxide. *ACS Nano* **4**, 5861–5868 (2010).

105. Dazzi, A. & Prater, C. B. AFM-IR: Technology and applications in nanoscale infrared spectroscopy and chemical imaging. *Chem. Rev.* **117**, 5146–5173 (2017).

106. Amarie, S., Ganz, T. & Keilmann, F. Mid-infrared near-field spectroscopy. *Opt. Express* **17**, 21794 (2009).

107. Markus Brehm, Thomas Taubner, †, Rainer Hillenbrand, and & Keilmann*, F. Infrared Spectroscopic Mapping of Single Nanoparticles and Viruses at Nanoscale Resolution. (2006). doi:10.1021/NL0610836

108. Gross, N. *et al.* Infrared near-field study of a localised absorption in a thin film. *Eur. Phys. J. Appl. Phys.* **16**, 91–98 (2001).

109. Hammiche, A. *et al.* Photothermal FT-IR Spectroscopy: A Step towards FT-IR Microscopy at a Resolution Better Than the Diffraction Limit. *Appl. Spectrosc.* **53**, 810–815 (1999).

110. Anderson, M. S. Infrared Spectroscopy with an Atomic Force Microscope. *Appl. Spectrosc.* **54**, 349–352 (2000).

111. Hammiche, A., Bozec, L., Pollock, H. M., German, M. & Reading, M. Progress in near-field photothermal infra-red microspectroscopy. *J. Microsc.* **213**, 129–134 (2004).

112. Dazzi, A., Prazeres, R., Glotin, F. & Ortega, J. M. Local infrared microspectroscopy with subwavelength spatial resolution with an atomic force microscope tip used as a photothermal sensor. *Opt. Lett.* **30**, 2388 (2005).

113. Dazzi, A. *et al.* AFM – IR : Combining Atomic Force Microscopy and Infrared Spectroscopy for Nanoscale Chemical Characterization. *Appl. Spectrosc.* **66 N62**, 1365–1384 (2012).

114. Hill, G. A. *et al.* Submicrometer infrared surface imaging using a scanning-probe microscope and an optical parametric oscillator laser. *Opt. Lett.* **34**,

431 (2009).

115. Kjoller, K., Felts, J. R., Cook, D., Prater, C. B. & King, W. P. High-sensitivity nanometer-scale infrared spectroscopy using a contact mode microcantilever with an internal resonator paddle. *Nanotechnology* **21**, 185705 (2010).
116. Marcott, C. *et al.* Nanoscale infrared spectroscopy of biopolymeric materials. *Soc. Adv. Mater. Process Eng. Tech. 2012 Conf.* 1–9 (2012).
117. Lu, F. & Belkin, M. A. Infrared absorption nano-spectroscopy using sample photoexpansion induced by tunable quantum cascade lasers. *Opt. Express* **19**, 19942 (2011).
118. Liu, Z. *et al.* Direct observation of oxygen configuration on individual graphene oxide sheets. *Carbon N. Y.* **127**, 141–148 (2018).
119. Pais, A. Einstein and the quantum theory. *Rev. Mod. Phys.* **51**, 863–914 (1979).
120. Alov, N. V. Fifty years of x-ray photoelectron spectroscopy. *J. Anal. Chem.* **60**, 297–300 (2005).
121. XPS. Available at: http://www.rowbo.info/XPS.html. (Accessed: 6th August 2018)
122. RAMAN, C. V. & KRISHNAN, K. S. A New Type of Secondary Radiation. *Nature* **121**, 501–502 (1928).
123. Casiraghi, C. *CDT NOWNANO handouts 'Optical Spectroscopy of Nano-Materials'*. (2006).
124. Rulli, C. The Raman Spectrophotometer.
125. Bogner, A., Jouneau, P. H., Thollet, G., Basset, D. & Gauthier, C. A history of scanning electron microscopy developments: Towards 'wet-STEM' imaging. *Micron* **38**, 390–401 (2007).
126. Characterization Techniques for Nanomaterials. in *Nanotechnology-Enabled Sensors* 211–281 (Springer US, 2008). doi:10.1007/978-0-387-68023-1_5
127. Why is carbon dioxide microwave inactive and IR active? - Quora. Available at: https://www.quora.com/Why-is-carbon-dioxide-microwave-inactive-and-IR-active. (Accessed: 6th August 2018)
128. CLINICAL PATHOLOGY/DRUG DEVELOPMENT/LIVE CELL IMAGING: High-confidence, high-throughput screening with high-def IR microspectroscopy - BioOptics World. Available at:

https://www.bioopticsworld.com/articles/print/volume-7/issue-2/features/clinical-pathology-drug-development-live-cell-imaging-high-confidence-high-throughput-screening-with-high-def-ir-microspectroscopy.html. (Accessed: 11th February 2019)

129. OMT. *Wayback Machine*. *World Tourism Organization* (1995).
130. Phillip, H. R. & Taft, E. A. Kramers-Kronig Analysis of Reflectance Data for Diamond. *Phys. Rev.* **136**, A1445--A1448 (1964).
131. Atomic Force Microscopy - Nanoscience Instruments. Available at: https://www.nanoscience.com/techniques/atomic-force-microscopy/. (Accessed: 11th February 2019)
132. William Blythe. Graphene oxide analysis. (2016). Available at: https://www.go-graphene.com/pages/graphene-oxide-analysis. (Accessed: 30th July 2018)
133. Gao, W. *et al.* Effect of flake size on the mechanical properties of graphene aerogels prepared by freeze casting. *RSC Adv.* **7**, 33600–33605 (2017).
134. Eigler, S. *et al.* Statistical Raman Microscopy and Atomic Force Microscopy on Heterogeneous Graphene Obtained after Reduction of Graphene Oxide. *J. Phys. Chem. C* **118**, 7698–7704 (2014).
135. Kim, S.-G., Park, O.-K., Lee, J. H. & Ku, B.-C. Layer-by-layer assembled graphene oxide films and barrier properties of thermally reduced graphene oxide membranes. *Carbon Lett.* **14**, 247–250 (2013).
136. Yang, D. *et al.* Chemical analysis of graphene oxide films after heat and chemical treatments by X-ray photoelectron and Micro-Raman spectroscopy. *Carbon N. Y.* **47**, 145–152 (2009).
137. Lin-Vien, D., Colthup, N. B., Fateley, W. G. & Grasselli, J. G. CHAPTER 17 - Aromatic and Heteroaromatic Rings BT - The Handbook of Infrared and Raman Characteristic Frequencies of Organic Molecules. in 277–306 (Academic Press, 1991).
138. Lu, F., Jin, M. & Belkin, M. a. Tip-enhanced infrared nanospectroscopy via molecular expansion force detection. *Nat. Photonics* **8**, 307–312 (2014).
139. Dazzi, A. *et al.* AFM-IR: Combining atomic force microscopy and infrared spectroscopy for nanoscale chemical characterization. *Appl. Spectrosc.* **66**, 1365–1384 (2012).
140. Aydin, O. I., Hallam, T., Thomassin, J. L., Mouis, M. & Duesberg, G. S. Interface and strain effects on the fabrication of suspended CVD

graphene devices. *Solid. State. Electron.* **108**, 75–83 (2015).